

Experiments with remote entanglement using single barium ions

Nathan Kurz

A dissertation
submitted in partial fulfillment of the
requirements for the degree of

Doctor of Philosophy

University of Washington

2010

Program authorized to offer degree:
Physics

University of Washington
Graduate School

This is to certify that I have examined this copy of a doctoral dissertation
by

Nathan Kurz

and have found it complete and satisfactory in all respects,
and that any and all revisions required by the final
examining committee have been made.

Chair of the Supervisory Committee:

Boris B. Blinov

Reading Committee:

Boris B. Blinov

Larry Sorensen

David Cobden

Date: _____

In presenting this dissertation in partial fulfillment of the requirements for the doctoral degree at the University of Washington, I agree that the Library shall make its copies freely available for inspection. I further agree that extensive copying of the dissertation is allowable only for scholarly purposes, consistent with "fair use" as prescribed in the U.S. Copyright Law. Requests for copying or reproduction of this dissertation may be referred to ProQuest Information and Learning, 300 North Zeeb Road, Ann Arbor, MI 48106-1346, 1-800-521-0600, to whom the author has granted "the right to reproduce and sell (a) copies of the manuscript in microform and/or (b) printed copies of the manuscript made from microform."

Signature _____

Date _____

University of Washington

Abstract

Experiments with remote entanglement using single barium ions

Nathan Kurz

Chair of the Supervisory Committee:
Dr. Boris B. Blinov
Physics Department

Barium ions are trapped and Doppler cooled in a linear Paul trap with the goal of demonstrating state initialization, single-qubit operations and detection. Rabi rotations are demonstrated on the $6S_{1/2} \leftrightarrow 6P_{3/2}$ transition using single pulses from a mode-locked Ti:Sapphire laser, and some evidence for the same on the more useful $6S_{1/2} \leftrightarrow 6P_{1/2}$ transition is shown. With the goal of entangling the polarization mode of emitted photons with the spin state of the ion in the trap in mind, single photon generation and detection ability is demonstrated. A stabilized $1.762 \mu\text{m}$ laser is used on the $6S_{1/2} \rightarrow 5D_{5/2}$ transition to demonstrate the ability to state selectively shelve the ion from the ground state to be used as readout. Using the techniques that will enable qubit operations and readout, several quantities of interest in $^{137}\text{Ba}^+$ are measured either for the first time or to higher accuracy than previously achieved.

TABLE OF CONTENTS

	Page
List of Figures	ii
List of Tables	iii
Abbreviations	iv
Chapter I: Atomic Physics & Quantum Computation	1
1.1 Introduction	1
1.2 Atom-light interactions	6
1.3 Matrix elements & multipole expansion	11
Chapter II: Ion Traps & Lasers	19
2.1 Ion trapping	19
2.2 Doppler cooling - a semiclassical picture	23
2.3 Doppler cooling - a quantum perspective	25
2.4 Trapping and cooling Ba ⁺	27
Chapter III: Ultrafast interactions	41
3.1 Mode-locked lasers	42
3.2 Ultrafast pulses & ions	45
3.3 Single pulse selection	46
3.4 Rabi flop at 455 nm	48
3.5 Branching ratios from 6P _{3/2}	50
3.6 Ultrafast excitation at 493 nm	56
Chapter IV: Single Photon Source	61

4.1 Single photon interference on a beam splitter	62
4.2 Experimental verification of single photon generation	67
Chapter V: Initialization & Readout	71
5.1 Magnetic field effects, briefly	71
5.2 Optical pumping	76
5.3 Shelving to $5D_{5/2}$ at $1.762 \mu\text{m}$	79
5.4 Precise measurement of $g_{5D_{5/2}}$	82
Chapter VI: Toward a Zeeman qubit & outlook	91
6.1 Zeeman qubit: How & why?	92
6.2 From entangled ions and photons to entangled ions	95
6.3 Applications	98
Bibliography	103

LIST OF FIGURES

Figure Number	Page
1.1 Bloch sphere representation of a general qubit state.....	5
1.2 Rabi oscillations, on resonance and detuned.....	9
1.3 Lamba structure with Rabi frequencies, detunings and decay rates...	11
1.4 Multipole radiation patterns (a) dipole, (b) quadrupole.....	12
1.5 Relative intensities for transitions in an $I = 3/2$ ion.....	17
2.1 Secular motion and micromotion of an ion in a Paul trap.....	22
2.2 Not-to-scale drawing of a linear Paul trap.....	22
2.3 Micromotion/secular sidebands of a ion-trap system.....	27
2.4 Barium ion energy levels.....	28
2.5 Energy levels in neutral Ba used for photoionization.....	32
2.6 (a) Cooling laser SHG cavity layout (b) Bias-T for PDH error signal	33
2.7 ADuC7020 SHG cavity servo.....	34
2.8 Atmospheric pressure-induced drift in Angstrom wavelength meter ..	35
2.9 Collected ion fluorescence (a) telegraph signal (b) histogrammed	37
2.10 Block diagram of experiment.....	39
3.1 Mira Ti:Sapphire laser.....	44
3.2 Numerical solution to optical Bloch equations with sech^2	46
3.3 Pulse picker electronics.....	47
3.4 Rabi flop at 455 nm.....	49
3.5 Weak excitation experiment to establish absolute decay ratios.....	51
3.6 Comparison amongst previous matrix element measurements.....	54

3.7 Ion fluorescence at 493 nm from Ti:Sapphire pulses	57
3.8 Ion-photon entanglement schemes	59
4.1 50-50 Beamsplitter output states	63
4.2 $g^{(2)}$ correlation function form	66
4.3 (a) Single photon generating pulse sequence (b) involved energy levels	67
4.4 $g^{(2)}$ function with CW 650 nm pulses	69
5.1 Zeeman shifts associated with $6S_{1/2} \rightarrow 5D_{5/2}$ transition	74
5.2 Optical pumping in (a) $^{137}\text{Ba}^+$ and (b) $^{138}\text{Ba}^+$	77
5.3 Zeeman resonance with and without optical pumping	80
5.4 $6S_{1/2}; M_J = +1/2 \leftrightarrow 5D_{5/2}; M_J = +3/2$ Rabi oscillations	83
5.5 (a) Measured 1.762 μm transitions, (b) Single field spectrum	85
5.6 Extrapolated positions of carrier transitions	86
6.1 Preliminary results of RF Zeeman spectroscopy	95
6.2 Space-time diagrams for loophole-free Bell test	100

LIST OF TABLES

Table Number	Page
1.1 Candidate qubit ions	4
2.1 Isotope shifts and abundances of barium isotopes	29
3.1 Measured quantities in the $6P_{3/2}$ decay	53
3.2 Systematics in branching ratio measurement	55
5.1 Landé g_J factors for low-lying states of $^{138}\text{Ba}^+$	72

ABBREVIATIONS

ADC Analog to digital converter - a device which accepts a continuously variable voltage signal and outputs a discretely-valued sequence

AOM Acoustic optic modulator - an RF device in which an acoustic standing wave in a solid state medium diffracts incident light, changing its direction and shifting its frequency by integer multiples of the input RF

APD Avalanche photodiode - a photon-counting device in which successively higher voltages accelerate electrons created by photons incident on a photosensitive semiconductor

BBO β -Barium borate - a nonlinear optical crystal well-suited to create second harmonic light across a wide wavelength range

DAC Digital to analog converter - a device which outputs an analog voltage proportional to an input digital level

ECDL External cavity diode laser - a laser design in which a diode is narrowed in frequency by retro-reflecting a portion of its emitted light

(EM)CCD (Electron-multiplied) Charge-coupled device - an imaging device comprised of a 2D array of semiconductor pixels, which may incorporate a mechanism for gain

EOM Electro-optic modulator - a device containing a nonlinear crystal whose index of refraction can be altered by applied electric field, used to frequency modulate an incident laser beam with RF

FSR Free spectral range - a frequency which characterizes the spacing between longitudinal modes of an optical cavity, equal to the speed of light

divided by twice the cavity length

FWHM Full width half maximum - a width measurement of a peak at a height equal to half the maximum height on both sides of the peak

IR Infrared - refers to the portion of the electromagnetic spectrum greater than approximately 700 nm up to several tens of microns, often subdivided into near-, mid- and far-infrared

LED Light-emitting diode - an incoherent semiconductor light source which emits light at a frequency determined by the electronic bandgap

Op Amp Operational amplifier

PDH Pound-Drever-Hall - a laser stabilization technique in which the error signal is generated by frequency or phase modulation of the laser light

PMT Photo-multiplier tube - a photosensitive device which makes use of the photoelectric effect to convert an incident photon into a measurable current signal

RF Radio frequency - the portion of the electromagnetic spectrum with frequency ranging from 3 kHz to 3 THz, often subdivided

SHG Second harmonic generation - a nonlinear optical process which occurs in particular media, creating output light of twice the frequency as incident light

TDC Time to digital converter - a device which uses a start-stop latch and digital timer to record separations between identical signals

Ti:Sapphire Titanium-doped sapphire - a solid state crystal doped with Ti^{3+} ions which have broad lasing transitions from 600-1000 nm amongst

vibrational bands

TTL Transistor-transistor logic - a logic system with on and off nominally at 5 V and 0 V, respectively

UHV Ultra-high vacuum - refers to vacuum with pressure less than 10^{-9} Torr

UV Ultraviolet - the portion of the electromagnetic spectrum with wavelength less than 400 nm down to approximately 10 nm

VCO Voltage-controlled oscillator - an RF device which generates a signal whose frequency is determined by an applied DC voltage level

VVA Voltage-variable attenuator - an RF device which attenuates an input signal by an amount determined by an applied DC level

ACKNOWLEDGMENTS

I have to thank my parents for their encouragement and support throughout my entire life, especially over the last five years of graduate school. Without what they have done for me, I wouldn't be anywhere near where I am now. Never once have I heard, "Get a real job," for which I am thankful. I also have to thank my wife-to-be Valerie Wall for her support and putting up with me over the last few years.

Of course, I need to thank my thesis advisor, Dr. Boris Blinov, for both his technical guidance throughout my work on this project and for always knowing when it was time to make a stop at Big Time. Equally important individuals are my colleagues, Matt Dietrich and Shu Gang, without whom this work would have never come to completion. Drs. Norval Fortson and Jeff Sherman must be recognized for indispensable advice in the early days of the group. None of the apparatus would have gotten built without Ron Musgrave, Bryan Venema, Hans Bern and Jim Greenwell; I learned an immeasurable amount about making things from them. Others who contributed to this project, either with blood, sweat and tears or timely advice and deserve recognition are Gary Howell, Adam Kleczewski, Ryan Bowler, Viki Mirgon, Joanna Salacka, Peter Greene, Tom Chanders and Tom Loftus. I am also appreciative of my new colleagues Tom Noel, John Wright and Chen-Kuan Chou, who have accepted the flame being passed to them.

My reading committee of Drs. Larry Sorensen and David Cobden deserve a special thanks for actually reading this and providing critiques.

DEDICATION

For my old man - if we didn't spend years almost electrocuting ourselves and each other, I would have probably been starving as an artist right now.

1 ATOMIC PHYSICS & QUANTUM COMPUTATION

Anybody who is not shocked by quantum theory has not understood it.

-Niels Bohr

1.1 Introduction

Theoretical conjecture, bold new ideas and brilliant experimental design have played off one another in exciting ways in the last century of physics. Quantum mechanics was founded in an effort to explain experiments probing the nature of matter at increasingly smaller scales. On the flip side, theoretical predictions of Einstein and Bose led to the experimental creation of condensates out of ultracold gasses, albeit seventy years later. The desire to study matter at the individual particle scale was a natural goal, realized in 1980 by Hans Dehmelt at the University of Washington with single trapped barium ions [24, 77].

Since that time, single trapped ions have been extensively studied and have found many practical applications. The obvious reason for their utility is their simplicity. Since they are single particles most often confined in one of the simplest potentials imaginable, the harmonic oscillator, their motion is well understood and obviates the need for quantum statistics. Trapping times of days or weeks are easily achievable, allowing for steady accumulation of statistics. Inhomogeneous effects such as Doppler or pressure broadening can be made very

small, allowing extremely accurate measurements. Among the many applications of trapped ions are studies of the variation of fundamental constants [86, 40], the construction of more accurate frequency standards [66, 93], tests of violations of fundamental symmetries and physics beyond the Standard Model [35, 41] and applications in quantum computation and quantum information technology [13, 17, 71]. Indeed, foundational tests of quantum theory itself can be realized with trapped ions [99]

This indirectly brings us to the subject of silicon-based computing technology, which itself is approaching the atomic scale and cannot feasibly be made too terribly much smaller without running into problems with quantum phenomena. Rather than engineering a means of getting around the quantum nature of matter to prolong our dependence on established computing technology, the answer seems to be to use quantum mechanics to usher in a whole new generation of computers. This is not a new idea. According to Richard Feynman in a 1982 talk given at the First Conference on the Physics of Computation at MIT, “If computational systems are a natural consequence of physical law, then a quantum computer is not only possible, but inevitable. It may take decades, perhaps a century, but a commercially viable quantum computer is a certainty [38].” Beyond esoteric interest to probe the fundamental features of quantum information, a quantum computer has applications in factoring and searching algorithms and in the simulation of quantum systems which cannot be solved by classical computers.

In principle, any two-level quantum system satisfying a basic set of requirements can be a quantum computer. IBM’s David DiVincenzo stated in 1995 [28] that to perform as a quantum computer, a system must fulfill the following basic set of criteria,

- 1) A scalable physical system with well-characterized qubit
- 2) The ability to initialize qubits to a fiducial state
- 3) Decoherence time much longer than gate operation time

- 4) A “universal set” of quantum gates
- 5) Qubit-specific measurement capability
- 6) Interconversion between stationary and “flying” qubits
- 7) Ability to faithfully transmit flying qubits

To varying degrees, several physical systems possess these attributes. Among the candidate systems currently under investigation are nuclear magnetic resonance in molecules, correlated pairs of photons, arrays of trapped neutral atoms, individual trapped ions, coupled superconducting junctions, quantum dots, nitrogen vacancy centers in diamond and other solid state systems.

Trapped ions are the subject of this work and are at the forefront of research in practical quantum computation. Each ion of a particular species is perfectly characterized; its energy levels provide rich structure to exploit for qubit states. These can be linked and manipulated by their coupling to photons or phonons and can be very long-lived (order of seconds) in comparison to the time required for individual excitations using radio-frequency (RF) or optical photons(sub-millisecond). Qubit state readout can also be easily performed by engineered pulse sequences. The ability to transmit quantum information over long distances is naturally accomplished via emitted photons, which can be sent over optical fibers. A summary of the relevant properties of the different ionic species currently being investigated appears in Table 1.1.

Classical computers process information via bits which take the values 0 and 1. Quantum computation makes use of a two-level quantum system with the states $|0\rangle$ and $|1\rangle$, which in the specific case of trapped ions correspond to two distinct spin states. The advantage over classical computers is the property that a quantum mechanical system can in general exist in a superposition of the two qubit states, written $|\psi\rangle = \cos\left(\frac{\theta}{2}\right)|0\rangle + e^{i\phi}\sin\left(\frac{\theta}{2}\right)|1\rangle$, where the

Table 1.1: Ionic species currently under investigation as qubit candidates. In some cases, several isotopes are significant. All are single valence electron ions, so the cooling wavelength listed is the splitting between the ground $nS_{1/2}$ and either the $nP_{1/2}$ or $nP_{3/2}$ excited state. The hyperfine splitting refers only to the ground state of the odd isotope listed with its corresponding nuclear spin.

Isotope	Nuclear spin	Cooling wavelength (nm)	Hyperfine splitting (GHz)
$^{137/138}\text{Ba}^+$	3/2, 0	493	8.037
$^9\text{Be}^+$	3/2	313	1.25
$^{40/43}\text{Ca}^+$	0, 7/2	397	3.226
$^{110/111}\text{Cd}^+$	0, 1/2	214.5	14.5
$^{199}\text{Hg}^+$	1/2	194	40.5
$^{24/25}\text{Mg}^+$	0, 5/2	280	1.8
$^{87/88}\text{Sr}^+$	9/2, 0	422	5
$^{171/173}\text{Yb}^+$	1/2, 5/2	369.5	12.643, 10.49
$^{64,67}\text{Zn}^+$	5/2	202.6	7.2

variables θ and ϕ correspond to the polar and azimuthal angles in an abstract space most easily visualized on the Bloch sphere (Figure 1.1). Operations on this qubit are represented as 2×2 matrices and take the form of rotations on the Bloch sphere. Physically, rotations in the θ direction, often denoted σ_x represent population transfer between the $|0\rangle$ and $|1\rangle$ states while rotations in ϕ , or σ_z rotations, represent relative phase. The full mathematic description of the Bloch sphere will be given in the subsequent section.

Extending this description to multiple qubits is straightforward. With n qubits, the general state $|\psi\rangle$ becomes a 2^n -component vector with complex amplitudes α_k , where k is an index running from 0 to 2^n . Two qubits then can be represented as $|\psi\rangle = \alpha_0 |00\rangle + \alpha_1 |01\rangle + \alpha_2 |10\rangle + \alpha_3 |11\rangle$. A consequence of this property is the existence of states that cannot be factored into the product of single-qubit states. Such states are known as entangled and have been the subject of considerable theoretical and experimental consideration. In the world of quantum computation, entangled states naturally arise in multi-qubit operations, a necessary ingredient for all quantum algorithms.

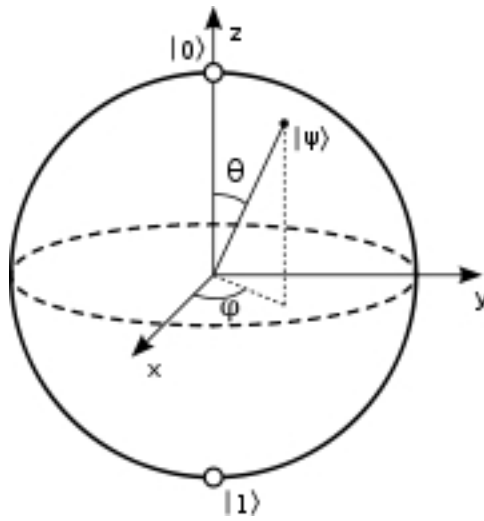


Figure 1.1: Bloch sphere representation of a general qubit state $|\psi\rangle$. Eigenstates $|0\rangle$ and $|1\rangle$ are located at the poles of the sphere.

Take for instance one of the maximally entangled Bell states $\frac{1}{\sqrt{2}}(|01\rangle + |10\rangle)$. This belongs to a family of states which have been the subject of immense study since its ramifications were first questioned by Einstein, Podolsky and Rosen in 1935 [37]. They argued that given the measurement of the quantum state of one particle, the fact that the other particle's state was determined with certainty irrespective of physical separation implied the existence of “hidden variables” not contained in quantum theory. Bell [8] and others [18, 19] recast the original conjectures into experimentally testable terms in the form of inequalities measuring the correlation between particles in entangled states. The result of the forty subsequent years of experimental testing with photons [42, 4, 81], subatomic particles [47], trapped ions [89] and coherent solid-state systems [2] have supported the predictions of quantum theory time and time again.

1.2 Atom-light interactions

At the heart of atomic physics is a singular concept, the interaction of an atom with electromagnetic radiation. This interaction is described by a fairly simple Hamiltonian

$$\hat{H}_{int} = -e\vec{E}(\vec{r}, t) \cdot \vec{r} \quad (1.1)$$

The time-oscillating electric field is given by $\vec{E}(\vec{r}, t) = \vec{E} \cos(\omega t + \vec{k} \cdot \vec{r})$, where \vec{k} is the so-called wavevector related to the wavelength of the radiation by $|\vec{k}| = 2\pi/\lambda$. This electric field can be written as the sum of two complex exponentials, making the interaction Hamiltonian then equal to

$$\hat{H}_{int} = -\frac{e\vec{E}}{2} \left(e^{i(\omega t + \vec{k} \cdot \vec{r})} + e^{-i(\omega t + \vec{k} \cdot \vec{r})} \right) \cdot \vec{r} \quad (1.2)$$

The problem can be made much simpler with two approximations. First of all, a unitary transformation into a reference frame rotating at ω , $\hat{H}_{int} \rightarrow \hat{H}'_{int} = \hat{H}_{int} e^{-i\omega t}$, makes the effect of the second term in the exponential negligible in the case of nearly resonant radiation because of its fast oscillation. This is known as the *rotating wave approximation*. Secondly, note that the extent of the atomic dipole is of order the Bohr radius a_o which is much less than the wavelength of the incident radiation, so in an expansion of the complex exponential $e^{i(\omega t + \vec{k} \cdot \vec{r})} = e^{i\omega t} \left(1 + i(\vec{k} \cdot \vec{r}) + \dots \right)$, the term $(\vec{k} \cdot \vec{r})$ is very small and can be neglected for the time being.

If it is assumed for the sake of simplicity that only two atomic levels are involved, so the solution ansatz $|\psi\rangle = c_1 |1\rangle e^{-i\omega_1 t} + c_2 |2\rangle e^{-i\omega_2 t}$, where $\omega_{1,2} = \epsilon_{1,2}/\hbar$ and $\epsilon_{1,2}$ the energies of the two states, can be plugged into the time-dependent Schrödinger equation along with the interaction Hamiltonian. Defining the atomic splitting $\omega_0 = \omega_1 - \omega_2$, one finds for the complex amplitudes c_1 and c_2

$$\begin{aligned}
i\dot{c}_1 &= c_2 e^{i(\omega-\omega_o)t} \frac{\Omega}{2} = c_2 e^{i\delta t} \frac{\Omega}{2} \\
i\dot{c}_2 &= c_1 e^{-i(\omega-\omega_o)t} \frac{\Omega^*}{2} = c_1 e^{-i\delta t} \frac{\Omega^*}{2}
\end{aligned} \tag{1.3}$$

where the detuning of the incident radiation from the atomic resonance is $\delta = \omega - \omega_o$ and the Rabi frequency $\Omega \equiv \frac{e}{\hbar} \langle 1 | \vec{r} \cdot \vec{E} | 2 \rangle$ have been introduced. For reasons that will become apparent when generalizing this problem to include more than two atomic states as is the case in real ions, the density matrix formalism is a particularly useful for solving this problem. It will also provide the formalism to visualize the problem and its solutions in a particularly convenient way.

$$|\psi\rangle \langle\psi| = \begin{pmatrix} c_1 \\ c_2 \end{pmatrix} \begin{pmatrix} c_1^* & c_2^* \end{pmatrix} = \begin{pmatrix} |c_1|^2 & c_1 c_2^* \\ c_1^* c_2 & |c_2|^2 \end{pmatrix} \equiv \begin{pmatrix} \rho_{11} & \rho_{12} \\ \rho_{21} & \rho_{22} \end{pmatrix} \tag{1.4}$$

The diagonal elements of this matrix are called the populations of the two states in the problem, while the off-diagonal elements are known as coherences. Making a change of variables $c_1 \rightarrow c'_1 = c_1 e^{-i\frac{\delta}{2}t}$ and $c_2 \rightarrow c'_2 = c_2 e^{+i\frac{\delta}{2}t}$ and defining the in-phase $u \equiv \Re(\rho_{12})$ and quadrature $v \equiv \Im(\rho_{12})$ components of the dipole in the rotating frame, the optical Bloch equations in the absence of damping are derived

$$\begin{aligned}
\dot{u} &= \delta v \\
\dot{v} &= -\delta u + \Omega w \\
\dot{w} &= -\Omega v
\end{aligned} \tag{1.5}$$

in which w is the population difference, or inversion, $\rho_{11} - \rho_{22}$ between the two states, and

the variables u and v are the dispersive and absorptive components of the dipole moment effective in coupling to the field to produce energy changes in the atom's energy expectation value $\frac{1}{2}\hbar\omega_o w$ [1]. Rather than jumping directly to the solution of this coupled set of differential equations, it is worthwhile to give some justification to Fig 1.1 which is a graphical representation of these three variables. Defining the vectors $\vec{R} = u\hat{e}_1 + v\hat{e}_2 + w\hat{e}_3$ and $\vec{W} = \Omega\hat{e}_1 + \delta\hat{e}_3$, the three optical Bloch equations can be summarized with a single expression as

$$\frac{d\vec{R}}{dt} = \vec{R} \times \vec{W} \quad (1.6)$$

\vec{R} is the state vector on the unit sphere, and \vec{W} is the effective “torque” on \vec{R} by the field. It is now worthwhile to give the solution to the problem in terms of the real measurable quantity w . Solving analytically, the population of the upper state 2 is $\rho_{22} = \frac{1-w}{2} = \left(\frac{\Omega}{W}\right)^2 \sin^2\left(\frac{Wt}{2}\right)$. Note that the magnitude of \vec{W} is equal to $\sqrt{\Omega^2 + \delta^2}$. This is often referred to as the generalized Rabi frequency and is the frequency of radiation-driven oscillations between the two states in the presence of a detuning δ which reduces simply to Ω for resonant excitation. From this graphical description, we can see what happens when resonant radiation is incident on the atom for a time t_o such that $\Omega t_o = \pi$. The population ρ_{22} will go from 0 to 1 or vice versa, that is, all population will be transferred from one state to the other. This is known as a π -pulse and the term will be used repeatedly throughout this work. Several Bloch sphere transformations and time evolutions of states are shown in Fig. 1.2.

Up until now, the assumption has been made that both states are infinitely long-lived. This is never the case in atomic physics. Coupling to electromagnetic vacuum modes ensures that every excited state will decay to the ground state with a lifetime τ . The rate at which the decay occurs for an atomic dipole is given by

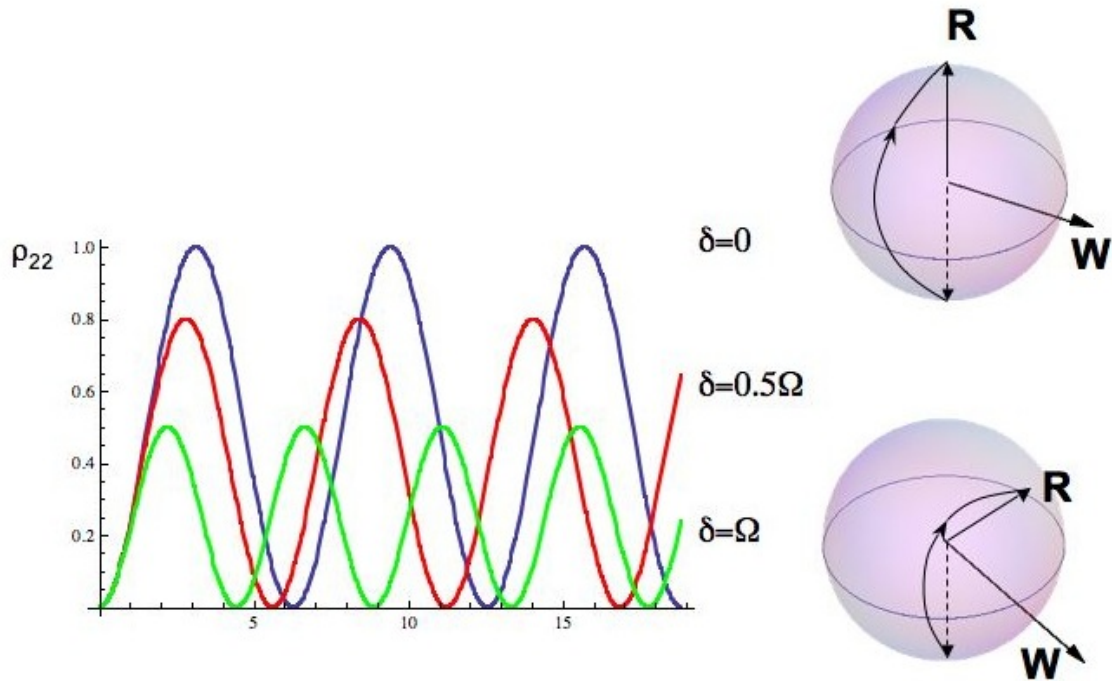


Figure 1.2: Left is the time evolution of an atom under the influence of incident radiation on resonance and with two different values for the detuning. Note that the frequency of oscillation in excited state population increases with greater detuning and the maximum population of that state decreases. On the right are two Bloch sphere representations of the evolution of a state vector \vec{R} under the influence of a driving field given by the pseudo-torque vector \vec{W} .

$$\gamma = \tau^{-1} = \frac{\omega_o^3}{3\pi\epsilon_o\hbar c^3} |\langle 2|er|1\rangle|^2 \quad (1.7)$$

Exactly as in the damping of a classical dipole, this decay rate is incorporated into the optical Bloch equations as a damping term, contributing to decay from the upper into the lower state, as well as a loss of coherence. The optical Bloch equations become

$$\dot{u} = \delta v - \frac{\gamma}{2}u \quad (1.8)$$

$$\begin{aligned}\dot{v} &= -\delta u + \Omega w - \frac{\gamma}{2}v \\ \dot{w} &= -\Omega v - \gamma(w - 1)\end{aligned}$$

A two-level system, while it would make the perfect qubit, is unphysical. As stated before, the density matrix formalism is the most convenient way to generalize the interaction problem to n states as

$$\rho = \begin{pmatrix} |c_1|^2 & c_1 c_2^* & \cdots & c_1 c_n^* \\ c_1^* c_2 & |c_2|^2 & & \\ \vdots & & \ddots & \\ c_n c_1^* & & & |c_n|^2 \end{pmatrix} \quad (1.9)$$

In particular, for a so-called three level Lambda system shown in Fig 1.3, these equations when damping terms are inserted become

$$\begin{aligned}\dot{\rho}_{11} &= i\frac{\Omega_{13}}{2}(\rho_{13} - \rho_{31}) + \gamma_1\rho_{33} \\ \dot{\rho}_{22} &= i\frac{\Omega_{23}}{2}(\rho_{23} - \rho_{32}) + \gamma_2\rho_{33} \\ \dot{\rho}_{33} &= i\frac{\Omega_{13}}{2}(\rho_{31} - \rho_{13}) + i\frac{\Omega_{23}}{2}(\rho_{32} - \rho_{23}) - (\gamma_1 + \gamma_2)\rho_{33} \\ \dot{\rho}_{12} &= i\left[(\delta_2 - \delta_1)\rho_{12} + \frac{\Omega_{23}}{2}\rho_{13} - \frac{\Omega_{13}}{2}\rho_{32}\right] \\ \dot{\rho}_{13} &= i\left[\frac{\Omega_{13}}{2}(\rho_{11} - \rho_{33}) + \frac{\Omega_{23}}{2}\rho_{12} - \delta_1\rho_{13}\right] - \frac{\gamma_1}{2}\rho_{13} \\ \dot{\rho}_{23} &= i\left[\frac{\Omega_{23}}{2}(\rho_{22} - \rho_{33}) + \frac{\Omega_{13}}{2}\rho_{21} - \delta_2\rho_{23}\right] - \frac{\gamma_2}{2}\rho_{23}\end{aligned} \quad (1.10)$$

This system of equations can (and will be) used to analyze our particular ionic qubit, Ba^+ , whose complete level diagram will be presented in Chapter 2.

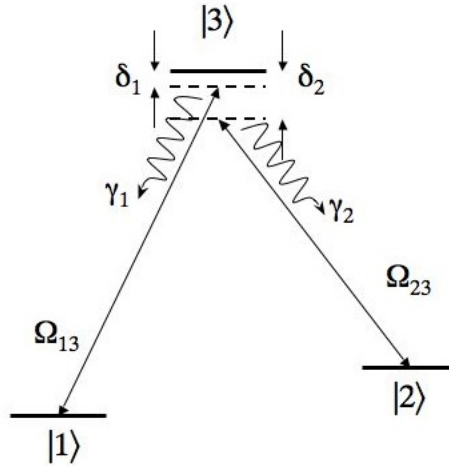


Figure 1.3: Energy level diagram of an atomic system with three energy levels with $E_3 > E_2 > E_1$, or a lambda system. Driven oscillations between $|1\rangle$ and $|3\rangle$ occur at a Rabi frequency of Ω_{13} at a detuning of δ_1 . In addition, the decay rate from $|3\rangle$ to $|1\rangle$ occurs at a rate γ_1 . Likewise, states $|2\rangle$ and $|3\rangle$ are linked by a field producing a Rabi frequency Ω_{23} at detuning δ_2 subject to decay γ_2 .

1.3 Matrix elements and Multipole expansions

A quantity appearing in both the Rabi frequency and decay rate is something which has been written but as of yet not named or otherwise discussed. This is the dipole matrix element $e\langle 1|\vec{r}\cdot\vec{\epsilon}|2\rangle$, where the electric field strength E_o has been separated from its polarization $\vec{\epsilon}$. Likewise, labeling the states simply by numbers sweeps under the rug the fact that we are actually talking about atomic states, designated by principle and angular momentum quantum numbers. There is a great deal of complicated calculation involved in actually determining the value of the matrix element for a given transition and a considerable amount that can be learned from measuring it for an actual atom.

To actually calculate atomic matrix elements, first it is convenient to expand the polarization vector into a basis defined by the spherical unit vectors

$$\begin{aligned}\hat{\epsilon}_0^{(1)} &= -\sin\theta\hat{\theta} \\ \hat{\epsilon}_{\pm 1}^{(1)} &= \frac{e^{\pm i\phi}}{\sqrt{2}}\left(\cos\theta\hat{\theta} \mp i\hat{\phi}\right)\end{aligned}\tag{1.11}$$

which correspond to linearly and circularly polarized light, respectively. These vectors also determine the radiation pattern of emitted photons. Plots of $\langle I \rangle = \left| \hat{\epsilon}_q^{(1)} \right|^2$ can be found in Fig. 1.4 (a). When the polarization vector is expanded in this basis, all of the usual separations of

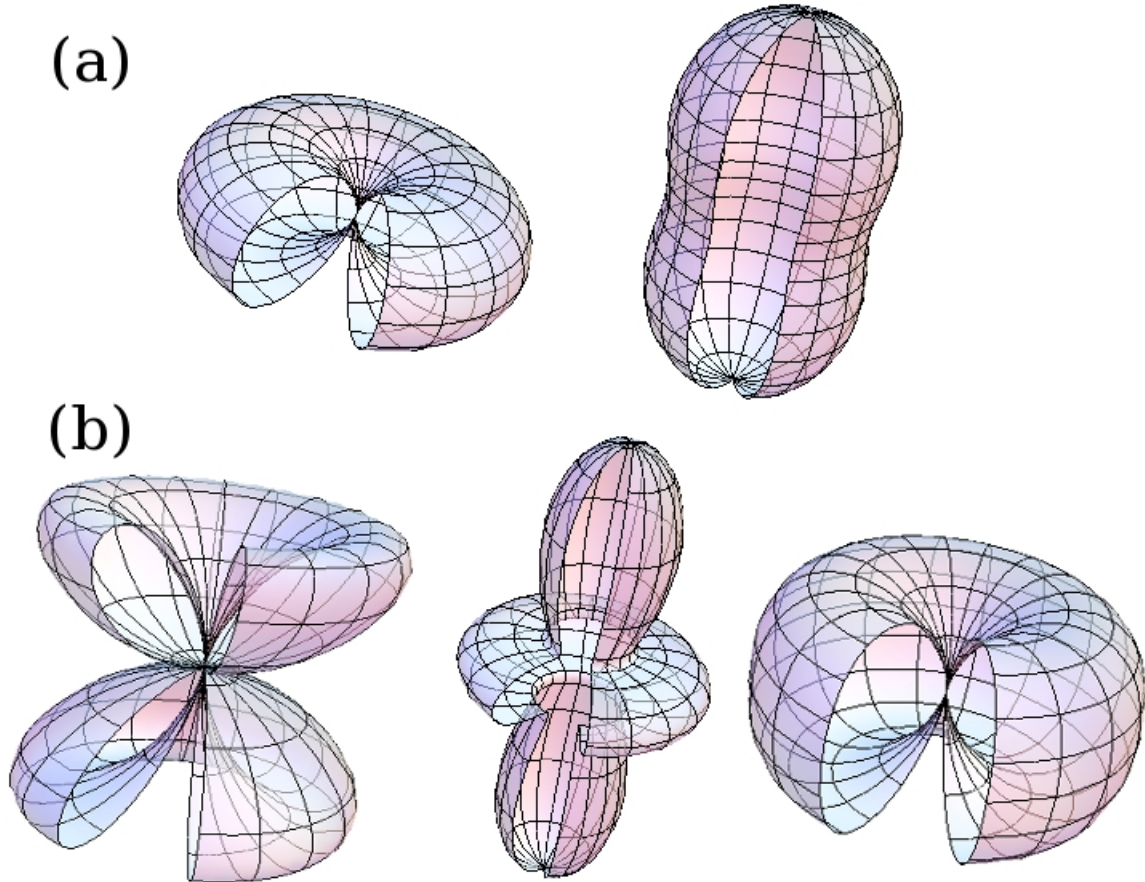


Figure 1.4: Radiation patterns for multipole transitions up to order two. In (a), left to right are $\Delta M_J = 0$ and $\Delta M_J = \pm 1$. In (b), left to right are $\Delta M_J = 0$, $\Delta M_J = \pm 1$ and $\Delta M_J = \pm 2$.

variables apply, and the angular part and radial parts of the matrix element can be computed separately. Spin-orbit coupling makes L and S unsuitable quantum numbers so the vector sum $J = L + S$ is used, and the matrix element becomes

$$\mu = e \langle n' J' M'_J | \hat{\epsilon} \cdot \vec{r} | n J M_J \rangle \quad (1.12)$$

Since the radial portion only involves the L portion of the J summation, the eigenstates of the total angular momentum have to be rewritten using the Wigner-Eckhart theorem

$$|n J M_J\rangle = \sum_{M_S, M_L} (-1)^{-L+S-M_J} \sqrt{2J+1} \begin{pmatrix} L & S & J \\ M_L & M_S & -M_J \end{pmatrix} |n L M_L\rangle |S M_S\rangle \quad (1.13)$$

so that after insertion into the matrix element, performing the double summation which produces the delta functions $\delta_{SS'}$ and $\delta_{M_S M_{S'}}$, and using Clebsch Gordon coefficient identities to compactify the expression, we get for the matrix element

$$\begin{aligned} \mu &= e (-1)^{L'+S-M'_J} \sqrt{(2J+1)(2J'+1)} \\ &\times \begin{Bmatrix} L' & J' & S \\ J & L & 1 \end{Bmatrix} \begin{pmatrix} J & 1 & J' \\ M_J & q & -M'_J \end{pmatrix} \langle n' L' \| r \| n L \rangle \end{aligned} \quad (1.14)$$

Another notation has been introduced in the above expression, the double-bar matrix element $\langle n' L' \| r \| n L \rangle$. This is an integral involving only the overlap of the two radial atomic wavefunctions. It is an overall factor that determines the strength of the coupling (and hence the Rabi frequency) between the two states and is common to all of the angular momentum transitions between two levels. From the $3j$ and $6j$ symbols in this expression, the dipole selection rules $L' = L \pm 1$ and $M'_J = M_J + q$ arise.

In the case that the nucleus has spin, as in $^{137}\text{Ba}^+$ with $I = 3/2$, the expression is slightly more complicated because of the hyperfine structure. In this case, $F = I + J$ which must first be expanded using Clebsch Gordon coefficients and then the J basis must be expanded in L and S . The result for the dipole matrix element is

$$\begin{aligned} \mu &= e(-1)^{1+L'+S+J+J'+I-M'_F} \langle n' L' \| r \| n L \rangle \\ &\times \sqrt{(2J+1)(2J'+1)(2F+1)(2F'+1)} \\ &\times \begin{Bmatrix} L' & J' & S \\ J & L & 1 \end{Bmatrix} \begin{Bmatrix} J' & F' & I \\ F & J & 1 \end{Bmatrix} \begin{pmatrix} F & 1 & F' \\ M_F & q & -M'_F \end{pmatrix} \end{aligned} \quad (1.15)$$

The same reduced matrix element appears here as well. The same selection rules as before apply, along with some important additions from the final $3j$ symbol. Specifically, for transitions involving $q = 0$ or linearly polarized light, F cannot equal F' . The results for an $I = 3/2$ nucleus ($^{137}\text{Ba}^+$) are shown in Fig. 1.5 [70].

A second approximation that was made that must be revisited is the fact that the expression for the spatial variation of the electric field was truncated at first order. If one looks at the next terms in the expansion $e^{i(\omega t + \vec{k} \cdot \vec{r})} = e^{i\omega t} \left(1 + i(\vec{k} \cdot \vec{r}) + \dots \right)$, one finds matrix elements involving the gradient of the electric field

$$\mu^{(2)} = \frac{e}{6} \langle n' J' M'_J | (\hat{\epsilon} \cdot \vec{r}) (\vec{k} \cdot \vec{r}) | n J M_J \rangle \quad (1.16)$$

Transitions involving such matrix elements are known as quadrupole transitions and are suppressed by an additional factor of the Bohr radius a_0 and two powers of $1/\lambda$ from the gradient. The expansion of the polarization vector involves now five basis vectors [95]

$$\begin{aligned}
\hat{\epsilon}_0^{(2)} &= \sqrt{5} \sin \theta \cos \theta \hat{\theta} \\
\hat{\epsilon}_{\pm 1}^{(2)} &= \sqrt{\frac{5}{6}} e^{\pm i\phi} \left(\cos 2\theta \hat{\theta} \mp i \cos \theta \hat{\phi} \right) \\
\hat{\epsilon}_{\pm 2}^{(2)} &= \pm i \sqrt{\frac{5}{6}} \sin \theta e^{\pm 2i\phi} \left(\pm i \cos \theta \hat{\theta} + \hat{\phi} \right)
\end{aligned} \tag{1.17}$$

Quadrupole radiation patterns $|\hat{\epsilon}_q^{(2)}|^2$ can be found alongside those for the dipole case in Fig. 1.4 (b).

The procedure proceeds exactly the same as in the dipole case, with the expansion of angular momentum bases down to L and S using Clebsch Gordon coefficients and after all is said and done, the expression for the quadrupole matrix element looks shockingly similar to the dipole with a few important distinctions

$$\begin{aligned}
\mu &= \frac{e}{6} (-1)^{L'+S-M'_J} \sqrt{(2J+1)(2J'+1)} \\
&\times \begin{Bmatrix} L' & J' & S \\ J & L & 2 \end{Bmatrix} \begin{pmatrix} J & 2 & J' \\ M_J & q & -M'_J \end{pmatrix} \langle n' L' \| r^2 \| n L \rangle
\end{aligned} \tag{1.18}$$

Or for the case in which there is hyperfine structure

$$\begin{aligned}
\mu &= \frac{e}{6} (-1)^{2+L'+S+J+J'+I-M'_F} \langle n' L' \| r^2 \| n L \rangle \\
&\times \sqrt{(2J+1)(2J'+1)(2F+1)(2F'+1)} \\
&\times \begin{Bmatrix} L' & J' & S \\ J & L & 2 \end{Bmatrix} \begin{Bmatrix} J' & F' & I \\ F & J & 2 \end{Bmatrix} \begin{pmatrix} F & 2 & F' \\ M_F & q & -M'_F \end{pmatrix}
\end{aligned} \tag{1.19}$$

Now in principle, there can be transitions of $L' = L \pm 1$ or ± 2 and $M'_J = M_J + q$ or $M_J + 2q$. In principle, the process of taking increasing orders in the multipole expansion can continue and be extended to transitions coupling to the magnetic rather than electric field, but it is wise to stop here, although there is some effort in our group to observe an electric octupole transition coupling the $6P_{1/2}$ and $5D_{5/2}$ states in Ba^+ .

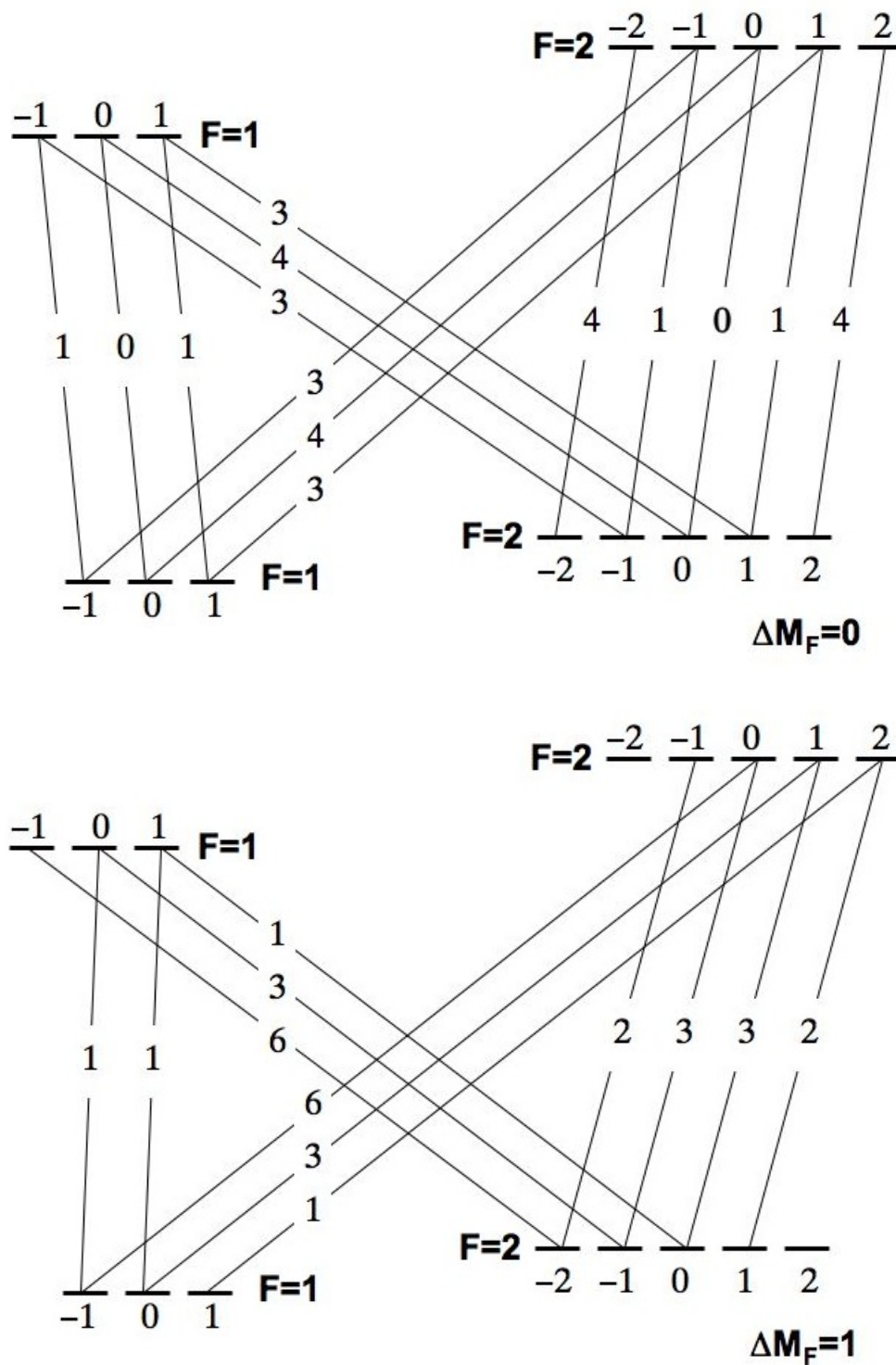


Figure 1.5: Relative transition strengths for dipole transitions in an atomic system with nuclear spin $I = 3/2$. Top are transitions which do not change M_F (π polarized excitation or emission), below are those which change M_F by 1 (σ^+ excitation or emission). Transitions which change M_F by -1 have the same relative strengths as those transitions in the lower diagram. [70]

2 ION TRAPS & LASERS

Quantum phenomena do not occur in a Hilbert space, they occur in a laboratory.

-Asher Peres

If it ain't broke, take it apart and fix it.

-Stephen Pollard

2.1 Ion trapping

Earnshaw's theorem - In order that the Laplace Equation for the electric field $\nabla^2\Phi = 0$ be satisfied, it is impossible to have an electrostatic minimum in three spatial directions, thus making a stable potential well in which to confine a charged particle likewise physically impossible.

That's unfortunate.

Luckily there are a few solutions to this problem. A potential that does satisfy the Laplace Equation is a hyperbolic paraboloid $\Phi(\vec{r}) = r^2 - 2z^2$. In one such trap, a strong magnetic field in the \hat{z} direction serves to confine ion orbits [83]. This so-called Penning trap is still a favorite for those performing high precision measurements of highly charged or very light ions. The more typical weapon of choice in the trapped ion quantum computation community is the Paul trap which effectively rotates the trapping potential at radio frequency. This will generate a pseudo-potential force whose time-averaged effect is to trap a charged particle [82]. Mathematically the Paul trap potential looks like

$$\Phi(\vec{r}) = (\Phi_o + V_{RF} \cos(\Omega_{RF}t)) \left(\frac{r^2 - 2z^2}{2r_o^2} \right) \quad (2.1)$$

where Φ_o is any DC component and V_{RF} and Ω_{RF} are the amplitude and frequency of the RF field applied to electrodes with a radius of r_o . Inserting this into Newton's second law gives a coupled set of differential equations for the radial and axial motion of the ion.

$$\begin{aligned} \frac{d^2r}{dt^2} + \left(\frac{eZ}{mr_o^2} \right) (\Phi_o - V_{RF} \cos(\Omega_{RF}t)) r &= 0 \\ \frac{d^2z}{dt^2} + \left(\frac{2eZ}{mr_o^2} \right) (\Phi_o - V_{RF} \cos(\Omega_{RF}t)) z &= 0 \end{aligned} \quad (2.2)$$

where eZ is the charge of the ion being trapped. The usual solution method is to recast the potentials and time variable in dimensionless terms

$$\begin{aligned} a_r &= -\frac{a_z}{2} \equiv \frac{4eZ\Phi_o}{mr_o^2\Omega_{RF}^2} \\ q_r &= -\frac{q_z}{2} \equiv \frac{2eZV_{RF}}{mr_o^2\Omega_{RF}^2} \\ \zeta &= \frac{\Omega_{RF}t}{2} \end{aligned} \quad (2.3)$$

yielding the well-studied Mathieu equation

$$\frac{d^2r}{d\zeta^2} + (a_r - 2q_r \cos 2\zeta) r = 0 \quad (2.4)$$

with an identical expression for the z (axial) coordinate. This differential equation has been well-studied and has both stable and chaotic orbits depending on the values of the parameters a_r and q_r in the equation. In particular $q_r \leq 0.9$ and $a_r \approx 0$ form the first region of stability

where most ion traps operate. Stable solutions relevant to the motion of ions in a Paul trap exhibit oscillatory behavior with the following form

$$r(t) = r_o \cos(\Omega_{trap}t) \left(1 - \frac{q_r}{2} \cos(\Omega_{RF}t)\right) \quad (2.5)$$

where $\Omega_{trap} = \frac{eZV_{RF}}{\sqrt{2}mr_o^2\Omega_{RF}}$ [39]. A solution of the same form exists for the axial coordinate. The first factor is known as the secular motion of the ion and typically occurs at a frequency significantly less than the RF drive frequency. This is simply the motion of the ion in a very nearly harmonic potential. In principle, there is a separate secular motion frequency for each degree of spatial freedom in the trap, but in most ion trap designs the asymmetry in the two radial directions is small enough that these are nearly degenerate. There are a number of ways to measure these frequencies in a trap, either by driving a trap electrode with a frequency near Ω_{trap} through a bias-T and observing ion heating, measuring the distance between two ions in the same trap and calculating the frequency Ω_{trap} assuming the Coulomb repulsion separates the ions in a harmonic well or by spectroscopically resolving the sidebands the motion imposes on either side of a narrow resonance. The second term is known as “micromotion” and is a small amplitude oscillation superimposed on the secular motion at Ω_{RF} . Fig. 2.1 shows a plot of the time evolution of the radial coordinate of an ion with both the secular motion and micromotion. Figure 2.3 shows the effect of those two oscillations on a narrow atomic resonance. Although micromotion is an unavoidable consequence of the oscillatory potential, excess micromotion in a Paul trap is undesirable and generally DC bias electrodes are included in trap designs to place the ion as near to the pseudo-potential minimum as possible [10].

All of this analysis was performed assuming rotationally symmetric hyperbolic electrodes, as was the case in Paul traps of old. Since that time, ion traps have undergone immense simplification, both to decrease the machining necessary to create the electrodes and to

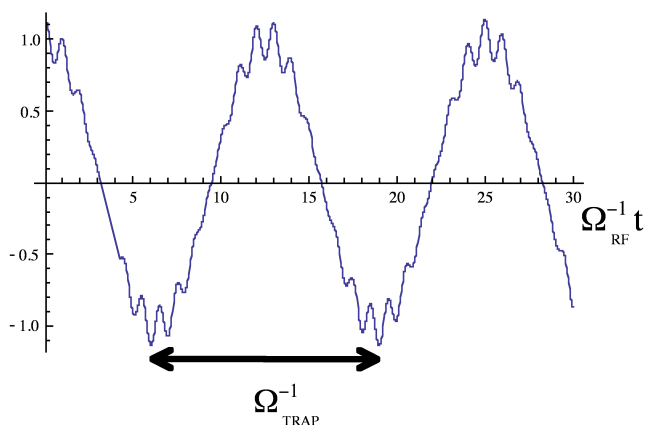


Figure 2.1: Numerical integration of the Mathieu equation to show the time evolution of the radial coordinate of an ion confined in a Paul trap. The horizontal units are integral periods of the RF drive frequency. Note that the fast oscillation superimposed on the slow secular motion occurs at Ω_{RF} .

to “open up” the design in order for increased optical access. Since the basic quantum gate protocol by Cirac and Zoller [17] calls for strings of ions coupled by their mutual Coulomb interaction, the linear Paul trap was developed [10]. To date, this has been the most significant trap geometry in terms of multiparticle entanglement generation and gate operations[13, 63]. Although investigation of new traps more suitable for microfabrication and scaling up to large numbers of ions is an important theme in trapped ion quantum

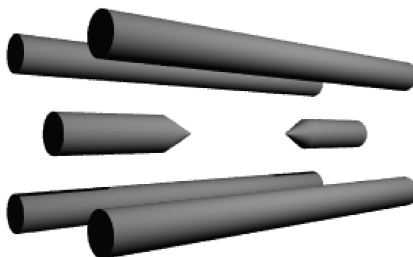


Figure 2.2: Cartoon drawing of a linear Paul trap like the one used to perform the work presented here. RF potential is applied to two rods diagonal to each other and the other two rods are held at ground. A few hundred DC volts applied to the needles provides axial confinement. The tips of the needles are about 2.5 mm apart and the spacing between rods about 0.5 mm.

computation [97, 102], all of the work presented here was performed on a four-rod linear trap shown in Fig. 2.2.

2.2 Doppler cooling - a semiclassical picture

Once a trap geometry has been realized, it is necessary to cool the motion of the ion in the trap. Because of the three-dimensional confinement of the RF pseudo-potential in an ion trap, it is sufficient to cool the ion along only one spatial axis as long as the incident laser's k -vector has components along all principle trap axes. This is an immense simplification over neutral atoms which require three pairs of beams. The ion moving within the trap will see incident light with frequency detuned from an atomic resonance by δ with an additional detuning due the first order Doppler shift

$$\delta_{ion} = \delta - \vec{k} \cdot \vec{v}_{ion} \quad (2.6)$$

Because of the Doppler shift in frequency for a red-detuned laser ($\delta < 0$), when the ion is moving toward the incident laser light it will be shifted closer to the atomic resonance and the probability for excitation will increase. When the ion is moving away, it will be less likely to be excited. Each photon absorption will reduce the momentum of the ion by an amount equal to $\hbar k$. For every excitation, there will be one photon emitted by the ion, which will be emitted isotropically in all directions. The net effect of this is to slow the motion of the ion. The average force over the entire process is

$$\langle F \rangle = \left\langle \frac{dP}{dt} \right\rangle = (\hbar k) R_{scatter} = \hbar k \gamma \rho_{22} \quad (2.7)$$

where ρ_{22} is the steady-state population of the excited state and takes the form

$$\rho_{22} = \frac{\sigma/2}{1 + \sigma + (2\delta_{ion}/\gamma)^2} \quad (2.8)$$

where $\sigma = 2\Omega^2/\gamma^2$ is the saturation parameter which is a measure of the effective broadening of transitions due to the decrease in excited state lifetime created by the coupling [39]. The denominator in the expression above can be expanded for small ion velocity and detuning to the red side of the atomic resonance. The result is [62]

$$\langle F \rangle \approx F_o (1 + \kappa v) \quad (2.9)$$

where F_o is the average force

$$F_o = \hbar k \gamma \frac{\sigma/2}{1 + \sigma + (2\delta/\gamma)^2} \quad (2.10)$$

and κ is the damping coefficient

$$\kappa = \frac{8k\delta/\gamma^2}{1 + \sigma + (2\delta/\gamma)^2} \quad (2.11)$$

This is a dissipative process and no such process can ever bring the ion to a motionless state. The results of the semi-classical theory of Doppler cooling show that the minimum temperature $k_B T_{min} = \langle E_{kin} \rangle$ is achieved when the cooling rate of the laser $\dot{E}_{kin} = \langle F \rangle v$ is balanced by the heating due to random thermal fluctuations of the ion in the laser field similar to Brownian motion, $\dot{E}_{kin} \approx 2\gamma \frac{\hbar^2 k^2}{m}$ [101]. Up to geometric factors of order unity that arise from the deviations from perfect isotropy of typical ion emission, the minimum Doppler temperature is achieved at a detuning from atomic resonance exactly at the half maximum on the red side of the transition and is given by [64]

$$T_{min} = \frac{\hbar\Gamma}{2k_B} \sqrt{1 + \sigma} \quad (2.12)$$

2.3 Doppler cooling - a quantum perspective

Since it will be relevant to subsequent chapters, it is helpful to understand what happens to atomic resonances when one starts dealing with trapped rather than free particles. Several other features of laser cooling of ions, in particular a dressed state picture of the cooling of a trapped ion to discrete oscillator states and a mechanism by which to cool below the Doppler limit come out of this treatment. To begin, a fully quantum Hamiltonian for the motion of the ion in the trap is needed. As stated before, an ion in a Paul trap is very nearly a harmonic oscillator, so the Hamiltonian used for solving this problem in one dimension is

$$\hat{H} = \frac{\hat{p}^2}{2m} + \frac{1}{2}m\Omega_{trap}^2\hat{x}^2 + \underbrace{\frac{\hbar}{2}\omega\hat{\sigma}_z}_{internal} + \underbrace{\hat{H}^{ion-photon}}_{interaction} \quad (2.13)$$

The interaction Hamiltonian takes the form

$$\hat{H}^{ion-photon} = \frac{\hbar\Omega}{2} \left(\underbrace{|1\rangle\langle 2|}_{\hat{\sigma}_-} + \underbrace{|2\rangle\langle 1|}_{\hat{\sigma}_+} \right) \left(e^{i(k\hat{x}-\omega t)} + e^{-i(k\hat{x}-\omega t)} \right) \quad (2.14)$$

Here, Ω is the Rabi frequency as defined in the previous chapter. This Hamiltonian can be very clearly understood as coupling the light with the internal states of the ion. Going to the interaction picture using the unperturbed oscillator Hamiltonian introduces the trapping potential into the interaction Hamiltonian. This will contain rapidly oscillating terms with exponential factors $e^{\pm i(\omega_0+\omega)t}$, which will be dropped as before. In this quantum description, this is the equivalent of the rotating wave approximation which was made in the classical theory. Also, the position operator \hat{x} of the ion will be replaced with the oscillator raising and lowering operators $\hat{x} = \sqrt{\frac{\hbar}{2m\Omega_{trap}}} (\hat{a}u^*(t) + \hat{a}^\dagger u(t))$. The $u(t)$'s are related to solutions of the Mathieu equation and contain complex exponentials of the RF drive frequency.

At this point an important parameter in the context of laser cooling, the Lambe-Dicke

parameter $\eta \equiv k\sqrt{\frac{\hbar}{2m\Omega_{trap}}}$ should be introduced. Roughly speaking, this parameter is the ratio of the photon recoil energy to the trap secular motion kinetic energy. Using this, the interaction now takes the form

$$\hat{H}^{ion-photon} = \frac{\hbar\Omega}{2} \left[\hat{\sigma}_+ e^{i\eta(\hat{a}u^*(t) + \hat{a}^\dagger u(t)) - i\delta t} + \hat{\sigma}_- e^{-i\eta(\hat{a}u^*(t) + \hat{a}^\dagger u(t)) + i\delta t} \right] \quad (2.15)$$

This expression becomes much more revealing once it is expanded to lowest order in η

$$\hat{H}^{ion-photon} = \frac{\hbar\Omega}{2} \hat{\sigma}_+ \left[1 + \sum_{n=-\infty}^{+\infty} i\eta C_{2n} (\hat{a} e^{-i(\Omega_{trap} + n\Omega_{RF})t} + \hat{a}^\dagger e^{i(\Omega_{trap} + n\Omega_{RF})t}) \right] e^{-i\delta t} + h.c. \quad (2.16)$$

Looking at the $n = 0$ term $\frac{\hbar\Omega}{2} \hat{\sigma}_+ [1 + i\eta (\hat{a} e^{-i\Omega_{trap}t} + \hat{a}^\dagger e^{i\Omega_{trap}t})] e^{-i\delta t} + h.c.$, one finds three resonances, each with its own characteristic Rabi frequency. There is the so-called carrier transition at $\delta = 0$ with an unaltered Rabi frequency $\Omega_{NN} = \Omega$, a *red* sideband at $\delta = -\Omega_{trap}$ with a Rabi frequency equal to $\Omega_{N,N-1} = \eta\sqrt{N}\Omega$ and a *blue* sideband at $\delta = \Omega_{trap}$ with a frequency $\Omega_{N,N+1} = \eta\sqrt{N+1}\Omega$, where N is the occupation number of the ion's motional state and arises from the normalization of the oscillator raising and lowering operators. The subscripts used to differentiate the effective Rabi frequencies of the different sidebands are meant to suggest a dressed state picture of the atomic internal state and phonon number N . Red sidebands decrease the phonon number by one, that is, they connect the states $|g, N\rangle$ and $|e, N-1\rangle$. Likewise, blue sidebands connect the states $|g, N\rangle$ and $|e, N+1\rangle$. At higher values of the summation index n are additional sidebands, now at $\pm\Omega_{RF}$ known as micromotion sidebands. These are suppressed by the coefficients C_{2n} arising from the power series solution to the Mathieu equation and an additional factor of η . Figure 2.3 shows this spectrum of ion-trap resonances.

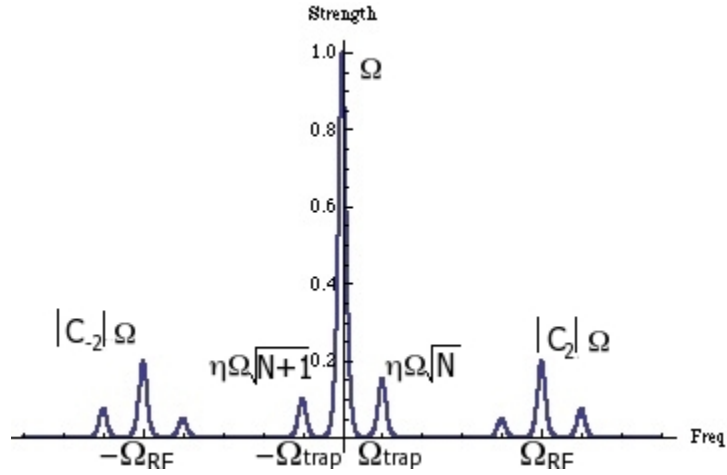


Figure 2.3: Characteristic spectrum of a narrow, for example dipole-forbidden, transition under the influence of a trapping potential. Vertical units are arbitrary. Micromotion sidebands at $\pm\Omega_{RF}$ are suppressed by a factor $|C_{\pm 2}|$. Secular motion sidebands on those transitions are suppressed by an additional factors of $\eta\sqrt{N}$ and $\eta\sqrt{N+1}$.

2.4 Trapping and cooling Ba^+

Finally, with all the general background of atom-light interactions, ion trapping and Doppler cooling out of the way, it is time to make the discussion specific to the ion species that will be used for the entirety of this work. Ba^+ was the first ion to be trapped and Doppler cooled and has a long history in high precision studies of atomic structure. Comprehensive studies of excited state lifetimes [67], hyperfine parameters of the odd isotopes $^{135}\text{Ba}^+$ and $^{137}\text{Ba}^+$ and isotope shifts [3, 104] and branching ratios [60] have all been performed. Considerable interest in precise measurement of the hyperfine structure of the $5D_{3/2}$ state is motivated by the potential to measure the nuclear octupole moment [9]. To date, this has only been performed in ^{133}Cs and the result was found to differ substantially from the value predicted by calculations of nuclear structure [45]. Ba^+ represents perhaps one of the best ions in which to observe atomic parity violation, since the $6S_{1/2}$ state acquires a small ($\sim 10^{-11}$) $6P_{1/2}$ component causing a parity-violating vector light shift on the 2051 nm $6S_{1/2} \rightarrow 5D_{3/2}$ quadrupole transition [41, 90]. The 2051 nm $6S_{1/2} |F = 2; m_F = 0\rangle \rightarrow 5D_{3/2} |F' = 2; m'_F = 0\rangle$ “clock”

transition also has potential for use as an optical frequency standard [93]. Because of this possibility and the fact that barium lines can be observed in quasar spectra, barium is one of several useful species for comparisons between laboratory and astronomical transition frequency measurements. In principle, it has enhanced sensitivity to space-time variation of the fine structure constant [33].

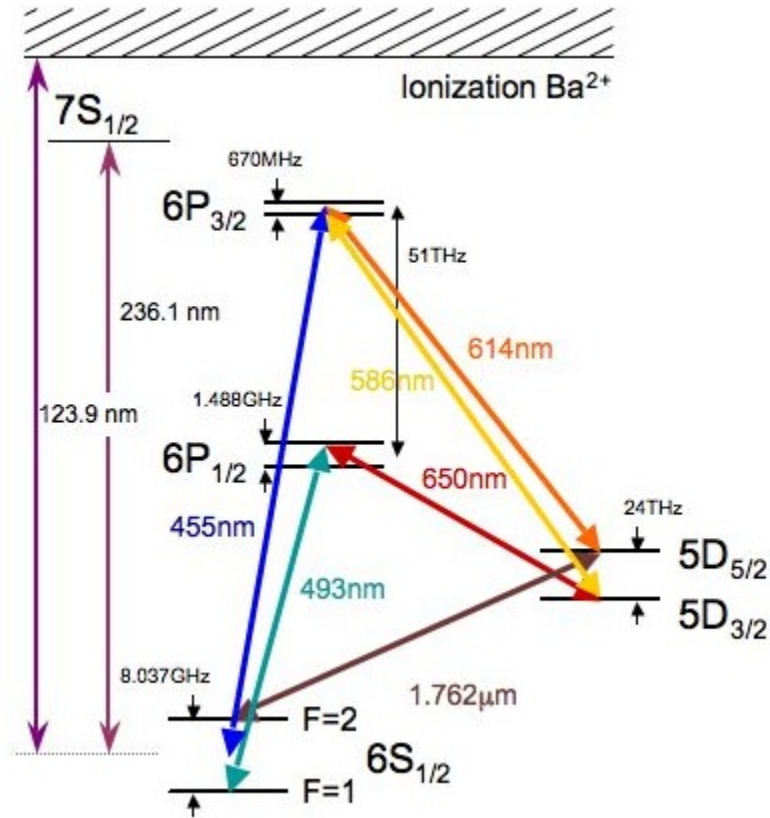


Figure 2.4: Several lowest energy levels and wavelengths of transitions among them in $^{137}\text{Ba}^+$. With a repump laser at 650 nm to excite the ion out of the $5D_{3/2}$ state, the 493 nm transition between $6S_{1/2}$ and $6P_{1/2}$ is used for cooling and fluorescence detection. $^{138}\text{Ba}^+$ is identical except the hyperfine structure (only partially depicted here as the state splittings in the S and P states) is not present. Zeeman sublevels are not shown. The next lowest-lying states are well into the UV, so no excitation even with broad band excitation discussed in subsequent chapters will occur to them.

From the point of view of those interested in trapped ion quantum computation, Ba^+ has several features that make it perhaps the best candidate ion out of the ion species currently

under investigations (Table 1.1). First of all, both the useful isotopes $^{138}\text{Ba}^+$ and $^{137}\text{Ba}^+$ are abundant enough that isotopically enriched samples are unnecessary (see Table 2.1). Useful qubit schemes, both optical and hyperfine exist [26]. Secondly, the cooling structure is extremely simple, requiring only two lasers both of which are in the visible and available as standard diodes with one doubling stage. Most other ions have cooling transitions that range from either very blue or well into the ultraviolet (UV). Besides simply being easier to work with visible light, UV light does not transmit well in single-mode optical fiber, making long-distance remote entanglement experiments [99] mediated by UV photons impossible. Additionally, the low-lying D states are available for state detection by means of electron shelving. These states decay only by electric quadrupole transitions and even then only at very long wavelength (1.762 μm in the case of the $5\text{D}_{5/2}$ state), so the suppression of the decay rate by a factor of λ^5 makes them very long-lived.

Table 2.1: Values for various quantities of interest of the stable barium isotopes. The second column is the shift in the $6\text{S}_{1/2} \rightarrow 6\text{P}_{1/2}$ transition with respect to $^{138}\text{Ba}^+$. For the odd isotopes, this is the position of the centroid of the hyperfine components.

Isotope	$\Delta\nu$ (MHz) [104]	Abundance (%) [21]
138	-	71.698
137	271.1	11.232
136	179.4	7.854
135	348.6	6.592
134	222.6	2.417
132	278.9	0.101
130	355.3	0.106

The trap geometry, as mentioned before, is of the linear Paul trap variety with center-to-center RF electrode separation of 0.036" and an endcap electrode separation of 0.090" as measured with the cooling laser focus mounted on a three-axis translation stage. The electrodes themselves are 0.017" diameter tungsten rods, with the endcaps electrochemically etched with KOH solution to a sharp tip. The two trap RF electrodes are shorted inside the

trap, as are the ground electrodes. While this diminishes the possible phase difference of the RF between the two rods, it means that DC bias voltages applied to the RF and ground electrodes that would be useful for micromotion compensation only shift the ion position with their gradient. This form of excess micromotion compensation was attempted but controlling micromotion remains a significant issue for this particular trap. The electrodes are insulated from the trap structure with alumina spacers and the entire piece is placed in a Kimball PhysicsTM 4-1/2" spherical octagon vacuum chamber with eight anti-reflection coated fused silica viewports, two placed as close to the trap as possible to accommodate photon collection optics, and the other six for laser access. Two additional ports are occupied by RF and high voltage feed-through's. The trap vacuum structure is baked for about a week and continuously pumped by a Varian Star-CellTM 20 l/s ion pump and periodically by a titanium sublimation pump. It has maintained UHV at a level of under 2×10^{-11} torr for several years with minimal effort, partially thanks to the fact that barium is itself an excellent getter.

The RF for the trap is generated by a Hewlett Packard 8640B function generator amplified to approximately 1-2 W and inductively coupled into the trap by means of a helical resonator with a resonant frequency $\Omega_{RF} = 2\pi \times (12.38)$ MHz and a Q of several hundred [65]. The ground electrodes can be accessed to allow modulation by means of an SMA coaxial connector on the resonator. The high voltage feed-through for the endcaps and barium ovens is heavily filtered by a network of low-pass pi-filters to prevent RF pickup from entering these power supplies. Typical endcap voltage is 400-500 V for trapping and 700 V for cooling. After considerable effort, we have found that trapping is facilitated by lower trapping potentials while cooling improves at a slightly higher value. In addition to the RF and DC fields needed for trapping, we apply a magnetic field of a few Gauss by running several amps of current (typically 2.1 A) through a coil with a diameter of approximately 4" and about 200 turns to break the Zeeman state degeneracy which would otherwise lead to dark states during

Doppler cooling [11]. Smaller coils on the two other spatial axes carry lower current to allow steering of the magnetic field axis for optical pumping, more details on that to follow in Chap. 6.

The barium atomic beam source is simply a 1 mm diameter, 1 cm long alumina tube wrapped with a tungsten wire through which current is run to heat the natural barium in the tube. To prevent coating optical access ports with barium which would render them rather useless neutral density filters, the atomic beam is first collimated simply by placing an aperture immediately in front of the oven. This aperture is also useful for keeping the transverse velocity of the beam low to aiding in photoionization as well as for shielding the trap itself from the heat radiated during loading. The neutral barium can be ionized by a number of means. Initially, electron bombardment was used by an electron gun made from a heated filament and accelerating plate. This is a less than ideal method as it tends to charge dielectric surfaces in the trap contributing to unwanted patch potentials, and is not isotope selective. A second method employed was an attempt at photoionization using a xenon flash-lamp focused in the trap center. This lamp has considerable spectral content at wavelengths shorter than 237.1 nm. It was unclear whether this lamp directly photoionized the barium in the atomic beam or if it created photoelectrons from the rods, as the short wavelength photons were energetic enough to overcome the work function of the tungsten.

Inspired by the success of two-step photoionization [100], an external cavity diode laser (ECDL) at 791 nm was constructed. This laser excites barium on a $6s6s^1S_0 \rightarrow 6s6p^3P_1$ intercombination transition. From there a pulsed nitrogen laser at 337 nm excites the electron to continuum, ionizing the barium. The 791 nm laser was aimed as perpendicular to the atomic Ba beam as possible to minimize the first-order Doppler shift due to the atoms' motion. Although the intercombination line has a 50 kHz linewidth in principle, a 640 MHz FWHM width was observed while loading [27]. This is sufficiently narrow to separate ^{137}Ba from ^{138}Ba , but ^{136}Ba is loaded occasionally. Since the loading rate is sensitively dependent

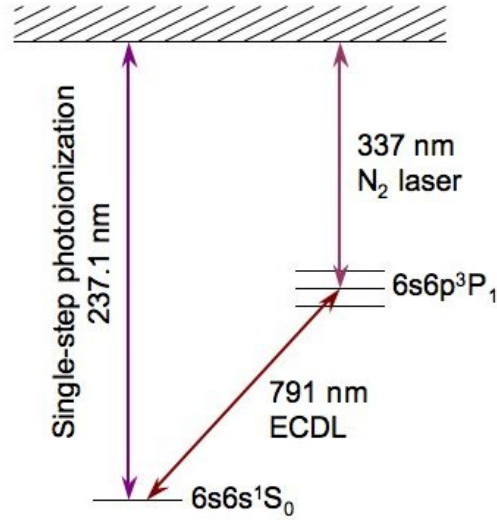


Figure 2.5: Partial energy level diagram of neutral barium to highlight the two photoionization schemes employed over the course of this work. The two-photon scheme has the advantage of isotope selectivity but is more sensitive to Doppler shift of the atomic beam.

on both the oven current and pulse rate of the N_2 laser, both of these are kept quite low to maximize the probability of loading only one ion at a time. The two photoionization schemes are shown in Fig. 2.5.

Once a neutral barium atom is ionized near the trap center, it experiences the trapping field of the quadrupole potential and quickly becomes localized as the cooling lasers bombard it with photons. The main transition of interest is the $6S_{1/2} \leftrightarrow 6P_{1/2}$ transition at 493.4 nm . This light is generated by a home-built 200 mW 986 nm ECDL, frequency-doubled in a non-critically phase-matched (temperature-tuned) potassium niobate ($KNbO_3$) Type-I ooe nonlinear crystal in a bow-tie enhancement cavity. The crystal itself is actually cut for second harmonic generation of a slightly shorter wavelength, and owing to the steep slope of the phase-matching temperature vs. laser wavelength, rather than heating to slightly over room temperature the crystal is held near 60°C . The cavity is locked using Pound-Drever-Hall stabilization [12], with an error signal created by directly modulating the current on the laser diode at 16 MHz through an isolation transformer and bias-T. The cavity specifications

and modulation circuit are pictured in Fig. 2.6 (a) and (b), respectively. Cavity locking is achieved with a ADuC7020 digital microcontroller servo laid out in Fig. 2.7 [25]. For the most efficient cooling, the polarization of this laser is elliptical and directed onto the ion perpendicular to the quantization axis defined by the magnetic field (refer to the dipole radiation patterns in Fig. 1.4 (a)).

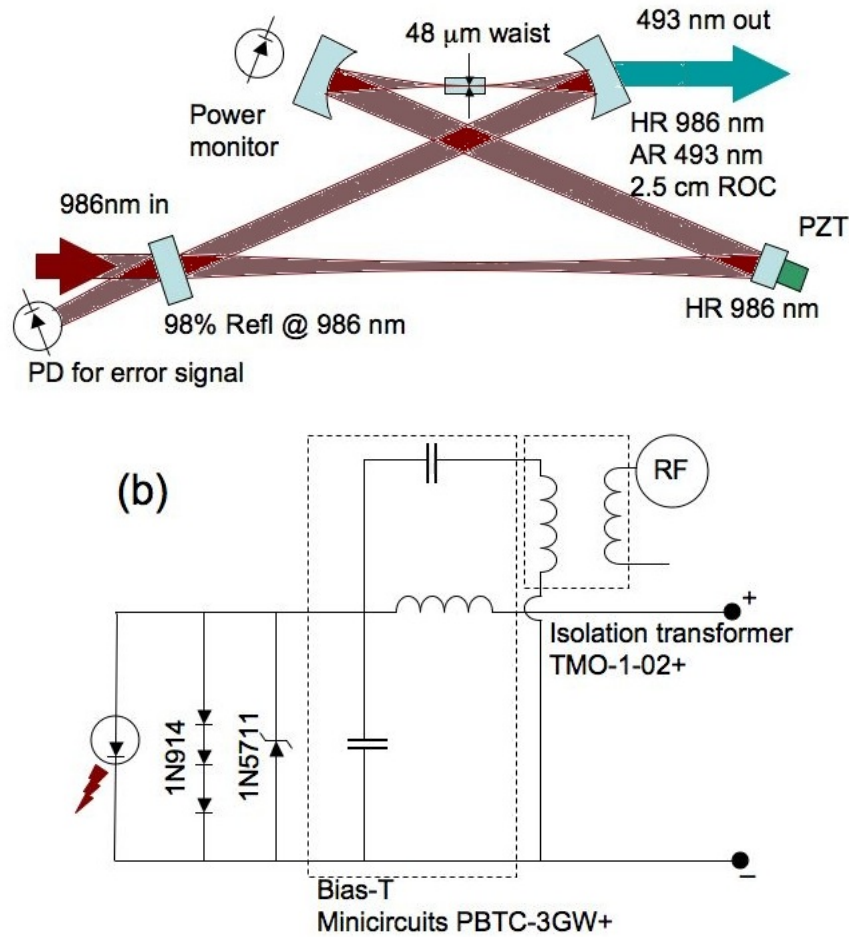


Figure 2.6: (a) Layout of second harmonic generation cavity for 493 nm cooling light. The curved mirror separation is 27 mm, just under the maximum allowed for stability as calculated by the transfer matrix approach [57]. Mode-matching is about 60%, cavity finesse approximately 50 and free spectral range is approximately 440 MHz. (b) Bias-T for modulation of the diode lasers current for PDH error signal. The isolation transformer separates the Bias-T's ground from the laser's ground and the 1N914 and 1N5711 Schottky diodes provide over-voltage and reverse bias protection respectively.

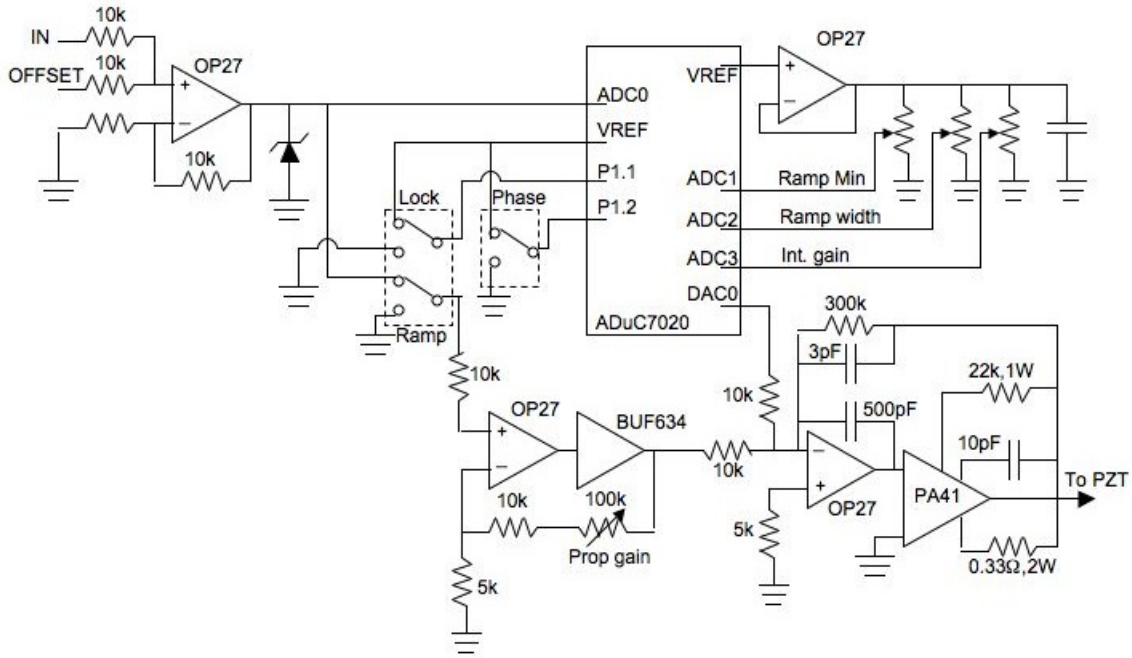


Figure 2.7: Cavity servo for SHG of 493 nm cooling light. The ADuC7020 is mounted on an evaluation board for easy uploading of scripts. In this case, it acts as both a ramp generator for cavity scanning and a digital integrator with a reacquire feature should the cavity fall out of lock. Adapted from [27].

Referring to the energy level diagram of Ba^+ , one finds that the $6P_{1/2}$ state can decay to the $5D_{3/2}$ state via a dipole-allowed transition. The branching ratio for this decay is approximately 27% [53] and the lifetime of the D state is 79 s [106]. This requires a second laser at 649.7 nm to *repump* the ion back in to the $6P_{1/2}$ state. The 650 nm laser has the same circuit to allow current modulation for the addition of sidebands for cooling $^{137}\text{Ba}^+$. The complete, closed cooling cycle is then comprised of the two wavelengths, 493 and 650 nm. The two colors are combined on a dichroic mirror and fiber coupled to send to the trap. Even though the fiber coupling diminishes the power available by a significant fraction, it has a number of advantages. It ensures perfect collinearity of the two beams, allows changes to be made before the trap to the optical layout without disturbing the beam alignment to the ion and serves to clean the mode to reduce halo and background scatter off trap surfaces.

After the fiber, there is approximately $50 \mu\text{W}$ of red light and $5 \mu\text{W}$ of green, entirely sufficient for cooling. When the ion is in this cycle, it fluoresces photons at 493 nm at a rate of a few times $10^7/\text{s}$. We collect these photons for state detection, as well as to simply know that an ion is in the trap.

Before moving on to state detection, a word on laser stabilization is necessary. The natural linewidth of the $6P_{1/2}$ state is approximately 20 MHz and although the quantity of 493 nm light power broadens this, the line width and long-term drift of a free-running ECDL would make Doppler cooling impossible. Therefore some sort of laser stabilization is necessary. While it is painfully simple with neutral atoms, e. g. Cs and Rb where a simple vapor cell provides a means of locking to the same species, ions are slightly more difficult. Discharge tubes and hollow cathode lamps can be used, as well as performing Doppler-free spectroscopy on molecular species with transitions in a similar wavelength range. The latter

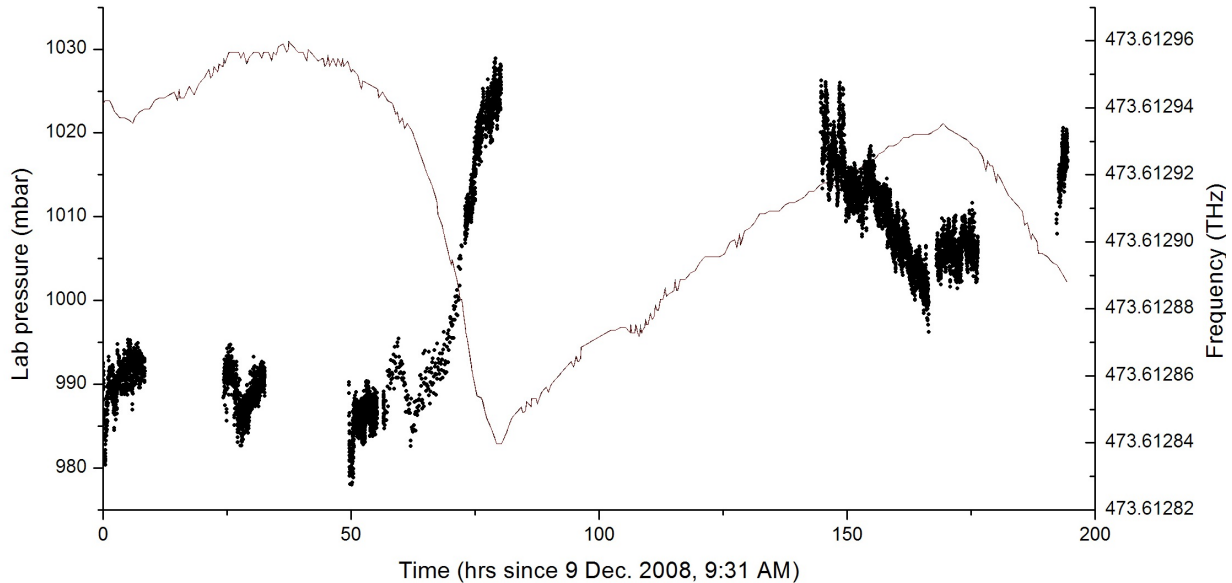


Figure 2.8: Atmospheric pressure (solid red line) vs. measured HeNe frequency (black dots), which it is safe to assume was stable during this time period so any measured drift can be taken to be a drift in the wavelength meter. From this data, it can be seen that the wavelength meter has a lag time of approximately 6 hrs. and drifts about 3 MHz/mbar .

was used for some time; a lock to diatomic tellurium for the green and iodine for the red. These systems require the majority of the laser's power be diverted to the lock and are cumbersome, often requiring a significant shift of relative laser and lock frequencies with acoustic optic modulators to reach both the lock and cooling frequencies. The situation becomes even more inconvenient when one wants to switch from one isotope to another. Eventually the solution which proved most convenient was a digital system based on a High-FinesseTM WS7 wavelength meter. The wavelength reading is digitized and sent to the data acquisition system, the error signal calculated and the feedback returned to the laser's grating arm piezo via a 12-bit DAC. A fivefold voltage divider ensures that the step size generated by the DAC is less than 1 MHz of laser frequency, which is actually well beyond the resolution of the wavelength meter. The wavelength meter itself however was found to drift in frequency, as shown in Fig. 2.8 where its measured frequency is referenced to a stabilized helium-neon (HeNe) laser. Although temperature plays a role as well, atmospheric pressure was found to be the more significant environmental parameter. For daily operation the wavelength meter is referenced to the HeNe laser and its measured frequency adjusted by this offset. The cooling and repump lasers are routinely locked to about ± 5 and 10 MHz, respectively, which is sufficient for reliable cooling.

Ion fluorescence is collected through a recessed fused silica viewport with a Mitutoyo NA=0.28 microscope objective positioned perpendicular to the quantization axis at a distance of about 2 cm from the ion. Spatial filtering is accomplished by positioning a 100 μm pinhole at the focus of this objective and substantially reduces what would be an otherwise overwhelming background of laser light scatter from the trap. For imaging, the light is refocused by a 25 cm doublet lens followed by a 493 nm interference filter. Although this filter reduces the collection of photons by approximately a factor of two, it enables running without worry about scatter from room lights. The ion can either be imaged by an Andor LucaTM electron-multiplied CCD camera, or the photons can be counted by a pair

of HamamatsuTM photomultiplier tubes (PMT's), mounted on opposite output ports of a polarizing beam splitter. The camera is mainly used for alignment and evaluation, while the PMT's are used for photon counting during experiments. A typical fluorescence signal, demonstrating bright and dark counts and a histogram of the data is shown for illustrative purposes in Figs. 2.9 (a) and (b).

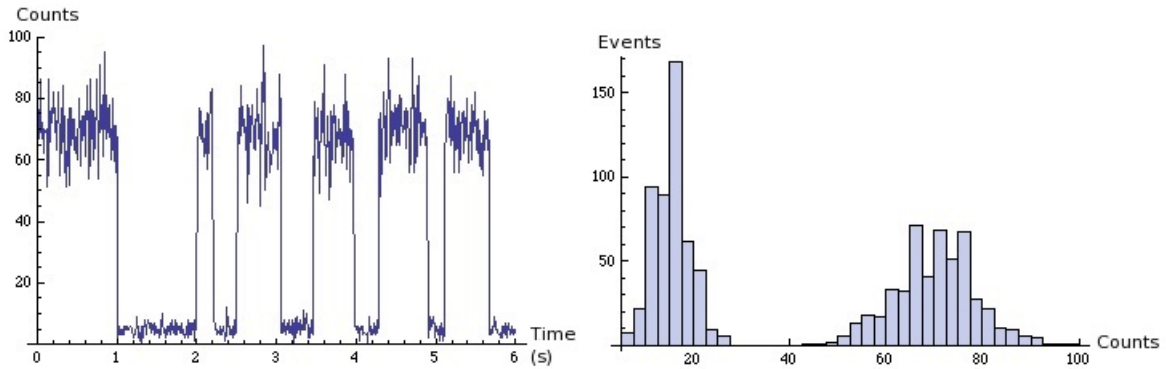


Figure 2.9: (a) Time plot of single ion fluorescence while turning on and off the 650 nm laser to demonstrate the difference between bright and dark count rates. Shining the $1.762 \mu\text{m}$ laser on the ion at the same time would produce a similar signal known as a “telegraph” only on a much faster time scale. (b) Histograms of multiple 20 ms exposures of the ion with dark counts near zero (non-zero due to background scatter) and bright counts averaging approximately 75 counts. An appropriate cut-off for state discrimination here might be chosen at 40 counts.

The final laser in the system is a Koheras AdjustikTM thulium-doped fiber laser at $1.762 \mu\text{m}$ to address the $6S_{1/2} \rightarrow 5D_{5/2}$ quadrupole transition. This laser is stabilized via a similar PDH locking scheme as the cooling laser to a high-finesse ZerodurTM cavity enclosed in a temperature controlled vacuum of about 10^{-6} Torr. The laser has a linewidth of < 5 kHz and is therefore sufficiently narrow to address individual Zeeman or hyperfine transitions between the ground and excited states. The $5D_{5/2}$ state has a lifetime of 32 s [106] during which neither the 493 nm nor the 650 nm light is resonant with any available transition. When the ion is in this state, it is said to be “dark,” since only background 493 nm light will be collected by the PMT. If after the experimental cycle the ion is still in the cooling cycle

or “bright” state, it can be concluded that the $1.762\ \mu\text{m}$ light was never resonant with any available $6S_{1/2} \rightarrow 5D_{5/2}$ sublevel transition. State selective detection via shelving can then be performed by imposing a cutoff between “bright” and “dark counts.” Applying a second pulse of $1.762\ \mu\text{m}$ light will rotate the ion back down to the S state, bringing it back to the cooling cycle for the experiment to continue.

The beam path of each laser between its output and the trap window contains a number of optical elements to allow experimental control. For the 650 nm laser, 40 dB of optical isolation and beam reshaping using an anamorphic prism pair is required. The light is then focussed through an acoustic optic modulator. Besides introducing a frequency shift, the AOM acts as a fast optical shutter (rise time $<10\ \text{ns}$, as fast as $2\ \text{ns}$ at the expense of diffraction efficiency), with the RF drive switched by Minicircuits ZYS-50D-R TTL-controlled switches. The main portion of the 493 nm cooling light is sent through an AOM and then coupled into a single mode fiber with the 650 nm light on a dichroic mirror. Before switching, a small fraction of the 493 nm light is picked off to act as an optical pumping beam. This light is switched independently of the main cooling beam. Before it enters the trap, there is a Glan-Thompson polarizer and a quarter-wave plate to allow polarization control, which is critical for optical pumping (more detail in Chap. 5). Details about the $1.762\ \mu\text{m}$ laser are in Section 5.3.

The entire experiment is computer-controlled through two National InstrumentsTM data acquisition cards (a PCI-6220 and a PCIe-6351) which can alternately use hardware or on-board timing and can be triggered with the phase of the wall voltage for magnetic-field sensitive experiments. A multi-channel pulse sequencer based around a field programmable gate array (FPGA) with accompanying direct digital synthesizer (DDS) has also been developed and allows for the creation of multiple signals of arbitrary amplitude, phase and envelope with user-defined phase and timing relations to one another. A block diagram of the entire system is shown in Fig. 2.10.

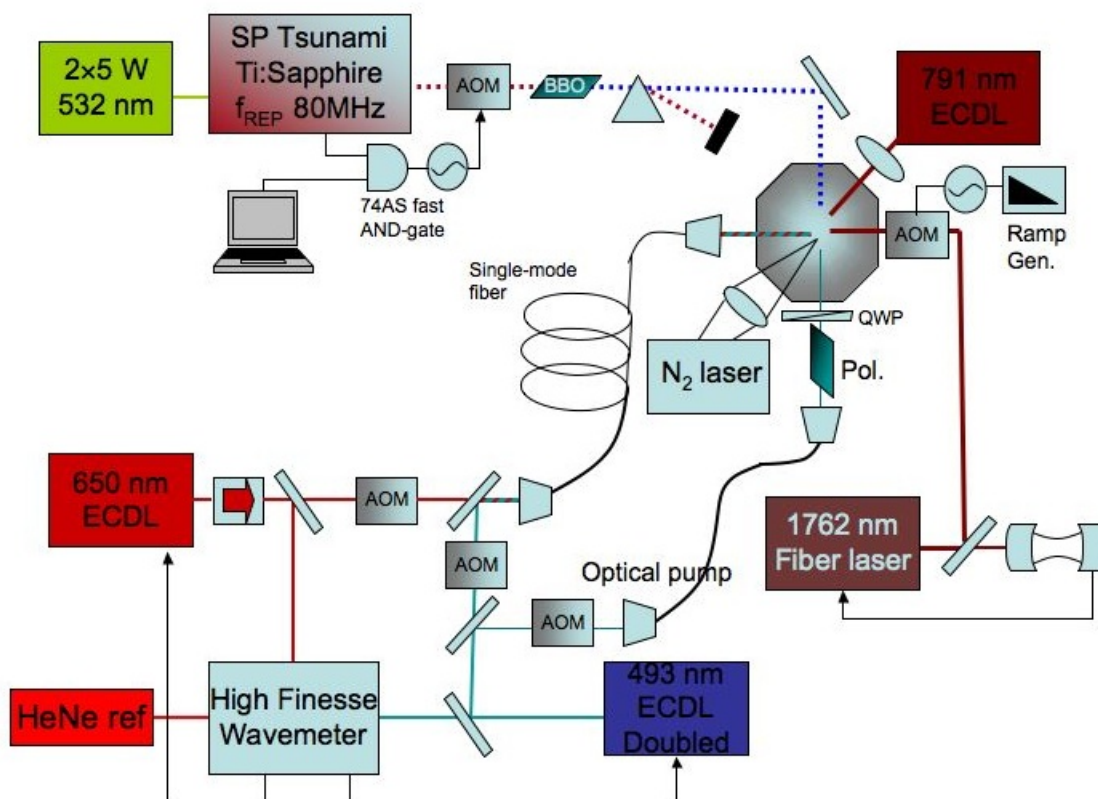


Figure 2.10: Block diagram layout of the entire experimental apparatus, without collection and imaging optics for clarity. See text for a description of the cooling, detection and ionization lasers. The function of the Ti:Sapphire laser will be addressed in Chap. 3.

3 ULTRAFAST INTERACTIONS

If you can't get rid of the skeleton in your closet, you'd best teach it to dance.

- George Bernard Shaw

The previous chapter gave an outline of the elements of the experimental apparatus that pertain to cooling, state manipulation and detection. The light sources that perform these tasks are all continuous wave, or CW. Another class of lasers equally useful in quantum computation with trapped ions is the family of mode-locked lasers, which emit intense, coherent pulses of light as short as a few femtoseconds if extreme care is taken in their design. Peak power in such lasers can be extremely high (up to megawatts and even higher with regenerative amplification) owing to the brief duration of the pulse. The first mode-locked lasers were Argon ion-pumped dye lasers in the 1970's, followed by the creation of the modern (though aging) work-horse of the field, the titanium (Ti^{3+})-doped sapphire (Ti:Sapphire) laser, developed in 1986 [75]. Other solid-state mode-locked lasers exist, YAG and vanadate lasers with various rare-earth dopants or the family of vibronic lasers such as forsterite, alexandrite, LiCAF and LiSAF where the chromium ion plays the role of titanium just to name a few. However, none have the broad gain bandwidth (150 THz) of the Ti:Sapphire laser. More and more, mode-locked fiber lasers are replacing solid-state systems because of their robust operation and low maintenance, although they have yet to reach single optical cycle pulse lengths.

Mode-locked lasers have found their way into the field of trapped ion quantum compu-

tation in a number of ways because of the fact that the high electric field intensity can very quickly drive excitations in ions. Recall that the Rabi frequency of a particular laser-driven transition is proportional to the local electric field at the ion. Also, being able to drive an ion into an excited state much faster than the characteristic decay time of that state (typically < 10 ns for a radiative transition) has enabled many protocols that require single photon emission. Remote entanglement [72], quantum teleportation [80], ultrafast quantum gates [50] and single-pulse driven Raman transitions [16] are all applications of pulses much shorter than the lifetime of radiative transition useful for quantum computation with trapped ions.

3.1 Mode-locked lasers

All mode-locked pulsed lasers operate on the same principle, but achieve their operation in a variety of ways. This discussion will be as general as possible, but is geared toward the operation of Ti:Sapphire lasers since the entirety of the work presented here was performed with such a laser. The basic design of a mode-locked laser is the same as any CW laser, that is a reflective optical cavity with one lossy side built around a gain medium pumped optically with continuous, coherent light. The gain medium here in contrast to CW lasers, is specifically chosen to have a broad gain bandwidth (up to 100 THz). For comparison, an atomic transition line in a gas laser or the band gap between conduction bands in a semiconductor have widths of 100's of MHz. A Ti:Sapphire laser has the broadest gain spectrum of any solid-state system and can in principle operate from 600 nm to nearly 1 μm , although the Ti^{3+} dopant fraction and other properties of the crystal generally limit particular lasers to slightly narrower regions of this spectrum. The term “mode-locked” refers to the longitudinal cavity modes, which form a comb of frequencies spaced by the free spectral range (FSR) of the cavity with length L ($FSR \equiv \frac{c}{2L}$), which are made to oscillate with a fixed phase relationship to one another. The frequency domain picture of the laser's

operation then is a comb of equally spaced modes with an overall intensity envelope given by the gain profile of the lasing medium and laser cavity parameters. The time domain picture is then a train of equally spaced pulses with a pulse width $\tau_p = \frac{TBP}{N\Delta\nu}$, where TBP refers to the time-bandwidth product, a factor of order unity specific to the functional shape of the pulse, N the number of simultaneously lasing modes in the cavity and $\Delta\nu$ the spectral bandwidth of the gain medium. Ti:Sapphire lasers (and most other *passively* mode-locked lasers for that matter) typically have or are assumed to have a hyperbolic secant electric field temporal profile with a $TBP = 0.315$ [20].

The mode-locking is achieved by a number of ways which fall into two broad categories, active and passive mode-locking. Actively mode-locked lasers make use of some sort of externally-timed optical shutter, such as an AOM, synchronized to the round-trip time of a pulse in the cavity. Passively mode-locked lasers use a material, a saturable absorber, which is only transparent to light of sufficiently high intensity, and therefore make the cavity unfavorable for CW operation. Such materials have a significantly high third-order component to their electric susceptibility tensor $\chi^{(3)}$ that they acquire an intensity dependence to their index of refraction $\Delta n = \lambda KI$, where λ and I are the wavelength and intensity of the light, respectively, and K is known as the Kerr constant of the medium. The trick is then to make the cavity itself unstable for CW operation, often done by closing a slit on the circulating beam or adjusting the length of the cavity around the Ti:Sapphire crystal. Lasers mode-locked in this way are referred to as Kerr-lens mode-locked lasers and tend to have the shortest pulse lengths attainable. The last element necessary for stable mode-locked operation is a means by which to compensate the group velocity dispersion (GVD) that occurs within the laser cavity due to the fact that the many different wavelengths operating concurrently experience wavelength-dependent indices of refraction which would otherwise lead to relative and randomly-evolving phases of the different frequency components. This is exacerbated by the self phase modulation (SPM) introduced by the Kerr effect itself which

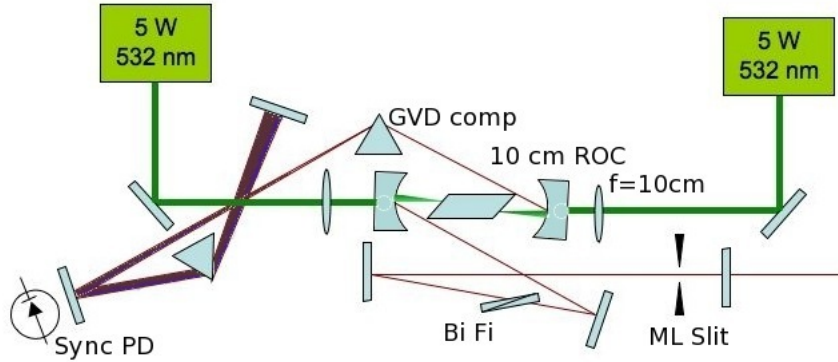


Figure 3.1: Mode-locked Ti:Sapphire laser used for this experiment based on Coherent MiraTM. *Bi Fi* birefringent filter for frequency tuning, *ML slit* used for chopping out CW mode and starting mode-locked operation, *GVD comp* prism pair for dispersion compensation, *Sync PD* fast photodiode used to synchronize pulse picking AOM to laser for experiments

it has already been noted is an intensity dependent index of refraction. GVD and SPM are compensated by either prism pairs or “chirped” mirrors which allow the slower wavelengths (blues) to “catch up” to the faster ones (reds).

The laser used for the majority of the work presented here is a design based on a heavily modified Coherent MiraTM. During the course of this work it has been pumped either by a single 15 W Spectra-Physics MillenniaTM at 532 nm or two 5 W versions of the same laser focussed into opposite ends of the Ti:Sapphire crystal. It has a repetition rate of 76 MHz and a pulse width of 400 fs. This corresponds to a spectral width of about 125 GHz assuming transform-limited pulses. By design, this is broad enough to cover the frequency splitting between hyperfine levels of the ground state of $^{137}\text{Ba}^+$ (8.037 GHz) but not so wide that transitions to undesired excited states are driven (6P states have a fine structure splitting of over 50 THz). By changing mirror sets, the laser can be made to operate and mode-lock at any wavelength between 860 and 1020 nm, although the only two useful wavelengths are 910 and 986 nm, twice the wavelength of the $6S_{1/2} \rightarrow 6P_{3/2}$ and $\rightarrow 6P_{1/2}$ transitions in Ba^+ , respectively. The pulses are frequency-doubled via single pass through a $\beta\text{-BaB}_2\text{O}_4$ crystal.

A diagram of its optical cavity layout is shown in Fig. 3.1.

3.2 Ultrafast pulses & ions

To analyze what exactly one would expect to see when shining a pico- or femtosecond pulse on an ion, it is necessary to revert to the optical Bloch equations (Eqns. 1.8). Instead of having a steady field $\vec{E} = \hat{e}E_o \cos(\omega t)$ however, there is an additional time envelope function which will show up in the optical Bloch equations as a time dependence to the Rabi frequency Ω . In the case of mode-locked Ti:Sapphire lasers, that envelope is approximately a hyperbolic secant, given by

$$\vec{E} = \hat{e}E_o \operatorname{sech}\left(\frac{t}{\tau_p}\right) \cos(\omega t) \quad (3.1)$$

where the only new variable introduced is the pulse duration, τ_p . Believe it or not, this problem is actually solveable analytically. For culture's sake, it is worth noting that the exact solution is related to a hypergeometric function $\rho_{22} = e^{-i\delta} \sqrt{\frac{\xi(1-\xi)}{ab}} \frac{d}{d\xi} {}_2F_1(a, b; c; \xi)$, with $a = -b \equiv \frac{1}{2}\tau_p E_o$, $c \equiv \frac{1}{2} + i\tau_p(\delta - i\gamma)$ and $\xi \equiv \frac{1}{2}(1 + \tanh(t/\tau_p))$ [96]. For practical situations, we are actually only concerned with what happens in the limit $t \rightarrow \infty$ for nearly resonant pulses. In that case, the excited state population looks like

$$\lim_{t \rightarrow \infty} \rho_{22} = \sin^2\left(\frac{1}{2}\pi\tau_p E_o\right) \quad (3.2)$$

The argument of the sine can be related to the energy in the pulse $U \propto \int |\vec{E}|^2 dt$, giving $\rho_{22} = \sin^2(\alpha\sqrt{U})$, where in practice the factor α will depend on the transverse dimensions of the laser at the location of the ion. In the case of a three-level Lambda system like Ba^+ where the ion has two decay channels from the excited state, it is necessary to add a prefactor B less than one to account for the fact that the ion has a probability to end up in one of

the D states following excitation. The results of the calculation are displayed in Fig. 3.2 for different detunings of the central frequency of the pulse. At the maximum of the curve, a π pulse has successfully transferred the entire population to the excited state.

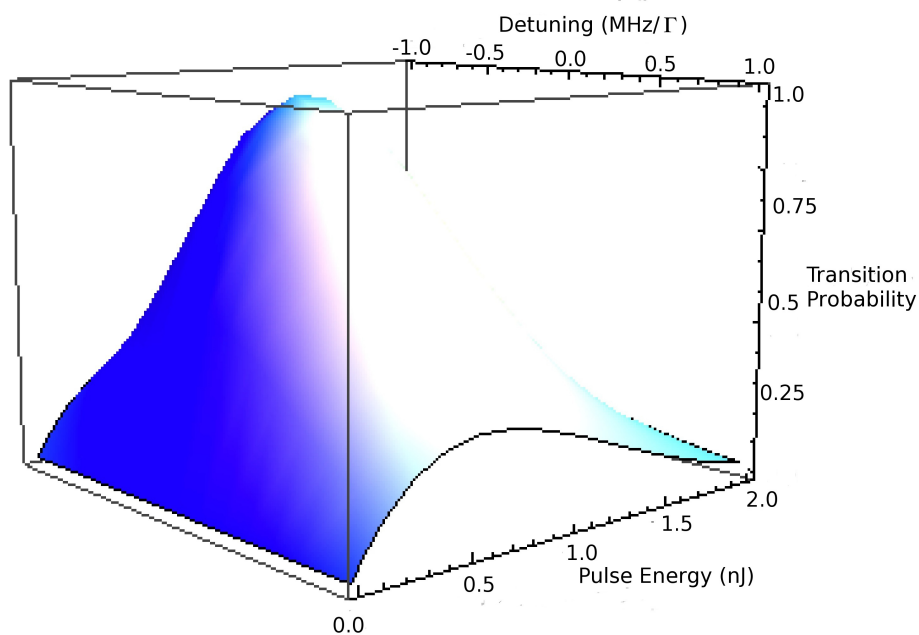


Figure 3.2: Numerical solution for the population of the $5D_{5/2}$ state after a 400 fs pulse has excited the ion to the $6P_{3/2}$ state using the six coupled optical Bloch equations. The profile for constant pulse energy is sech^2 and for constant detuning \sin^2 .

3.3 Single pulse selection

If pulses were sent onto the ion at the Mira's repetition rate of 76 MHz, S to P transitions would be driven on average after only two decay times had elapsed, causing the ion's state to quickly become a mess. For the purposes of realizing a π rotation on the spin state of the ion, it is necessary to use single pulses from the laser which would be available at the experimenter's demand. Since there is no external synchronization when using a passively mode-locked laser, a pick-off photodiode with a transimpedance amplifier based on an OPA

380 for approximately 90 MHz bandwidth was installed behind an imperfect laser cavity (see Fig. 3.1) mirror to pick up the pulse signal and synchronize the laser's operation to the experiment. The resulting signal is too small to be recognized for control by the DAQ system so must be amplified to a level which is TTL-compatible. This is accomplished with a chain of high-speed devices consisting of a UA733 video amplifier, a MAX933 high-speed comparator and finally a DS1040-A15 single-shot pulse generator with 5 ns pulse width. Even with fast electronics, the dead time of the DS1040-A15 causes it to miss every second pulse, effectively making the fastest possible operation equal to half the repetition rate of the Mira. When needed for the experiment, single-shot pulses from the DAQ card enter one input terminal of a Potato semiconductors PO74G08A 1.125 GHz bandwidth AND gate and the synchronization pulse train from the laser enter the other. The resulting pulse with 5 ns duration triggers an HP8310B pulse generator with variable delay. This allows monitoring of selected pulses on a fast photodiode to ensure that the trigger pulse is centered on the laser's pulse train. The same RF signal generators, amplifiers, switches and AOM's as are used to

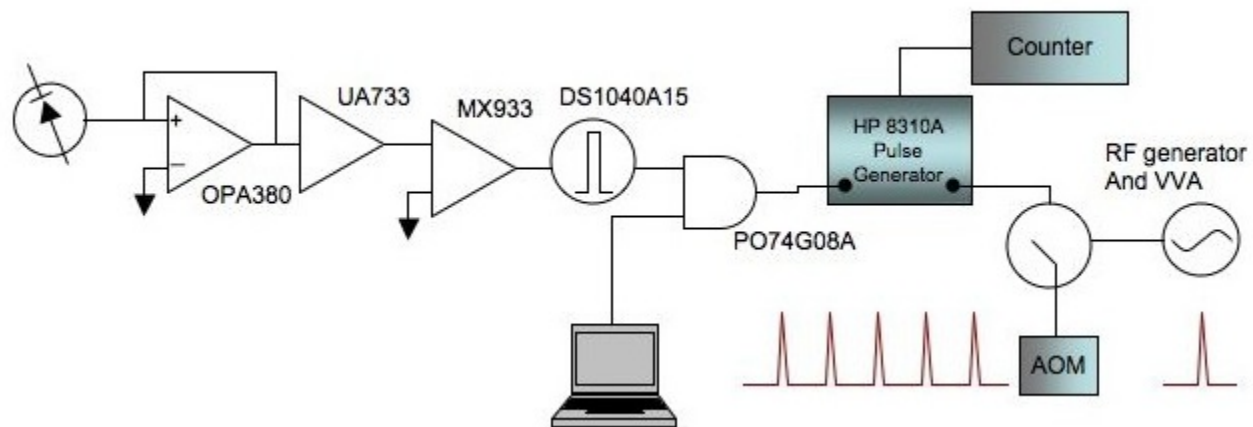


Figure 3.3: Pulse picker electronics, the function of individual elements is described in the text. The counter is used to monitor the trigger out from the HP 8310B and provides a way to count the number of times the switch is triggered. Approximately 3% of the trigger pulses are missed and these counts were removed from experiments.

switch on and off the cooling lasers are used to provide an optical shutter triggered by the TTL pulses from the 8310. Rather than being optimized for maximum deflection efficiency, the AOM in the beam path of the Mira is optimized for the fastest possible rise time, although it is still the bottleneck in the overall speed of the system and incomplete switching on and off leads to the leakage of laser pulses (not more than $\sim 3\%$ of the maximum intensity of the main peak) on either side of the selected pulse. These are highly attenuated in the SHG process which scales with the square of the intensity. The RF drive power, and hence the energy per laser pulse, can be adjusted via a DAC-controlled Minicircuits ZX73-2500 voltage variable attenuator (VVA). Fig. 3.3 shows the chain of electronics pictorially. A protocol to use pulse sequencer's capability to execute a phase-locked loop is under development and would in principle replace the DAQ trigger pulse and AND gate, greatly simplifying the operation of the system.

3.4 Rabi flop at 455 nm

The first experiments performed using the mode-locked pulses from the Mira were to excite the ion from the $6S_{1/2}$ state to the $6P_{3/2}$ at 455.4 nm by frequency doubling 910.8 nm Ti:Sapphire laser pulses rather than $6P_{1/2}$, because the available pump power was insufficient to provide enough power to mode-lock the laser at 986 nm. The experiment was performed by first turning off the cooling lasers, the 650 nm repump laser a few microseconds after the 493 nm cooling laser to ensure pumping to the ground state rather than the D state. A single pulse at 455.4 nm was then sent onto the ion, exciting it to the $6P_{3/2}$. From there, three allowed decay channels exist, the first back to the $6S_{1/2}$ state at 455.4 nm, the second to the $5D_{5/2}$ at 614.2 nm and the third to the $6D_{3/2}$ at 585.5 nm. If the ion decayed to either the ground state or to $5D_{3/2}$, it would appear bright when the cooling lasers were switched back on immediately after the pulse. If however, it went to the $5D_{5/2}$ state, it would be out

of the cooling cycle and appear dark. A high-power Luxeon Star orange LED with a central wavelength near 614 nm provided a means to excite the ion out of the dark state to begin a new run of the experiment. The process was repeated for different attenuation values on the VVA from the maximum 455nm pulse energy at about 1.6 nJ per pulse down to where no shelving was observed at about 0.05 nJ per pulse.

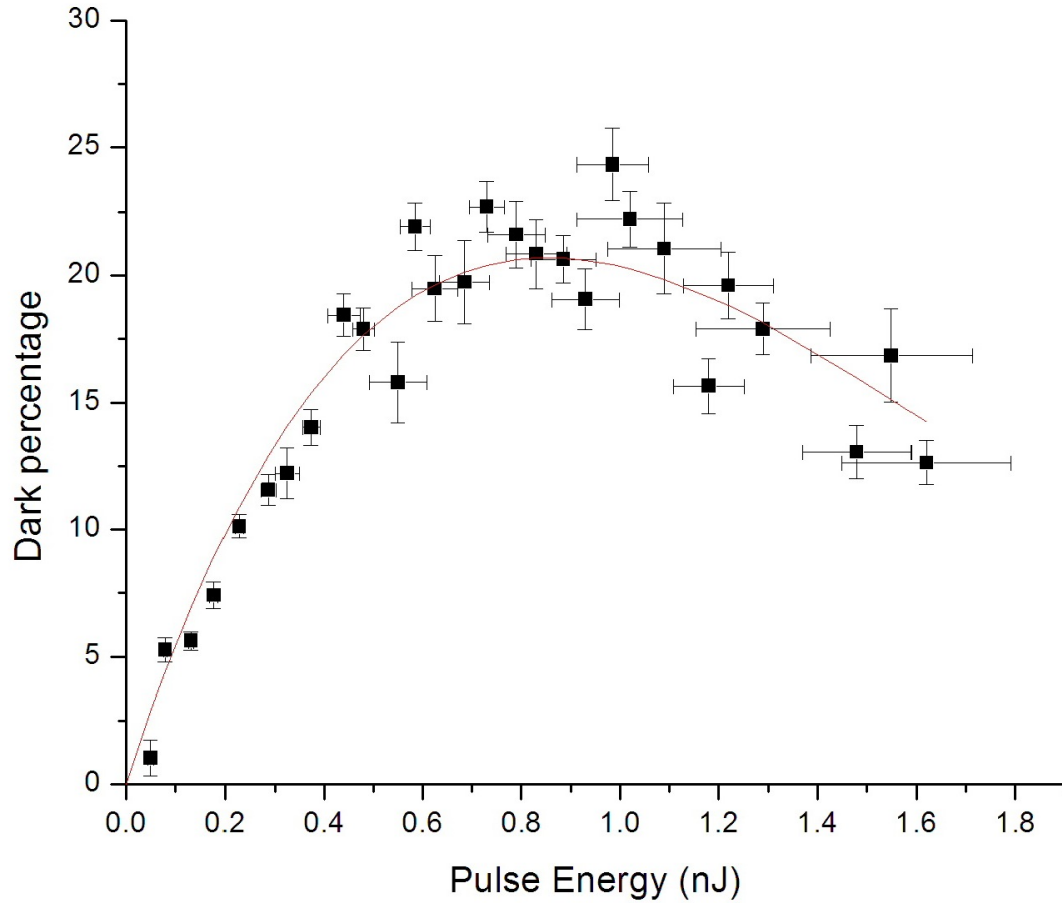


Figure 3.4: Data obtained from single 455 nm laser pulse excitation of the $6S_{1/2} \rightarrow 6P_{3/2}$ transition. The vertical axis is the fraction of times the ion was not fluorescing following the incident pulse, meaning that it was in the $5D_{5/2}$ state. Vertical error bars are statistical, given by the binomial variation in dark probability. Horizontal error bars are due to the variation in pulse energy which arise both from a slight non-constant intensity envelope of the pulses from the laser and from the finite rise time of the pulse picking AOM. The solid line is a two parameter fit to the function $P_{dark} = B \sin^2(\alpha\sqrt{U}/2)$.

The resulting data were binned and fit to the function $P_{dark} = B \sin^2(\alpha\sqrt{U}/2)$, where B is the branching ratio for the fraction of the time that the ion decays to the dark $5D_{5/2}$ rather than back into the cooling cycle and α simply corresponds to the shelving efficiency. So besides simply being a demonstration of the ability to excite the ion from the ground state to the excited P state with unit probability at a particular pulse energy given by the location of the maximum in Fig 3.4, this experiment when combined with a second experiment described in the following section provides a means to measure the branching ratios from $6P_{3/2}$ state and hence, the transition amplitudes and radial matrix elements. The branching fraction for the $6P_{3/2} \rightarrow 5D_{5/2}$ decay was found to be 0.215 ± 0.0047 and α equal to $3.41 \pm 0.07 \text{ nJ}^{-1/2}$. The value of B moreover was robust against fluctuations in α up to the observed 10%. It also proved not to change due to the small pulses on either side of the main selected pulse. This concern was laid to rest through numerical integration of the Bloch equations (see section and Fig. 3.2); the side pulses simply contribute to a non-zero dark probability at a pulse energy corresponding to a 2π rotation but do not have any effect on the maximum value of the curve which is simply given by the branching ratio.

3.5 Branching ratios from $6P_{3/2}$

A second experiment was needed to determine the absolute values of all three branching ratios, since the Rabi flop determined the fraction that decayed to the $5D_{5/2}$ state, leaving the two decay channels to $6S_{1/2}$ and $5D_{3/2}$ indistinguishable. This was done by weakly exciting the ion to the $6P_{3/2}$ state using trains of highly attenuated pulses at 455 nm of various lengths from 0.1 to 10 ms and 1.6 to 3.4 mW of average power. This relaxed the requirement that single pulses be selected from the Mira. This left decays to the D state indistinguishable, since only in the asymptotic limit could it be that ion was excited to the $6P_{3/2}$ state with high probability. The functional form of the dark probability expected vs. exposure time

can be calculated from the probability of excitation for a single pulse, given by the already frequently used equation $P_{exc} = \sin^2(\alpha\sqrt{U}/2)$ which can be expanded for low energy and hence small argument of the sine to be $P_{exc} \approx \alpha\sqrt{U}$. If the excited state has a probability B for decay to a dark state and $1 - B$ to a bright state, the rate of pumping into the dark state is given by $B\alpha\sqrt{E}f_{REP}$, where f_{REP} is the repetition rate of the laser. A steady-state dark population $P_{dark} = B\alpha\sqrt{E} \sum_{n=0}^{\infty} e^{-n\gamma/f_{REP}} = B\alpha\sqrt{E} \frac{e^{-\gamma/f_{REP}}}{1 - e^{-\gamma/f_{REP}}}$ will accumulate due to the sum of decaying exponentials with a characteristic lifetime γ for decay from the excited

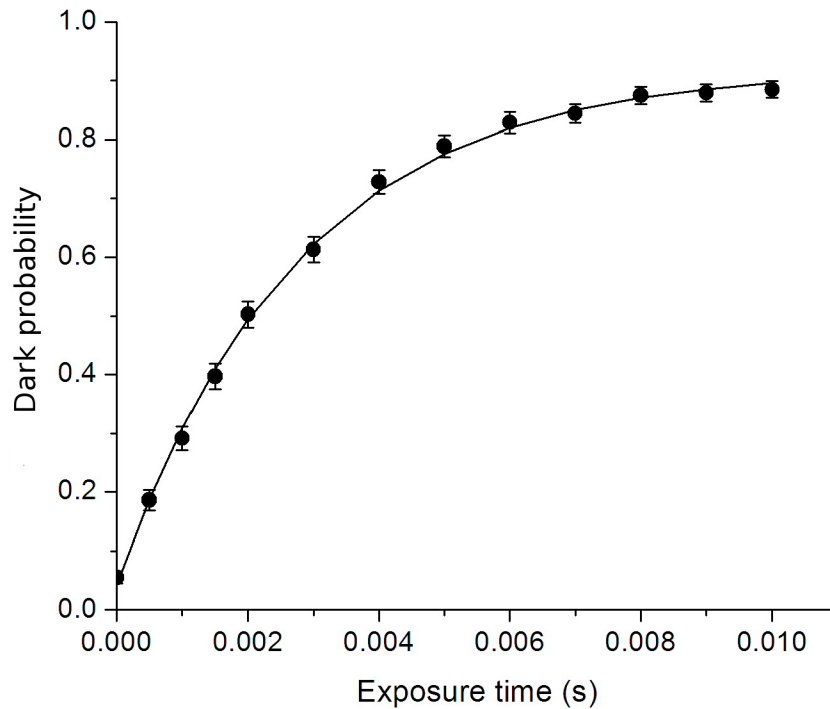


Figure 3.5: Characteristic data for the weak excitation experiment performed to determine a value for the branching ratio of D state decays. The experiment was repeated to establish a statistically robust value for the asymptotic dark state probability. The fit is to the expected form of the function discussed in the text $P_{dark} = \Delta + B(1 + e^{-\lambda t})$. Error bars include both the statistical uncertainty from binomial probability and a 0.5% systematic uncertainty arising mainly from de-excitation due to cooling light leakage and background gas collisions.

state in between pulses. The sum can be taken to infinity because the time between pulses and the lifetime for the atomic decay are both much shorter than the total exposure time. The rate of accumulation into the dark state population is then γP_{dark} . The total rate of pumping to the dark state, or shelving, is then the sum of P_{exc} and P_{dark} which can be integrated to give the population ρ_{dark} , and hence the probability of finding the ion dark after the train of pulses has passed. The functional form expected for the probability that the ion is dark, after all is said and done, is $P_{dark} = \Delta + B(1 + e^{-\lambda t})$, where Δ is any offset from zero probability at zero pulse duration due to false dark counts and λ is a parameter which depends on the pulse intensity, repetition rate and decay rate from the excited state. A representative data set for different exposure times is shown in Fig. 3.5.

The results of the weak excitation experiment are a ratio for each of the D state decays to each other, excluding decays to the S state, determined from the asymptotic dark state probability related to the B coefficient. The relative strengths are 0.881 and 0.119 for $5D_{5/2}$ and $5D_{3/2}$, respectively. Combining these ratios with the absolute value for the $5D_{5/2}$ decay from the Rabi rotation experiment and the fact the total ratio must equal unity, the absolute values for the branching ratios to $6S_{1/2}$, $5D_{3/2}$ and $5D_{5/2}$ are 79.6, 2.9 and 21.5% respectively. From the three branching ratios, summarized again with uncertainties in Table 3.1, transition rates and the dipole matrix elements can be calculated for the three transitions. The branching ratios are simply algebraic ratios of the three absolute transition amplitudes for the decays, with the constraint that the lifetime of the excited state τ_i is given by the inverse of the sums of all amplitudes for decays from that state, $\tau_i = \left(\sum_f A_{fi}\right)^{-1}$. From knowledge of the lifetime of the $6P_{3/2}$ state, given in [84] to be 6.32(10) ns, the transition amplitudes for the $6P_{3/2} \rightarrow 6S_{1/2}$, $\rightarrow 5D_{3/2}$ and $\rightarrow 5D_{5/2}$ are calculated and given in the final column of Table 3.1. From the transition strengths, the radial dipole matrix elements (Sect. 1.3) can be calculated

$$\langle 6P_{3/2} \parallel \hat{D}_{E1} \parallel f \rangle = \sqrt{\frac{g_i \lambda^3 A_{fi}}{2.0261 \times 10^{18}}} \quad (3.3)$$

where g_i is the degeneracy of the excited state (4 in the case of $6P_{3/2}$), λ is the transition wavelength and the numerical factor a conversion to atomic units where $ea_o = 1$ [49, 48]. The three matrix elements are then $\langle 6P_{3/2} \parallel \hat{D}_{E1} \parallel 6S_{1/2} \rangle = 4.720 \pm 0.040$, $\langle 6P_{3/2} \parallel \hat{D}_{E1} \parallel 5D_{3/2} \rangle = 1.349 \pm 0.036$ and $\langle 6P_{3/2} \parallel \hat{D}_{E1} \parallel 5D_{5/2} \rangle = 3.945 \pm 0.066$.

Table 3.1: Measured values for branching ratios from $6P_{3/2}$

Transition $6P_{3/2} \rightarrow$	Relative strength	Radial matrix element (a.u.)	Rate $A_{fi} \times 10^9 s^{-1}$
$6S_{1/2}$	0.756 ± 0.046	4.720 ± 0.040	0.1196 ± 0.0020
$5D_{3/2}$	0.029 ± 0.0015	1.349 ± 0.036	0.004589 ± 0.00025
$5D_{5/2}$	0.215 ± 0.0064	3.945 ± 0.066	0.03402 ± 0.00115

The main use for improved values of these matrix elements is in experimental confirmation of the values calculated and used in the calculation of the parity-nonconserving amplitude $A(E1)_{PNC}$ in the $6S_{1/2} \rightarrow 5D_{3/2}$ transition. The amplitude itself is given in second-order perturbation theory as a sum over intermediate state matrix elements of both the dipole (\hat{D}_{E1}) and parity-nonconserving weak charge (\hat{H}_{PNC}) Hamiltonians.

$$A(E1)_{PNC} = \sum_{n \neq 6S_{1/2}} \frac{\langle 5D_{3/2} \parallel \hat{D}_{E1} \parallel n \rangle \langle n \parallel \hat{H}_{PNC} \parallel 6S_{1/2} \rangle}{E_{6S_{1/2}} - E_n} + \sum_{n \neq 5D_{3/2}} \frac{\langle 6S_{1/2} \parallel \hat{D}_{E1} \parallel n \rangle \langle n \parallel \hat{H}_{PNC} \parallel 5D_{3/2} \rangle}{E_{5D_{3/2}} - E_n} \quad (3.4)$$

[91]

The largest contributions come from terms involving the $6P_{1/2}$ and $6P_{3/2}$ states and make up 90 and 8 % of the overall amplitude. Two of the radial matrix elements, $\langle 6P_{3/2} \parallel \hat{D}_{E1} \parallel 5D_{3/2} \rangle$

and $\langle 6P_{3/2} || \hat{D}_{E1} || 6S_{1/2} \rangle$, appear in this amplitude. Comparison between anomalous quasar spectra and Earth-based optical frequency standards to search for drifts in fundamental constants is another realm in which these values turn up. A summary of these results compared to other measurements and calculations is given in Fig. 3.6 with appropriate error bars.

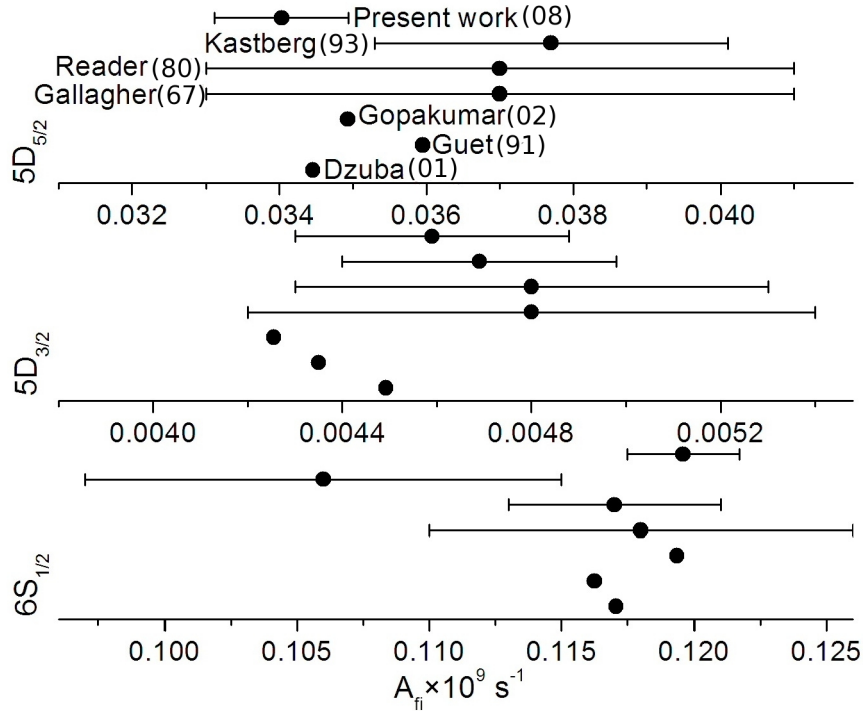


Figure 3.6: Comparison of the errors established for the transition rates for the three decays from the $6P_{3/2}$ state among different experiments [54, 88, 43] and the calculated values [48, 49, 34].

A brief discussion of the systematic errors that occur in the course of the two experiments is appropriate since several will come up in later chapters as well. An unavoidable effect is the de-excitation of the ion due to collisions with background gas particles. This has been thoroughly studied in the context of measurement of the $5D_{5/2}$ state lifetime [67], but over the 100 ms duration of each run of the experiment at a pressure of less than 2×10^{-11} torr here contributes to a systematically low value of the branching ratio to that state by

a value of order 0.1%. This will be a source of error in any experiment requiring shelving to that state, mainly in the readout of the quantum state of the ion during single qubit operations discussed in subsequent chapters. A second, more insidious source of error is the leakage of cooling and repumping light through the AOM's when they are turned off during the experiment. The AOM's provide an attenuation of greater than 40 dB and in these experiments, a fiber switch in between the cooling lasers and the trap contributed an extra 45 dB of attenuation. The saturation intensity for the cooling transition, however, is so low that any leakage light can drive transitions and take the ion out of the ground state contributing to a systematically low value for the dark state probability by less than 0.5%. The optical switch cannot always be used to increase the optical attenuation of leakage light into the fiber, so the effect must simply be mitigated by careful optical alignment and often by translating the AOM to avoid invisible inclusions that exacerbate the scatter.

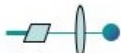


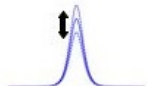


	Effect	Error (1)	Error(2)
	Cooling Leakage	0.5%	0.5%
	Collisions	<0.1%	<0.1%
	Pulse selection	--	1%
	Shot-to-shot variation	--	-0.7%
	Residual pulses	--	negligeable
	Chirp	--	negligeable

Table 3.2: Systematic effects identified in the two experiments to measure the $6P_{3/2}$ branching ratios. The columns correspond to (1) the weak excitation experiment and (2) the single-pulse Rabi flop. Because of the single-pulse selection required for the latter but not the former, several effects are not considered in column (1). Mechanisms are discussed in the text.

Asynchronicity between the pulse picker gate and the actual optical pulse from the laser, likely resulting from too short of an overlap between the computer trigger pulse and the pulse train coming from the DS1040-A15 to trigger the AND gate, resulted in about a 1% systematic error in the branching ratio involved in the Rabi rotation experiment. Shot-to-shot variation in pulse energy, found to be of order 10% contributed to a systematically low value for the branching ratio by a factor of about -0.7%. This variation is larger than measured for the pulse train of the laser itself and likely arises from the finite rise time of the pulse picker AOM. Better synchronization through the use of the phase-locked loop capability of the pulse programmer will likely eliminate the first problem and alleviate the second when this method of excitation is used to drive pulsed Rabi oscillation for coherent coupling of photon modes with the ion's spin, following the methods used for $^{111}\text{Cd}^+$ [68] and $^{171}\text{Yb}^+$ [72]. Residual pulses on either side of the selected pulse which are of order 3% the peak intensity of the main peak were found through the simulation in Sec. 3.2 to have no effect on the maximum attainable shelving efficiency but only to add some residual dark state population at an energy corresponding to a 2π pulse which would otherwise have zero probability there. Additional effects related to the pulses, such a frequency chirp, do not have any effect.

3.6 Ultrafast excitation at 493 nm

Since the goal of exciting the ion with ultrafast pulses is not simply to measure quantities in Ba^+ , but rather to generate entangled ion-photon and ultimately ion-ion pairs, drive stimulated Raman transitions with the different frequency components in the pulse or to realize ultrafast quantum gates [44, 29], it is necessary to pursue a means by which to generate mode-locked pulses at 986 nm to frequency double to resonance with the $6\text{S}_{1/2} \rightarrow 6\text{P}_{1/2}$ rather than $6\text{P}_{3/2}$ transition. This was accomplished by adding a second pump laser counter-

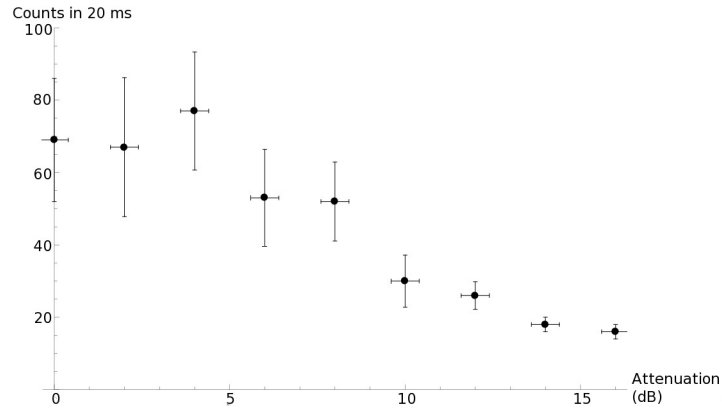


Figure 3.7: Ion fluorescence as a function of RF attenuation for illumination with 493 nm mode-locked pulses at a repetition rate of 8 MHz. Vertical error bars are the Poissonian variance in the counts for 20 trials per attenuation value. Dark counts were also recorded by turning off the red laser while the pulses were still incident on the trap and subtracted from the background. Horizontal error bars reflect the $\pm 5\%$ variation in pulse energy observed in the excitation at 455 nm, although this only reflects an upper bound.

propagating with the first and replacing the output coupler of the Ti:Sapphire laser with one more restrictive at the longer wavelength. The pulses were then sent onto the ion at a repetition rate decreased by a factor of ten with the 493 nm cooling laser turned off but the 650 nm repump laser left on. This is identical to the normal closed cooling cycle, albeit with the 650 nm laser providing the Doppler cooling and the pulsed laser at 493 nm serving as a repump, and ion fluorescence at 493 nm could be observed on the PMT. A plot of ion fluorescence as a function of attenuation on the VVA is given in Fig. 3.7. As attenuation decreases, more fluorescence is observed.

Generating ion-photon entangled pairs entails careful selection of states, polarization of excitation pulses and the direction from which they should be focussed onto the ion and the resulting photons be collected. Dipole radiation patterns plotted in Fig. 1.4(a) determine the probability of excitation given the angle of incidence. It would, for example, be impossible to drive π transitions along the magnetic field axis or to observe those decays. Selection rules can be used to the advantage of the experimenter as in the first ion-photon entanglement

scheme pictured in Fig. 3.8 where there is no mixing of $\Delta m_F = 0$ decays. This creates a unique entangled state $\psi_{ion-photon} = \frac{1}{\sqrt{2}} (|F = 2, m_F = 0; \nu_{red}\rangle + |F = 1, m_F = 0; \nu_{blue}\rangle)$ if all circularly polarized photons are filtered out. This is known as a photonic frequency qubit. A second scheme to illustrate the difficulty of generating entanglement in this way using the $6P_{3/2}$ state is shown in Fig. 3.7 on the right. Here a circularly polarized pulse excites the ion to the $M_J = +3/2$ state in the upper manifold which can no longer decay to the ground state except by emitting a circularly polarized photon. Since there is only one possible decay, there is no possible entanglement. Here instead an entangled ion-photon state exists on the 614 nm decay. If linearly polarized photons are filtered out, the state can be calculated using the formulae for transition strengths from Sec. 1.3, and is found to be $\psi_{ion-photon} = \left(\frac{10}{\sqrt{101}} |m_J = \frac{5}{2}; \sigma^-\rangle + \frac{1}{\sqrt{101}} |m_J = \frac{1}{2}; \sigma^+\rangle \right)$. This is known as a photonic polarization qubit, albeit a poor one due to the fact that one decay is ten times more likely than the other. This situation is also less than ideal because decays to this state are significantly less likely than those to the ground state, cutting down on the probability of generating the state in the first place, and the entangled state will decay in the characteristic lifetime of the $5D_{5/2}$ state. The desirable qualities of an ion-photon entanglement scheme are then

- 1) maximal entanglement (i. e. generation of one of the Bell states)
- 2) no extra decays that must be ignored
- 3) ion qubit states in the ground state
- 4) unwanted excitations excluded by selection rules

Despite the fact that hyperfine and optical qubits have been demonstrated in $^{137}\text{Ba}^+$, a third qubit that perfectly fulfills these criteria for the generation of entangled ion-photon pairs with ultrafast excitation is a qubit encoded in the Zeeman sublevels of the spinless $^{138}\text{Ba}^+$ isotope, as will be described in the final chapter.

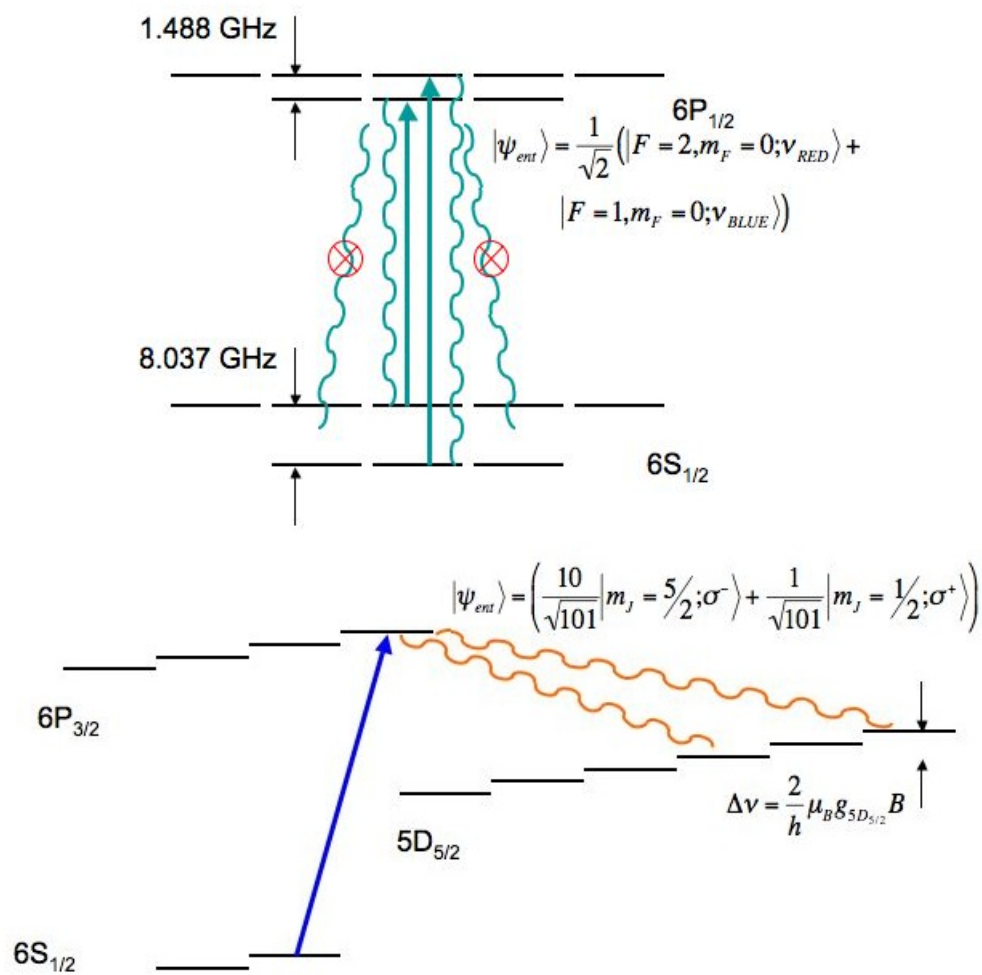


Figure 3.8: Two entanglement schemes, left a frequency qubit in $^{137}\text{Ba}^+$, right a polarization qubit in $^{138}\text{Ba}^+$. Individual Zeeman levels can no longer be ignored, as they were in the energy level diagram Fig. 2.4, since transition strengths and selection rules given in Fig. 1.5 determine the entangled states that can be created.

4 SINGLE PHOTON SOURCE

It is kind of fun to do the impossible.

- Walt Disney

Besides the requirements for the generation of ion-photon entangled pairs mentioned in the final section of the previous chapter, i. e. uniqueness of excitation and decay channels, maximal entanglement and a long-lived ionic qubit, another critical point in the problem is that each excitation produce no more than one photon. As previously mentioned, the goal of using mode-locked pulses to push excitation probability to unity is ultimately to use those photons as a means by which to carry information about the ion's spin state. In ion-photon entanglement schemes, if the ion produces two photons, the combined state will be mixed and useless. Likewise in ion-ion entanglement, where the photons are made to interfere on a non-polarizing beam splitter to remove which-way information to project the ions into a combined entangled state, if more than one photon per ion is emitted, the state will be mixed. Additionally, the photon collection and detection apparatus must be sufficiently sensitive to single photons if the protocol is to generate entangled pairs at a reasonable rate.

Both to verify the creation of single photons and ultimately to entangle the spin states of two ions, the optical setup for photon detection requires a slight change of elements before the PMT pair. In this case, we use a non-polarizing beam splitter so that the two photonic channels are identical. Only in the case that we want to perform a measurement of the photon polarization state, for instance to verify that emitted photons are in fact entangled

with the emitting ion, will a polarizing beam splitter be necessary. A 50-50 beam splitter will then remove which way information about the photons on the input ports and leads to a number of interesting features depending on how the photons are created. From the detection of single photons in the case that one input port is the vacuum, or pairs of photons when two ions are emitting into each input port, the details of the emission events can be determined.

4.1 Single photon interference on a beam splitter

If photons enter the left (L) and right (R) ports of a loss-less non-polarizing beam splitter with reflectivity R , there is an effective rotation of the photon number state $|n_L m_R\rangle \rightarrow e^{-i\theta \hat{J}_y} |n_L m_R\rangle$ as they exit the corresponding ports by an angle $\theta = \pi R$, with photon creation and annihilation operators \hat{a}_i^\dagger and \hat{a}_i contained in $\hat{J}_y = -\frac{i}{2} (\hat{a}_L^\dagger \hat{a}_R - \hat{a}_L \hat{a}_R^\dagger)$. The rotation matrices for $N = 1$ and $N = 2$ photons entering the beam splitter are

$$\begin{pmatrix} |0_L 1_R\rangle \\ |1_L 0_R\rangle \end{pmatrix} \rightarrow \begin{pmatrix} \cos\left(\frac{\pi R}{2}\right) & \sin\left(\frac{\pi R}{2}\right) \\ -\sin\left(\frac{\pi R}{2}\right) & \cos\left(\frac{\pi R}{2}\right) \end{pmatrix} \begin{pmatrix} |0_L 1_R\rangle \\ |1_L 0_R\rangle \end{pmatrix} \quad (4.1)$$

$$\begin{pmatrix} |0_L 2_R\rangle \\ |1_L 1_R\rangle \\ |2_L 0_R\rangle \end{pmatrix} \rightarrow \begin{pmatrix} \frac{1}{2}(1 + \cos(\pi R)) & \frac{1}{\sqrt{2}}\sin(\pi R) & \frac{1}{2}(1 - \cos(\pi R)) \\ -\frac{1}{\sqrt{2}}\sin(\pi R) & \cos(\pi R) & \frac{1}{\sqrt{2}}\sin(\pi R) \\ \frac{1}{2}(1 - \cos(\pi R)) & -\frac{1}{\sqrt{2}}\sin(\pi R) & \frac{1}{2}(1 + \cos(\pi R)) \end{pmatrix} \begin{pmatrix} |0_L 2_R\rangle \\ |1_L 1_R\rangle \\ |2_L 0_R\rangle \end{pmatrix} \quad (4.2)$$

[36]

An example for a 50-50 beam splitter, which will be the only type considered from here on, is shown in Fig. 4.1.

These matrices can be used along with knowledge of the input state to determine the

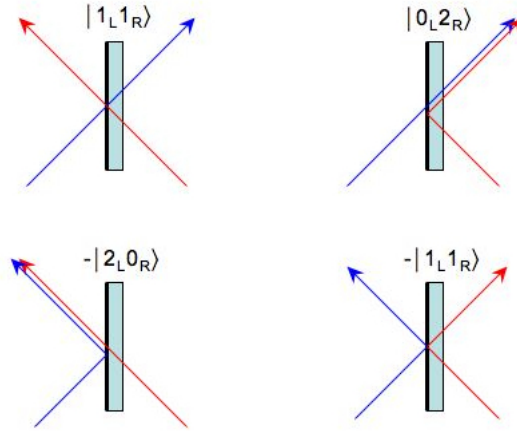


Figure 4.1: The four output states from a 50-50 non-polarizing beamsplitter obtained using Eq. 4.2 with the input state $|1_L 1_R\rangle$.

form of the photon distributions measured on the output ports of the beamsplitter. If the photons are created in a spatial-temporal mode $\xi(\vec{r}, t)$ at input port i (an index indicating either L or R) by decays from an excited state with lifetime τ by a series of N laser pulses with a repetition time t_{rep} between them, the electric field operator is given by

$$\hat{E}_i^+(t) = \sum_{n=1}^N \frac{A}{\sqrt{\tau}} \xi(\vec{r}, t) e^{-\frac{1}{2}(t-nt_{rep})/\tau} \Theta(t - nt_{rep}) \hat{a}_i^{(n)} \quad (4.3)$$

The factors A and $1/\sqrt{\tau}$ serve to account for the amplitude to detect photons and to normalize the photon detection probability to a unitless quantity. $\Theta(t - nt_{rep})$ is a Heaviside unit step function representing the probability of photon creation at each repetition of the experiment. The number state of photons at port i is a product of the N repetitions of the experiment along with the implicit assumption that only one photon is created in a single repetition of the experiment and that the repetition time t_{rep} is sufficiently long that several lifetimes τ pass between each repetition so no population can be accumulated in the excited state. This is given by

$$|\psi_i\rangle = \left(\prod_{n=1}^N \hat{a}_i^{(n)\dagger} \right) |0\rangle \quad (4.4)$$

The probability to a detect a photon in output port i created in input port i (it doesn't matter whether one looks at L or R on the output, referring to Eq. 4.1 it is clear that the probabilities are equally likely with a 50-50 beam splitter), is simply the expectation value of the electric field

$$\begin{aligned} \langle \psi_i | \hat{E}_i^-(t) \hat{E}_i^+(t) | \psi_i \rangle &= \langle 0 | \left(\prod_{n=1}^N \hat{a}_i^{(n)} \right) \sum_{k=1}^N \frac{A^*}{\sqrt{\tau}} \xi^*(\vec{r}, t) e^{-\frac{1}{2}(t-kt_{rep})/\tau} \Theta(t-kt_{rep}) \hat{a}_i^{(k)\dagger} \\ &\times \sum_{m=1}^N \frac{A}{\sqrt{\tau}} \xi(\vec{r}, t) e^{-\frac{1}{2}(t-mt_{rep})/\tau} \Theta(t-mt_{rep}) \hat{a}_i^{(m)} \left(\prod_{n=1}^N \hat{a}_i^{(n)\dagger} \right) |0\rangle \\ &= \frac{|A|^2 |\xi(\vec{r}, t)|^2}{\tau} \sum_{k=0}^N \sum_{m=0}^N e^{-\frac{1}{2}(t-kt_{rep})/\tau} e^{-\frac{1}{2}(t-mt_{rep})/\tau} \Theta(t-mt_{rep}) \Theta(t-kt_{rep}) \\ &\times \langle 0 | \left(\prod_{n=0}^N \hat{a}_i^{(n)} \right) \hat{a}_i^{(k)\dagger} \hat{a}_i^{(m)} \left(\prod_{n=0}^N \hat{a}_i^{(n)} \right) |0\rangle \\ &= \frac{|A|^2 |\xi(\vec{r}, t)|^2}{\tau} \sum_{k=0}^N \sum_{m=0}^N e^{-\frac{1}{2}(t-kt_{rep})/\tau} e^{-\frac{1}{2}(t-mt_{rep})/\tau} \Theta(t-mt_{rep}) \Theta(t-kt_{rep}) \delta_{km} \\ &= \frac{|A|^2 |\xi(\vec{r}, t)|^2}{\tau} \sum_{k=0}^N e^{-\frac{1}{2}(t-kt_{rep})/\tau} \Theta(t-kt_{rep}) \end{aligned} \quad (4.5)$$

This is known as the first-order correlation function $g^{(1)}$ and in the case that $A = \xi(\vec{r}, t) = 1$ is simply a series of N decaying exponentials with a lifetime equal to that of the excited state τ evenly spaced by t_{rep} . This is not an especially interesting result and could have probably been obtained simply by inspection.

A much more relevant and interesting question to ask is what is the probability, given photons being created in input port i by laser pulses incident on an ion to jointly detect photons at output ports L at say time zero and R at some other time τ_d . This is known as

the second-order correlation function $g^{(2)}(\tau_d)$, and is given by an expectation value involving four photonic operators

$$\begin{aligned}
g^{(2)}(\tau_d) &= \int_{-\infty}^{\infty} \langle \psi_i | \hat{E}_L^-(t) \hat{E}_R^-(t + \tau_d) \hat{E}_R^+(t + \tau_d) \hat{E}_L^+(t) | \psi_i \rangle dt \\
&= \int_{-\infty}^{\infty} \langle 0 | \left(\prod_{m=1}^N \hat{a}_i^{(m)} \right) \left(\sum_{k=1}^N \frac{A^*}{\sqrt{\tau}} \xi^*(\vec{r}, t) e^{-\frac{1}{2}(t - kt_{rep})/\tau} \Theta(t - kt_{rep}) \hat{a}_L^{(k)\dagger} \right) \\
&\quad \times \left(\sum_{n=1}^N \frac{A^*}{\sqrt{\tau}} \xi^*(\vec{r}, t + \tau_d) e^{-\frac{1}{2}(t + \tau_d - nt_{rep})/\tau} \Theta(t + \tau_d - nt_{rep}) \hat{a}_R^{(n)\dagger} \right) \\
&\quad \times \left(\sum_{n=1}^N \frac{A}{\sqrt{\tau}} \xi(\vec{r}, t + \tau_d) e^{-\frac{1}{2}(t + \tau_d - nt_{rep})/\tau} \Theta(t + \tau_d - nt_{rep}) \hat{a}_R^{(n)} \right) \\
&\quad \times \left(\sum_{k=1}^N \frac{A}{\sqrt{\tau}} \xi(\vec{r}, t) e^{-\frac{1}{2}(t - kt_{rep})/\tau} \Theta(t - kt_{rep}) \hat{a}_L^{(k)} \right) \left(\prod_{m=1}^N \hat{a}_i^{(m)} \right) |0\rangle dt \quad (4.6)
\end{aligned}$$

The \hat{a}_L and \hat{a}_R operators and their Hermitian conjugates can be expanded in terms of input port creation and annihilation operators \hat{a}_i^\dagger and \hat{a}_i using the rotation matrix, Eq. 4.1, and all terms involving the second input port can be eliminated since at the moment this is limited to an ion creating photons only at a single input port. This will leave the expression for $g^{(2)}(\tau_d)$ solely in terms of photonic operators for a single input port of the beam splitter. The k and m summations can be performed, leaving a delta function as before,

$$\begin{aligned}
g^{(2)}(\tau_d) &= \frac{|A|^4}{4\tau^2} \sum_{k=0}^N \sum_{n=0}^N (1 - \delta_{kn}) e^{-(\tau_d - t_{rep}(k+n))/\tau} \\
&\quad \times \int_{\tau_d + t_{rep}(k-n)}^{\infty} |\xi(u + nt_{rep})|^2 |\xi(u - \tau_d + nt_{rep})|^2 e^{-2u/\tau} \Theta(u) du
\end{aligned}$$

and the integration be carried out considering both the case where $\tau_d \leq -t_{rep}(k - n)$ and $\tau_d \geq -t_{rep}(k - n)$. The results can then be combined into a single expression

$$g^{(2)}(\tau_d) = \frac{1}{8\tau} \sum_{k=0}^N \sum_{n=0}^N (1 - \delta_{kn}) e^{-|\tau_d + t_{rep}(k-n)|/\tau} \quad (4.7)$$

where A and ξ have been set to unity for clarity [79, 61]. The former would simply shift the overall amplitude down and the latter, which is generally a decaying function representing a probability for photon emission, can usually be convolved with the lifetime of the excited state τ to change the effective lifetime of the overall decaying exponential. The functional form of $g^{(2)}(\tau_d)$ then is a series of N exponential decays extending to both position and negative delay time which decay in both directions (see Fig. 4.2). The delta function is an important feature of this function; it serves to suppress the peak centered at $\tau_d = 0$ and is a key feature of the emission of a single photon. By simply changing the input state to $|\psi_i\rangle = \left(\prod_n \hat{a}_L^{(n)\dagger}\right) \left(\prod_m \hat{a}_R^{(m)\dagger}\right) |0\rangle$, interference from both input ports can be analyzed, which will be important in remote ion entanglement. Surprisingly, the functional result is the same as Eq. 4.7, multiplied by a factor of four.

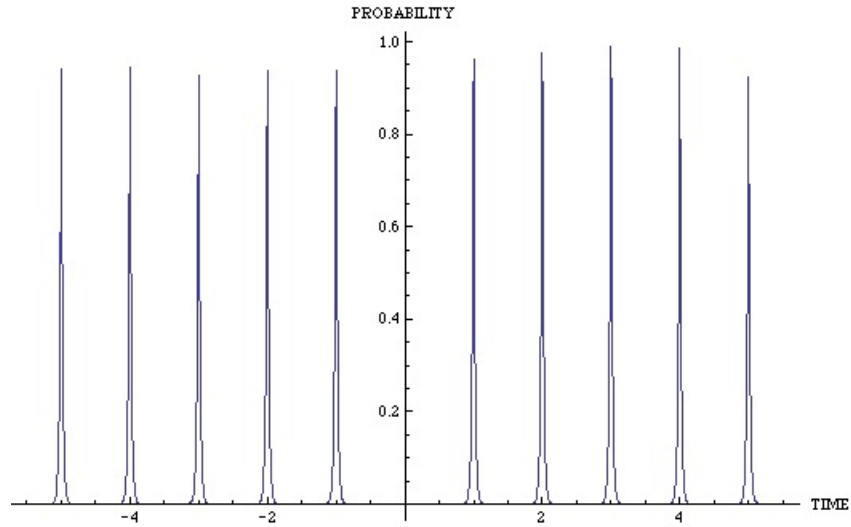


Figure 4.2: Correlation function $g^{(2)}(\tau_d)$ with horizontal axis in units of the repetition time of the experiment and the vertical the probability of photon detection on one PMT conditioned upon detection of a photon on the other PMT.

4.2 Experimental verification of single photon generation

While mode-locked pulses with duration much less than the lifetime of the state to which the ion is excited are generally thought of as the ideal means by which to generate single photons from spontaneous decay, CW laser pulses can be used as well. Here the excitation is weak to minimize the probability that two photons are generated from multiple excitations. This was also proposed as a means to generate ion-ion entanglement by simultaneous weak excitation of a pair of ion[15]. However, the photons' wavepackets are extended in time due to the low probability of excitation (encapsulated in the function $\xi(\vec{r}, t)$), making this scheme impractical due to the difficulty of synchronizing the timing of the arrivals of the photons at the beam splitter. It is a perfectly acceptable means by which to demonstrate the ability to create and detect single photons on command, however, and the happy coincidence of having a borrowed time-to-digital converter (TDC) at the same time as characterizing the performance of a new trap provided the opportunity to do just that.

The collection optics were modified as mentioned earlier in this chapter; a 50-50 non-

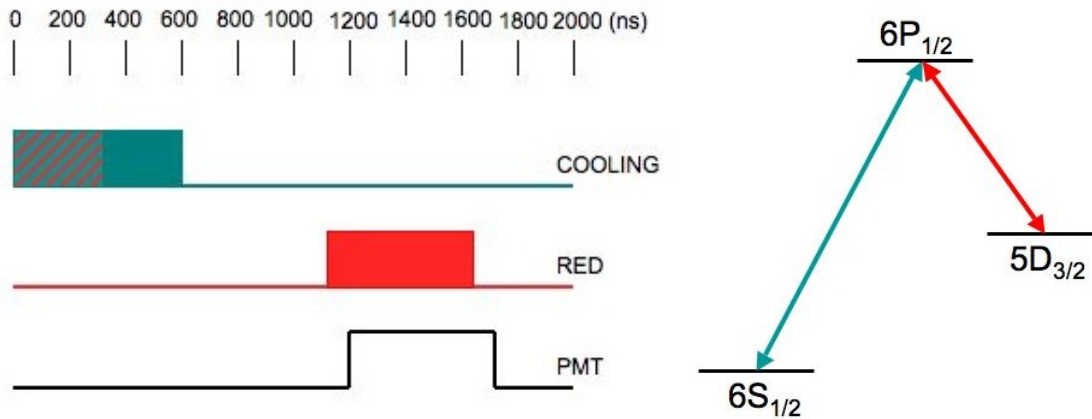


Figure 4.3: *left* Pulse sequence used to generate single 493 nm photons by pumping to $5D_{3/2}$ state with 493 nm light and generating the single photon by re-excitation to $6P_{1/2}$ with 650 nm light. *right* Partial Ba⁺ level diagram showing the levels involved in single photon creation.

polarizing beam splitter was placed after the 493 nm interference filter and a PMT placed at each output port. While single photons can be created on any spontaneous decay, the decay to the $6S_{1/2}$ state at 493 nm was chosen because it has the largest branching ratio and ultimately a qubit in the ground state is desirable. Using CW pulses introduces a second complication due to increased background counts. Since the duration of mode-locked pulses is extremely short (1 ps at most), the probability of collecting background photons in this interval is extremely low. The CW pulses in the measurement cycle used here required the PMT's to be gated and were still considerable. This window must be long enough to encompass several decay lifetimes of the $6P_{1/2} \rightarrow 6S_{1/2}$ transition but short enough to keep background counts to a minimum. The measurement sequence, shown in Fig. 4.3, was as follows - 300 ns of cooling at 493 and 650 nm, followed by 300 ns of the 493 nm light to ensure optical pumping to the $5D_{3/2}$ state, and 500 ns of delay before a 500 ns pulse of 650 nm light excited the ion to the $6P_{1/2}$ state to decay to the ground state and emit a single 493 nm photon. The PMT's were turned on 100 ns into this pulse and remained on 100 ns after it is switched off to accommodate signal delays. The cycle was repeated after another 400 ns delay. Data could be accumulated very quickly and indeed needed to be, since the probability of collecting and detecting each photon is quite low due to small collection angle, the interference filter which is only about 50% transmissive and the 12% quantum efficiency of the PMT's at 493 nm. Besides simply being a proof of the ability to create and detect single photons, this served as a means to characterize the photon collection efficiency of the optical setup [98].

Rather than simply counting the number of photon arrival events at each of the PMT's, which are limited in their ability to determine the arrival times of the individual photons by the 10 MHz onboard clock speed of the National Instruments PCIe 6530 card, a demo PicoQuant PicoHarp 300TM was used. This device takes inverted TTL signals from each of the PMT's simultaneously and continuously. Upon the arrival of a pulse from a photon at

either input, a timing sequence is initiated, binning photon arrival events on the other channel according to their time delay from the start pulse. The device has a resolution down to 4 ps, but was operated at 256 ps resolution for a reasonable match to the tens of nanoseconds lifetime of the spontaneous emission in this experiment. The data for approximately a night's worth of collection appear in Fig. 4.4 and have the characteristic form of Eq. 4.7, albeit noisy and with a constant offset from zero due to the previously mentioned background count problem.

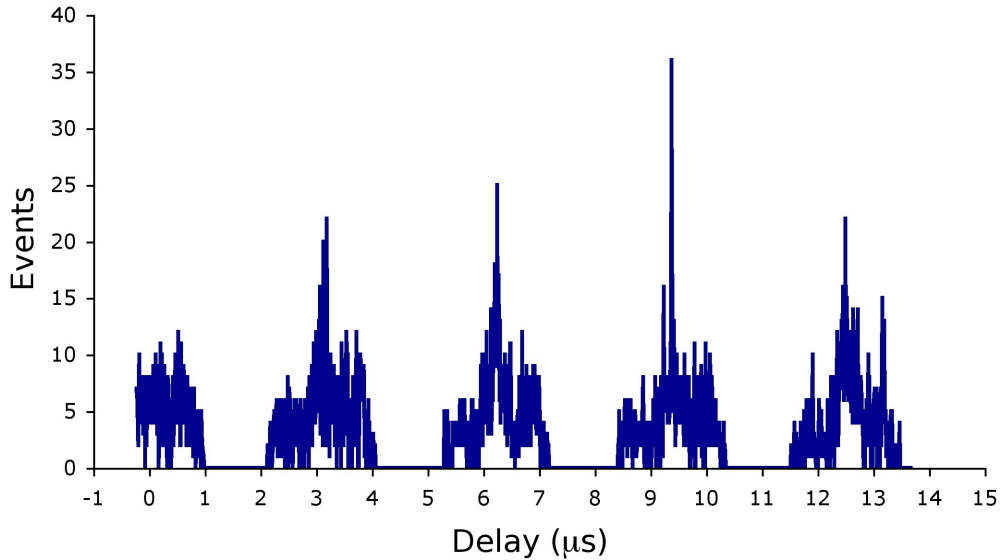


Figure 4.4: Data for the $g^{(2)}$ correlation function measured for CW pulses. The data recorded are the time intervals between the arrival of pairs of photons with a bin width of 256 ps, taken with a PicoQuant PicoHarp 300TM. Because of the background, the PMT's were only turned on in $2 \mu\text{s}$ windows along with the 493 nm cooling light. The lack of any counts over the background at zero delay indicates that what is being generated is in fact single photons in each pulse. The average width of each photon emission event is approximately 120 ns.

Each PMT window is accompanied by a significant level of background, but the feature to note is the lack of any peak above the background level at zero delay time. This is an indication, as Eq. 4.7 suggests, that only one photon is emitted during each pulse of the red laser. Also, each emission event has a characteristic width of approximately 120 ns, which is

significantly greater than the characteristic lifetime of the excited $6P_{1/2}$ state. This indicates that the emission is dominated by the excitation from the $5D_{3/2}$ state.

5 QUBIT INITIALIZATION & READOUT

Wenn man einen Teelöffel Jauche in ein Faß Wein gibt, ist das Resultat Jauche.

Wenn man einen Teelöffel Wein in ein Faß Jauche gibt, ist das Resultat ebenfalls Jauche.

-Schopenhauer

Two parts of the quantum computation problem have been only mentioned in passing thus far, qubit state initialization and readout of the final state. The former is accomplished by optical pumping, the latter by electron shelving. The $1.762 \mu\text{m}$ laser used for detection by means of transitions to the dark $5D_{5/2}$ state is very narrow (known to be better than 10 kHz, perhaps as good as 100 Hz), so whereas the broadband Ti:Sapphire laser could in principle cover the 8.037 GHz hyperfine splitting of the ground state of $^{137}\text{Ba}^+$, this laser will address individual magnetic sublevels of the fine or hyperfine levels of the ion. Optical pumping then provides the experimenter with a means by which to prepare the ion in one of these individual magnetic sublevels. Likewise, for ion-photon entanglement, transitions among these sublevels determine the photon qubit state that will be measured.

5.1 Magnetic field effects, briefly

It is well known that an externally applied magnetic field will break the Zeeman degeneracy of atomic states. The interaction is easily studied through perturbation theory using the interaction

$$\hat{H}_B = -\vec{\mu}_a \cdot \vec{B} = -g_J \mu_B \vec{J} \cdot \vec{B} \quad (5.1)$$

in which the atomic magnetic moment μ_a is proportional to the total angular momentum vector \vec{J} by the Bohr magneton μ_B and the Landé g -factor

$$g_J = \frac{J(J+1) + L(L+1) - S(S+1)}{2J(J+1)} + g_e \frac{J(J+1) - L(L+1) + S(S+1)}{2J(J+1)} \quad (5.2)$$

Here, g_e is the magnetic moment of the electron, whose slight deviation from 2 due to quantum electrodynamic corrections arguably sparked the entire field of atomic physics and J , L and S the total, orbital and electron spin quantum numbers, respectively. Similarly, the atomic g_J will deviate from the value predicted by Eq. 5.2, and a table of all measured Landé g_J factors for Ba^+ is given in Table 5.1.

Table 5.1: Electronic Landé g_J factors for all levels involving visible and infrared transitions from the ground state in Ba^+ . Deviations from what is expected from $L - S$ coupling (Eq. 5.2) in column 2 come from relativistic effects, interactions between the valence electron and the core shell and QED shifts from electron self-energy and vacuum polarization. Typical these arise at the $\alpha(\alpha Z)^2$ level.

State	Expected g_J	Measured g_J
6S _{1/2}	2	2.0024906(11) [56]
6P _{1/2}	2/3	0.672(6) [85]
6P _{3/2}	4/3	1.328(8) [85]
5D _{3/2}	5/4	0.7993278(3) [56]
5D _{5/2}	6/5	1.2020(5) [59]

The energy shift caused by the interaction between the spin and the magnetic field is given to first order for low values of the field where spin-orbit coupling is still the more dominant perturbation by

$$\begin{aligned}
\Delta E^{(1)} &= \left\langle n, J, M_J \left| g_J \mu_B \vec{J} \cdot \vec{B} \right| n, J, M_J \right\rangle \\
&= \left\langle n, J, M_J \left| g_J \mu_B B \hat{J}_z \right| n, J, M_J \right\rangle \\
&= g_J \mu_B B M_J
\end{aligned} \tag{5.3}$$

At higher values of the field J and M_J are no longer good quantum numbers and the L and S state vectors must be used. In general, second order perturbation theory gives a result at low field that is quadratic in magnetic field

$$\Delta E^{(2)} = \sum_{n', J', M'_J} \frac{\left| \left\langle n, J, M_J \left| g_J \mu_B B \hat{J}_z \right| n', J', M'_J \right\rangle \right|^2}{E_{n, J, M_J} - E_{n', J', M'_J}} \tag{5.4}$$

but it will be shown later in this chapter that the magnetic field applied to break the degeneracy of the magnetic sublevels of the ions for cooling is weak enough that the Zeeman energy shifts are very nearly linear.

The effect of this interaction is to split the fine structure energy levels in $^{138}\text{Ba}^+$ (or the hyperfine levels in $^{137}\text{Ba}^+$) into $(2J + 1)$ or $(2F + 1)$ sublevels. So just as for the sodium lines in which this effect was first observed, the barium ion will have multiple transitions at $1.762 \mu\text{m}$, all of which can be resolved spectroscopically since that transition is E2 and has a natural linewidth that will always be dominated by ion temperature, laser noise and residual magnetic noise. Fig. 5.1 shows transitions amongst the two Zeeman sublevels of the ground and the six sublevels of the $5D_{5/2}$ level and how they shift with the magnetic field away from what would be the zero field frequency of the $6S_{1/2} \rightarrow 5D_{5/2}$ transition between the two long horizontal dashed lines. The geometry of the excitation determines exactly which of these transitions will be observed in the spectrum of the ion illuminated by the $1.762 \mu\text{m}$ laser as its frequency is scanned over the Zeeman splitting of all the states (refer to the radiation

intensity patterns for quadrupole transitions, Fig. 1.4, and the discussion in Sec. 1.3 for selection rules for quadrupole transitions).

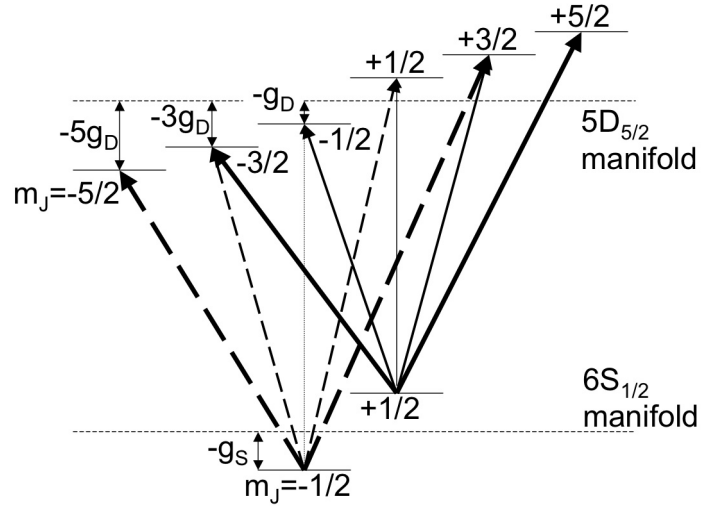


Figure 5.1: Relative shifts of the observed transitions between ground and excited state Zeeman levels in $^{138}\text{Ba}^+$, not to scale. Allowed transitions from the $m_J = +1/2$ and $m_J = -1/2$ Zeeman levels are represented by solid and dashed arrows, respectively, with the relative strengths indicated by the intensity of the line. In this work, $\Delta m_J = 0$ transitions are suppressed by the relative orientation of the \mathbf{k} -vector of the light to the quadrupole radiation pattern and were never observed. Frequency shifts are indicated in units of $\frac{1}{2\hbar}\mu_B B$ for Zeeman levels with negative spin. Those with corresponding positive spin shift upward by an equal amount.

Also important is the effect of an oscillating magnetic field, $\vec{B}(t) = \vec{B} \cos(\omega t)$. If the above treatment of the static magnetic field Zeeman effect looked shockingly similar to the DC Stark effect, then it is not surprising that the following will look like and lead to results almost identical in form to everything presented in Chapter 1. A rotating magnetic field affects a spin state $|JM_J\rangle$ by rotating it about the y axis

$$|\psi(t)\rangle = e^{-\frac{2i}{\hbar}\hat{J}_y\Omega t} |JM_J\rangle \quad (5.5)$$

which can be projected onto the quantization axis (aligned with whatever static field \vec{B}_o breaks the degeneracy of M_J levels so that it still makes sense to talk about transitions

amongst them) with the matrices

$$d_{M'_J M_J}^{(J)} = \langle JM'_J | \psi(t) \rangle \quad (5.6)$$

The selection rule that magnetic dipole interactions do not change J is implicit. The matrices

$d_{M'_J M_J}^{(J)}$ are given by the Wigner formula [92]

$$\begin{aligned} d_{M'_J M_J}^{(J)} &= \sum_k (-1)^{k-M_J+M'_J} \frac{\sqrt{(J+M_J)!(J-M_J)!(J+M'_J)!(J-M'_J)!}}{(J+M_J-k)!k!(J-M'_J-k)!(M'_J-M_J+k)!} \\ &\times \left(\sin \frac{\Omega t}{2} \right)^{2k-M_J+M'_J} \left(\cos \frac{\Omega t}{2} \right)^{2J-2k+M_J-M'_J} \end{aligned} \quad (5.7)$$

from which it is less than obvious that $\Delta M_J = \pm 1$ [95]. Fortunately, here we are only interested in a $J = 1/2$ system, specifically spin flips between the two Zeeman levels in the $6S_{1/2}$ state of $^{138}\text{Ba}^+$, so the matrix reduces to the familiar SO(3) rotation matrix

$$d_{M'_J M_J}^{(1/2)} = \begin{pmatrix} \cos \frac{\Omega t}{2} & -\sin \frac{\Omega t}{2} \\ \sin \frac{\Omega t}{2} & \cos \frac{\Omega t}{2} \end{pmatrix} \quad (5.8)$$

which leads to familiar ‘‘Rabi’’ oscillations between the $|\frac{1}{2}, \frac{1}{2}\rangle$ and $|\frac{1}{2}, -\frac{1}{2}\rangle$ Zeeman levels

$$\rho_e = \left| d_{\frac{1}{2}, -\frac{1}{2}}^{(1/2)} \right|^2 = \sin^2 \frac{\Omega t}{2} \quad (5.9)$$

The frequency of oscillations between the two levels comes from the Hamiltonian for a two-state spin system driven by a field \vec{B} perpendicular to the quantization axis oscillating at a frequency detuned from the RF spin flip resonance by a detuning δ

$$\hat{H}_B = \frac{\hbar}{2} \begin{pmatrix} 0 & g_J \mu_B B \\ g_J \mu_B B & \delta \end{pmatrix} \quad (5.10)$$

In the case that the RF frequency is resonant with the $M_J \rightarrow M'_J$ transition, the Rabi frequency is given by

$$\begin{aligned} \Omega &= \frac{1}{\hbar} \langle JM'_J | g_J \mu_B B \hat{J}_+ | JM_J \rangle \\ &= g_J \mu_B B \sqrt{(J - M_J)(J + M_J + 1)} \end{aligned} \quad (5.11)$$

which reduces simply to $\Omega = g_{6S_{1/2}} \mu_B B$ for the ground state of $^{138}\text{Ba}^+$ [94].

5.2 Optical pumping

The second of the DiVincenzo criteria [28] specifies that a quantum system must possess a means by which to initialize to a fiducial state in order to be useful as a qubit. Trapped ions are particularly good candidates in this regard because of a process known as optical pumping, whereby incident light of a particular polarization and orientation decouples from the cooling cycle a single state where the ion will become trapped after a series of several spontaneous decays. State preparation fidelity can be extremely robust and achieved in a time as short as a few microseconds.

Both $^{137}\text{Ba}^+$ and $^{138}\text{Ba}^+$ can be optically pumped. In the case of $^{137}\text{Ba}^+$, linearly polarized light is directed perpendicular to the magnetic field axis. Since the sidebands used to cool the two hyperfine levels of the ground state, $F = 1$ and $F = 2$, excite the ion to the $F' = 2$ manifold of the $6P_{1/2}$ state and any transition from $M_F = 0$ in the ground state to M'_F in the P state must change the F quantum number due to selection rules, the $F = 2; M_F = 0$

Zeeman level of the ground state becomes decoupled from the cooling cycle if the 493 nm light is linearly polarized parallel to the magnetic field axis. In $^{138}\text{Ba}^+$, circularly polarized light directed along the quantization axis will optically pump the ion to one of the M_J levels of the ground state depending on the left- or right-handedness of the circular polarization. The same can be used with a more complicated ground state (one with more than two levels) to optically pump to either the positive or negative extreme value of M_F , known as a stretched state. Linear and circular optical pumping schemes are shown in Fig. 5.2 (a) and (b), respectively.

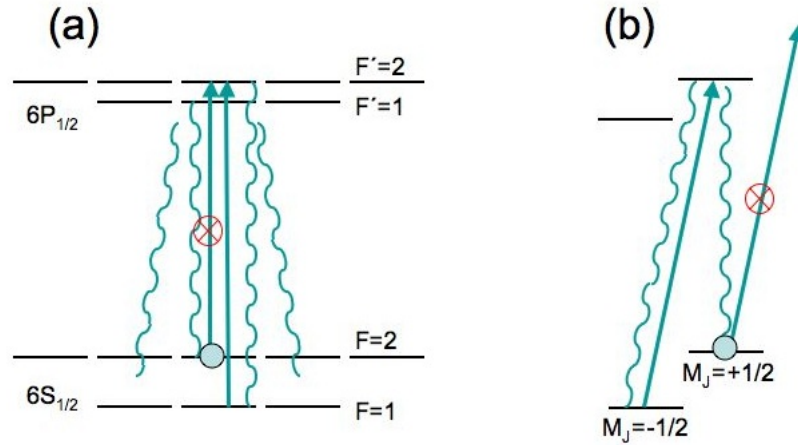


Figure 5.2: (a) Optical pumping to the $F = 2$, $M_F = 0$ state in $^{137}\text{Ba}^+$ with linearly polarized light perpendicular to the quantization axis. (b) Pumping to the $M_J = +1/2$ sublevel of the ground state in $^{138}\text{Ba}^+$ with circularly polarized light along the quantization axis.

The apparatus for optical pumping is a small pickoff of the 493 nm cooling light, focussed through a separate AOM than the cooling beam to allow independent switching. The light is fiber coupled and then sent through a Glan-Thompson linear polarizer with a 10,000:1 extinction ratio of the orthogonal polarization. The linearly polarized light is then either sent to the ion in the case of $^{137}\text{Ba}^+$ or sent through a quarter wave plate to produce circular polarization and then sent to the ion. Approximately 1-2 μW of optical pumping light is more than sufficient. The alignment procedure entails maximizing the fluorescence counts

from the ion with the optical pumping beam in an elliptical polarization, which will cool the ion just as before. By rotating the waveplate to a location which perfectly circularly polarizes the light, the ion fluorescence will be minimized since the ion can no longer scatter photons. Of course, the polarization is not perfect and can actually be quantified by a parameter $\sigma \equiv \frac{E_+ - E_-}{E_+ + E_-}$, where E_+ and E_- are the left and right circular components of the field. Optical pumping efficiency of approximately 90-95% has been observed, measured by using electron shelving of one of the Zeeman levels. During experiments, the ion is cooled with elliptically polarized 493 nm light and repumped with 650 nm light. The cooling light is shut off, but the repump remains on, as the ion still has a probability to decay to the $5D_{3/2}$ state during optical pumping. The circularly polarized optical pumping beam is then switched on for 100-200 μs and then after a short delay the red laser is switched off, leaving the ion prepared in one of the Zeeman levels.

Of course as mentioned before, the efficiency of circularly polarized optical pumping depends on the purity of the polarization σ , but also on the alignment of the beam with the magnetic field axis. The main field coil provides the magnetic field, but separate coils on the other two perpendicular axes carrying 100-200 mA serve to cancel stray fields at the trap center and better orient the magnetic field with the pumping beam. These currents are adjusted to maximize the shelving efficiency to one of the Zeeman levels. If θ is the angle between the magnetic field and beam's direction, the optical pumping efficiency is found to be

$$P\left(M_J = \frac{1}{2}\right) = \frac{1}{2} + \frac{2\sigma \cos \theta}{3 + 2\sigma^2 - \cos 2\theta} \quad (5.12)$$

[58]. This in principle leads to a two-parameter contour of optical pumping as a function of vertical and horizontal steering coil currents, with what is found to be a broad maximum. Since it is such a weak dependence and producing this contour is very time consuming,

in practice it has been found that simply minimizing PMT counts with a long exposure while exposing the ion to the optical pumping and red lasers serves as a sufficiently accurate method to align the field and optical pumping beam.

5.3 Shelving to $5D_{5/2}$ at $1.762 \mu\text{m}$

The last of the DiVincenzo criteria [28] to receive attention in this work (after the ability to couple to flying qubits, photons, initialize the qubits by optical pumping and perform operations with radiation resonant with the frequency splitting between $|0\rangle$ and $|1\rangle$ states) is the ability to read out the final qubit state. In this case, the task is accomplished by state-selectively “shelving” the qubit to the $5D_{5/2}$ state, taking it out of the cooling cycle so it no longer fluoresces, a state detection method pioneered by Dehmelt in the early days of ion trapping [76].

The laser used for this is a Koheras AdjustikTM thulium-doped fiber laser at $1.762 \mu\text{m}$ frequency stabilized via a Pound-Drever-Hall locking scheme to a high-finesse temperature-controlled ZerodurTM enclosed in vacuum. The frequency stability requirements for this laser are far more strict than for the ionization and cooling lasers, as it must be able to state-selectively excite the narrow quadrupole transition from the ground state to $5D_{5/2}$ and do so repeatably. The cavity itself has a free spectral range of about 0.5 GHz and a finesse of 1000, so a linewidth of 500 kHz. The laser frequency is offset from cavity lines by a double-pass AOM tunable from 80 to 120 MHz, frequency modulated at 1 MHz with an I/Q modulator to generate the error signal for the PDH lock servo, which itself is similar to the PDH servo for the cooling laser doubling cavity. Considerably more detail can be found in [25, 27]. The portion of the light not sent to the cavity is sent to a second single-pass AOM, where the first diffracted order is sent to the ion. This AOM has a bandwidth equal to that of the first and can be scanned to perform high-precision spectroscopy on the $6S_{1/2} \rightarrow 5D_{5/2}$ transition.

With the available laser intensity at the ion, a Rabi frequency of order approximately 100 kHz is achievable.

From measurements of the widths of transitions measured while performing spectroscopy on the $S \rightarrow D$ transition, typical widths of 50 kHz are observed. Optical Rabi oscillations taken on resonance display coherence times greater than 200 μs , indicating a laser linewidth of about 10 kHz. Because there are many other decoherence sources not related to the

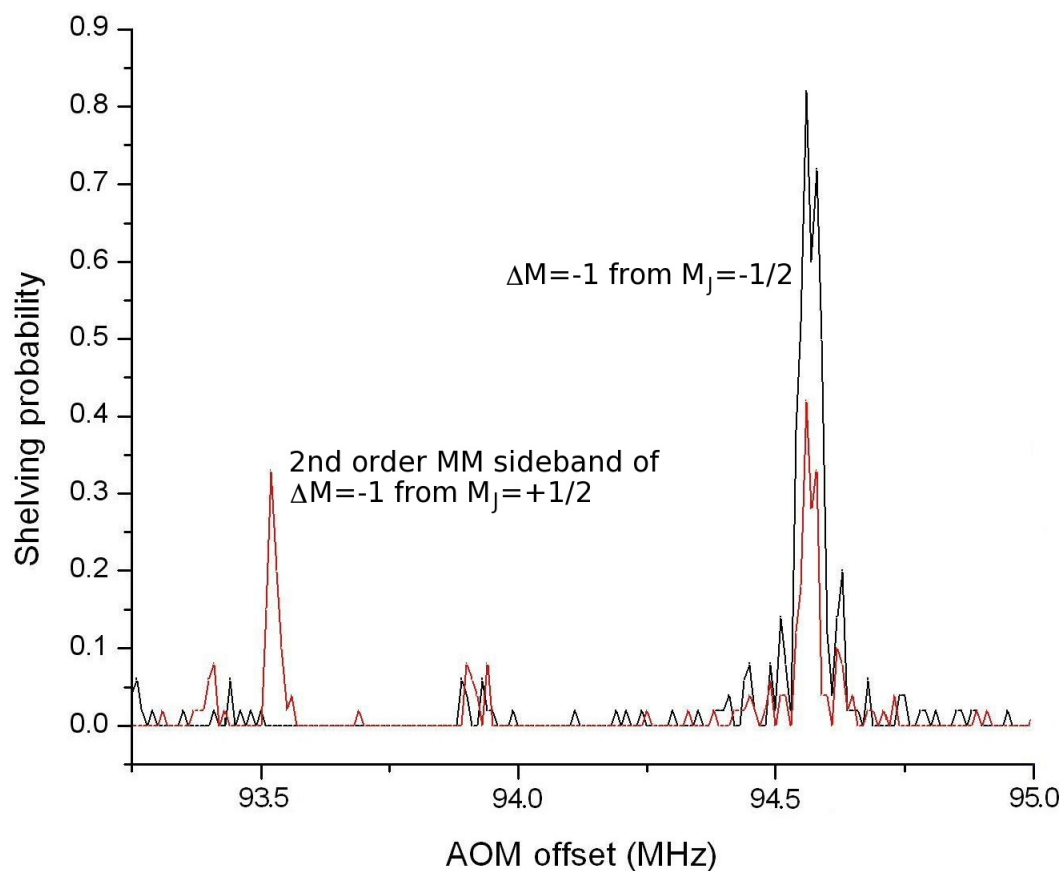


Figure 5.3: Scans of 1.762 μm laser single pass AOM frequency with (black) and without (red) optical pumping at main coil current of 3.0 A. Without optical pumping both M_J levels of the ground state are equally populated and as a result, the maximum value for the probability that the ion is dark after shelving one of the Zeeman levels is 50%. When optically pumped, the probability is enhanced for spin up and suppressed for spin down. This plot shows that the two transitions observed without optical pumping originate from opposite Zeeman levels of the ground state.

laser (fluctuating magnetic fields, ion temperature, etc.) this can be taken as an upper estimate of the linewidth of shelving laser, although there is some reason to suspect from adiabatic passage experiments, wherein the laser frequency is quickly swept over an atomic resonance rather than stabilized at the top of it for a fixed exposure, that the stability is considerably higher [78]. Long term stability, mostly dominated by thermal effects, is also quite good - observed to be less than 60 mK over the course of three months [27]. This is mostly dominated by the temperature coefficients of reference voltages and resistors in the temperature controller and could be improved upon by thermally insulating or even controlling the electronics, but the level of stability has been found to be sufficient.

Spectroscopy on the transitions amongst Zeeman levels from the ground state to the $5D_{5/2}$ state can then be performed similarly to the indirect shelving with the Ti:Sapphire laser through the $6P_{3/2}$ state. The ion is cooled with both the 493 and 650 nm lasers. The 493 nm cooling light is switched off to prevent power broadening of the ground state while driving the $6S_{1/2} \leftrightarrow 5D_{5/2}$ transition, which would otherwise wash out the fine features of the transition. Delaying turning off the 650 nm light pumps the ion to the ground state, during which time optical pumping light may or may not be applied to reach a definite Zeeman level of the ground state. The $1.762 \mu\text{m}$ light is then switched on for $20 \mu\text{s}$ to drive the $6S_{1/2} \rightarrow 5D_{5/2}$ transition. This pulse is triggered at a fixed value of the phase of the AC wall voltage to reduce fluctuation due to magnetic perturbations. The duration of the pulse is chosen to be approximately a π Rabi rotation between the ground and excited state for carrier transitions and lower order micromotion sidebands, while suppressing the excitation of weaker sideband transitions. After the pulse is applied, the cooling lasers are switched on and the ion's state is determined by observing its fluorescence on the PMT. The sequence is repeated 40 to 100 times for each value of the shift AOM to accumulate statistics. Shelving events (when the ion is in a dark state after the fiber laser pulse) are counted and the frequency of the laser shifted by the single-pass AOM to obtain the desired spectrum. A

section of the spectrum performed once with optical pumping and once without is shown in Fig. 5.3, from which it is obvious the effect that optical pumping has on the spectrum. The feature at approximately 94.5 MHz is a $\Delta M_J = +1$ transition from the $M_J = -1/2$ Zeeman level of the ground state, and the feature at 93.5 MHz is a sideband of the $\Delta M_J = -1$ transition from the opposite M_J level of the ground state. By optically pumping to the spin down level, the strength of the feature from that level increases from 50% to a maximum limited by the alignment of the magnetic field with the optical pumping beam axis, while the other feature is nearly extinguished because that Zeeman state is depopulated.

After locating individual Zeeman transitions through spectroscopy, optical Rabi oscillations can be executed by fixing the AOM frequency to be at the top of a resonance and varying the pulse length of the $1.762 \mu\text{m}$ exposure. A typical example can be seen in Fig. 5.4, taken on the $\Delta M = +1$ from $M_J = +1/2$ transition. In this way, transitions on micromotion sidebands can be differentiated from those on the carrier transitions. The micromotion sideband Rabi frequency is suppressed by a factor $|C_{\pm 2n}|$, which is of order one-third for our trap (refer to Section 2.3 on ion interactions with the trapping field) and hence micromotion transitions will always be separated by the Ω_{RF} and oscillate more slowly than carriers.

5.4 Precise measurement of $g_{5D_{5/2}}$

Just as Rabi oscillations with a Ti:Sapphire laser tuned to the $6S_{1/2} \rightarrow 6P_{3/2}$ transition provided a means by which to measure all three branching ratios and hence reduced matrix elements for decays from that state, narrow band excitation to the $5D_{5/2}$ state in a magnetic field provides an opportunity to precisely measure the Landé g_J factor for that state. Prior to the work presented here and in [59], this quantity was only known from archaic astronomical observations of line splittings and quoted as 1.12 [73, 5, 22, 74], which is a suspiciously large deviation from what is expected from $L - S$ coupling (i. e. $6/5=1.2$), much larger than any

of the other low-lying states in Ba^+ (Table 5.1).

The experimental procedure for producing the spectra needed to determine the g_J factor has been described in the previous section. Scanning the entire range of the single-pass AOM (80-120 MHz) encompasses either carriers or micromotion sidebands of four different Zeeman sublevel transitions. Starting at a magnetic field coil current of 3.0 Amps and progressively decreasing its strength reveals that the spectral resonances converge to several different values at zero current, where all transitions are degenerate up to separations equal

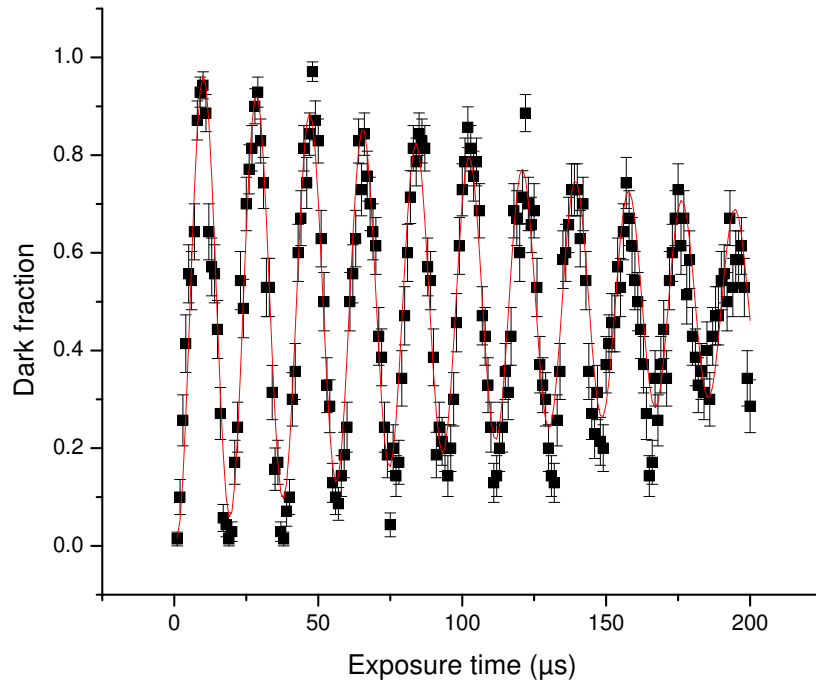


Figure 5.4: Optical Rabi oscillations were used to differentiate carrier transitions from their micromotion sidebands; this particular example was taken at 94.43 MHz at a coil current of 2.1 A on the $\Delta m = +1$ from $m_J = +1/2$ transition. As shown in Fig. 2.3, the strength of micromotion sidebands is suppressed and hence the Rabi frequency is lower compared to the carrier transitions. The red line is a fit to an exponentially decaying sine function, the decay arising from decoherence of the qubit states due to combination of magnetic noise, laser frequency noise and ion temperature.

to Ω_{RF} , the separation of micromotion sidebands from their respective carriers. Spectra were recorded at six different current values - 3.0, 2.6, 2.35, 2.1, 1.6 and 1.0 Amps. The data are presented in Fig. 5.5 along with lines tracing each of the transitions observed. By performing spectroscopy without optical pumping, all transitions are visible. Going back over the spectra with optical pumping reveals from which ground state Zeeman sublevel each line originates. Referring yet again to the geometry of the quadrupole radiation patterns shown in Fig. 1.4(b), it can be seen that there is a node in the intensity along the equatorial plane of the $\Delta M_J = 0$ plot. This is the direction from which the 1.762 μm light is directed into the trap chamber, so it is immediately apparent that only $\Delta M_J = \pm 1$ or ± 2 transitions are driven, the latter more strongly than the former.

Now the task remains to interpret the resulting spectra. The basic idea is to determine the expected relative positions of the different transitions in Fig. 5.1 as the magnetic field varies. Of the lines observed, two pairs are found to translate parallel to one another along the entire range of currents measured. Moreover, they are always separated by exactly the trap frequency Ω_{RF} , so they can immediately be identified as carrier transition/micromotion sideband pairs. The Rabi frequency of optical rotations between the ground and excited state on each line reveal that the stronger line is the carrier and the weaker the sideband. Carrier transitions have typical π rotation times of 10 μs , while sidebands require 20-30 μs . Two weaker transitions are found to converge to a zero current frequency 12.38 MHz above that of the first-order micromotion sidebands. This is consistent with them being second-order micromotion sidebands of two other transitions outside of the range accessible with the single-pass AOM. The error in bright vs. dark counts is taken to be binomial and each peak is fit to a three-parameter Lorentzian profile $P_{dark}(\omega) = \frac{1}{\pi} \frac{A}{(\omega - \omega_c)^2 + \gamma^2}$, where the parameter of interest is the central frequency of the transition ω_c . Typical statistical uncertainty in the fit of this parameter is of order several kHz. From the separations of seven measured pairs of carrier transitions/micromotion sideband pairs, the trap frequency can be determined to

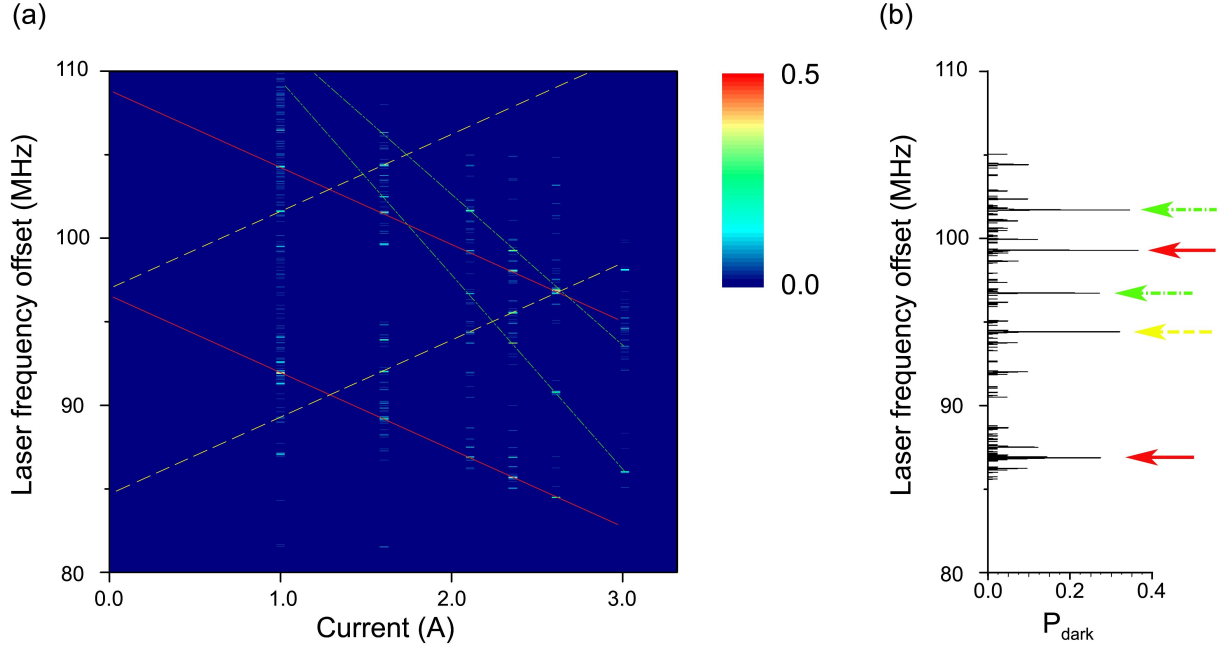


Figure 5.5: (a) All spectra measured without optical pumping showing $6S_{1/2} \leftrightarrow 5D_{5/2}$ transitions at six different values for the main coil current. The lines on the figure are inserted by hand to guide the eye. Resonances not crossed by the guiding lines were identified as secular sidebands by their characteristic frequency separation from main transitions. The dashed, yellow lines are the $\Delta M = +1$ from $M_J = +1/2$ and its 1st order micromotion sideband, the solid, red lines are the $\Delta M = -1$ from $M_J = -1/2$ and its 1st order micromotion sideband and dash-dot, green the 2nd order sidebands of $\Delta M = -2$ from $M_J = -1/2$ and $\Delta m = -1$ from $m_J = +1/2$. Secular motion sidebands at 2.5, 1.4 and 0.6 MHz are visible as well but deliberately not emphasized by added lines (b) A representative spectrum taken without optical pumping at 2.1 Amps. Arrow line styles (colors) correspond to the same scheme used to label transitions in (a).

be $\Omega_{RF} = 12.3759 \pm 0.0025$ MHz. By subtracting the measured trap frequency from first order micromotion sidebands and twice that frequency from second order sideband positions, we calculate the position of the carrier frequency for four Zeeman transitions: $\Delta M_J = +1$ from $|6S_{1/2}; M_J = +1/2\rangle$, $\Delta M_J = -1$ from $|6S_{1/2}; M_J = -1/2\rangle$, $\Delta M_J = -1$ from $|6S_{1/2}; M_J = +1/2\rangle$ and $\Delta M_J = -2$ from $|6S_{1/2}; M_J = -1/2\rangle$ (see Fig. 5.6).

From the extrapolated peak positions, one can take the zero field $6S_{1/2} \rightarrow 5D_{5/2}$ transition

frequency f_0 , the magnetic field at the center of the trap and the g_J factor of the $5D_{5/2}$ to be unknowns and formulate systems of linear equations in these three variables. As an example, for the 1.0 Amp data, there were three measured transitions, $\Delta M_J = +1$ from $M_J = +1/2$, $\Delta M_J = -1$ from $M_J = -1/2$ and $\Delta M_J = -1$ from $M_J = +1/2$. Their positions can be

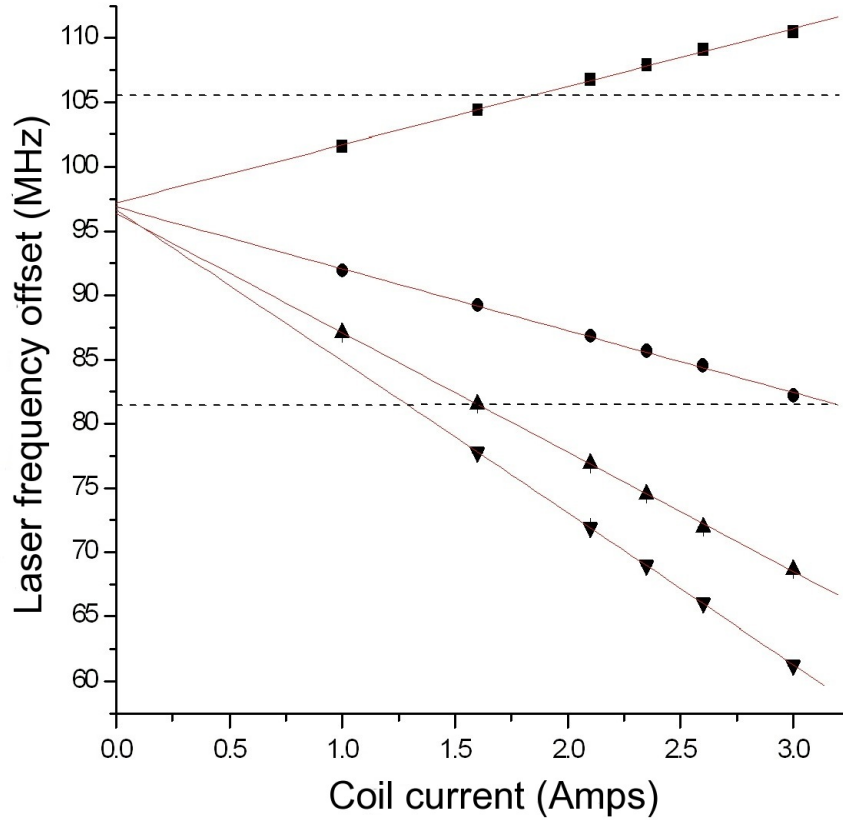


Figure 5.6: Measured and extrapolated positions of carrier transitions. Squares denote $\Delta M_J = +1$ from $M_J = +1/2$, circles $\Delta M_J = -1$ from $M_J = -1/2$, triangles $\Delta M_J = -1$ from $M_J = +1/2$ and upside-down triangles $\Delta M_J = -2$ from $M_J = -1/2$. Below 82 MHz and above 105 MHz (horizontal dashed lines in the figure), positions of carrier transitions were extrapolated from the position of micromotion sidebands due to insufficient bandwidth of the single-pass AOM to reach frequencies out of that range. The micromotion frequency itself was determined by the difference between measured carrier and first order sideband positions of the $\Delta m = -1$ from the $m_J = +1/2$ state. Fits are to the function $f(I) = \alpha\sqrt{I^2 + B_o^2} + f_o$, where I is the main coil current and B_o is a small offset magnetic field at zero coil current found to be less than 0.1% of the magnetic field from the main current coils and f_o is the transition frequency between $6S_{1/2}$ and $5D_{5/2}$ at zero field.

calculated from the standard formula for Zeeman shift (Eq. 5.3)

$$\begin{aligned}
 f_1 - f_0 &= \frac{\mu_B B}{2\hbar} (3g_D - g_S) \\
 f_2 - f_0 &= \frac{\mu_B B}{2\hbar} (-3g_D + g_S) \\
 f_3 - f_0 &= \frac{\mu_B B}{2\hbar} (-g_D - g_S)
 \end{aligned} \tag{5.13}$$

The variables f_0 and B can be eliminated by pairwise summing the equations and taking a ratio of the remaining two combined equations. This has the additional advantage that only frequency differences and no absolute frequencies are required, cutting down on the possible systematic errors which would otherwise be incorporated into the determination of the g factor. The final algebraic expression which must be solved is then

$$\frac{f_1 - f_2}{f_3 - f_2} = \frac{3g_D/g_S - 1}{g_D/g_S - 1} \tag{5.14}$$

For all other current values, there is an additional transition, $\Delta M_J = -2$ from $M_J = -1/2$, which actually overdetermines the system of equations adding $f_4 - f_0 = \frac{\mu_B B}{2\hbar} (-5g_D + g_S)$. Two values for the g factor ratio g_D/g_S can be found from the data and they are found to agree well within the statistical uncertainty. Using the measured value for g_S from Table 5.1, 2.0024906(11) [56], the absolute value for $g_{5D_{5/2}}$ can be found to be 1.2020 ± 0.0005 . The prediction from strict $L - S$ coupling is $6/5$, the difference arising from leading order QED shifts including electron self-energy and vacuum polarization, interactions between the valence electron and core shell as well as relativistic effects. The largest corrections occur at the $\alpha(\alpha Z)^2$ level, approximately where the deviation from $6/5$ is observed here [55, 46]. Going back to the system of linear equations used to calculate the g factor, the magnetic field at the center of the trap can be found to be 0.067 mT per Amp of current applied to

the main field coils, a value that will be useful when attempting to drive Rabi oscillations between the two M_J Zeeman levels of the ground state with the magnetic dipole component of incident RF radiation as described earlier in this chapter.

There are several sources of systematic error. There is no concern over linewidths or transition strengths, so only effects that influence the relative frequencies of transitions in an individual run need to be considered. Two sources of error related to trapping parameters are the variation of the ion's position with respect to the magnetic field and AC Zeeman shifts caused by currents induced in the trap by the high RF voltages. An estimate of the former is at the levels of 10^{-4} as the ion's position varies by much less than a few microns over the course of the experiment, as observed on a electron-multiplied CCD camera, and magnetic gradients are of the order $40 \text{ nT}/\mu\text{m}$. AC Zeeman shifts have been seen to affect g factor measurements, albeit at the 10^{-4} level in slightly different trap geometries [94], but these are highly suppressed in our trap design because of the large distance between the ion and the nearest grounded electrode through which current is able to pass to ground. Several potential sources of frequency error are related to the shelving laser itself. Drifts can occur both on the locking cavity due to pressure or temperature variations and in the phase of the 60 Hz AC voltage to which the beginning of the shelving pulse is triggered. This is only a problem during the course of a single run at each individual magnetic field, since the extraction of the g factor comes from each field value rather than a fit as a function of field. One can use the observed change in the position of the $6S_{1/2} \rightarrow 5D_{5/2}$ transition as a combined measure of these effects. The central (non Zeeman-shifted) value for the $6S_{1/2} \rightarrow 5D_{5/2}$ transition lies midway between the $\Delta M_J = +1$ from $|6S_{1/2}; M_J = -1/2\rangle$ and $\Delta M_J = -1$ from $|6S_{1/2}; M_J = +1/2\rangle$ transitions. This value agrees to within 4 kHz for the different values of coil current. From this uncertainty, a worst estimate of the shift over the course of an individual run, which is at most one hour in duration, is a few kHz. This represents the dominant contribution to the systematic uncertainty and the overall systematic error in the g factor

measurement can be assumed to be ± 0.0001 .

6 TOWARD A ZEEMAN QUBIT & OUT-LOOK

Schnee und Sturm und Felsgestein

Stählt den Fuß und übt das Bein.

Immer hinterm Offen sein,

macht das Leben arm und klein

-Gunnar Gunnarsson

I've had a good time. This just wasn't it.

-Graucho Marx

Up until now, there has been very little motivation for the experiments presented in the chapters leading up to here, seemingly violating the mantra, “say what you are going to say, say it and then review it.” This, however, was not done without purpose. Perhaps it was a bit of historical perspective on the work presented, since it more or less chronologically follows the progression of what was done. Along those same lines, perhaps the reason for only a vague sense of the exact methods and applications was to recreate some of the sentiment of the author, for whom the path to entanglement was not always so clear. Maybe it was to give the reader the opportunity to think about the utility of the methods presented here for him or herself. Whatever the reason, the intent in this final chapter is to wrap everything together into a single (incomplete) set of experiments aimed at realizing several goals in practical

quantum computation as well as a few foundational aspects of studying quantum mechanics. The two broad categories are less separate than the previous sentence might imply, but I hesitate to use the word “practical” with the foundations of quantum mechanics, as it may be difficult to impress upon, say the person sitting next to you on the bus, the burdensome importance of simultaneously closing all of the local loopholes in a Bell’s inequality test.

6.1 Zeeman qubit: How & why?

Referring to Fig. 3.8 one finds two ion-photon entanglement schemes - a frequency qubit at 493 nm in $^{137}\text{Ba}^+$ and a polarization qubit in $^{138}\text{Ba}^+$. As already noted in the text associated with the figure, neither of these qubit schemes represents a particularly good way in which to entangle ion spin with photon modes. A polarization qubit has the advantage of having straightforward qubit rotations by simply rotating a half-wave plate and not experiencing any chromatic dispersion through optics and optical fiber. A frequency qubit has the advantage that any optical process which disturbs polarization, such as reflections from curved surfaces and propagation through optical fiber will not mix the qubit states. This allows a greater collection angle than that for a polarization qubit, since the error rate due to mixing of polarizations from the two radiation patterns for dipole radiation (Fig. 1.4(a)) is proportional to the square of the solid angle subtended by the collection optics, $\propto (\Delta\Omega)^2$.

It has already been alluded to, but the ionic qubit of choice is one encoded in the Zeeman levels of the $6\text{S}_{1/2}$. While there are many advantages to using $^{137}\text{Ba}^+$ and exploiting its hyperfine levels to make magnetically insensitive qubit levels, the nuclear spin of $3/2$ creates very complex state manifolds even in the ground state. Operating a Ti:Sapphire on resonance with the $6\text{S}_{1/2} \rightarrow 6\text{P}_{1/2}$ transition at 493 nm offers some hope of generating ion-photon entanglement looking only at $\Delta M_F = 0$ transitions using the selection rule that such decays must change the F quantum number, but this ignores all decay channels for which $\Delta M_F =$

± 1 , or two-thirds of the total decays. Any decay from one of the stretched states (the only other states to which the ion can be initialized via optical pumping where one could envision generating a polarization qubit on decay) will generate at least one unwanted decay. Looking to the $6P_{3/2}$ state is even more hopeless, since there are four F levels all of which fall into the bandwidth of the 400 fs pulses from the Ti:Sapphire laser. It is therefore desirable to work instead with a spin- $\frac{1}{2}$ system, $^{138}\text{Ba}^+$.

A possible objection to this proposal is that there are no magnetically insensitive levels in $^{138}\text{Ba}^+$, so decoherence of the ionic qubit due to magnetic noise will render this ion-photon entanglement generation scheme useless. Such a qubit scheme has been implemented with $^{88}\text{Sr}^+$ ions [23]. Moreover, looking at the several hundred microsecond coherence time of optical Rabi oscillations gives some idea of an upper limit of how fast the qubit states decohere due to magnetic noise. Since the photon travel time is a negligible fraction of this time, there will be no degradation of the fidelity during the time operation are performed on the photonic qubit. While applying 8 Ghz radiation to $^{137}\text{Ba}^+$ must be performed with a microwave horn mounted outside the trap chamber such that no focussing of the radiation is possible, the tens of MHz RF radiation needed to drive qubit rotations can be applied directly to the trap electrodes, potentially making qubit rotations very fast. Even greater speed and improved insensitivity to magnetic fluctuations would be possible if qubit operations were performed with a pair of Raman beams. Moreover, line-triggering of experimental sequences, magnetic shielding and perhaps active field compensation can be employed to further extend the coherence time which has already been observed. Detection with adiabatic passage by sweeping the $1.762 \mu\text{m}$ laser over the desired qubit level rather than fixing the frequency of the laser at the atomic resonance has improved fidelity of detection even with a slightly varying magnetic field.

The greatest advantage of the proposed Zeeman qubit is its simplicity. Generation of ion-photon entangled states simply requires optically pumping with σ^+ polarized light

in a manner identical to that employed in the g factor measurement presented in the previous chapter. A single π polarized femtosecond pulse at 493 nm will excite the ion to the same Zeeman sublevel in the $6P_{1/2}$ pair of states. On decay the entangled state $\frac{1}{\sqrt{2}}(|M_J = +1/2; \pi\rangle + |M_J = -1/2; \sigma\rangle)$ will be created. Qubit states are separated by a splitting determined by the magnetic field, which has already been found to equal 0.067 mT/A or applied coil current or, using the measured $g_{6S_{1/2}} = 2.0024906$, 12.4 MHz/A. The small splitting and the fact that the transition is magnetic dipole means these states are extremely long-lived. Qubit rotations are performed applying RF modulation to the ground electrodes in the trap which are shorted on the side opposite the helical resonator. This has been described in Section 5.1 where it was assumed that the oscillating magnetic field was directed perpendicular to the quantization axis and had a ± 1 helicity component. Since the ion is at the center of where the driving field originates, the near-field form of the oscillating magnetic field will have all three “polarization” components to drive the magnetic transition.

The sequence of experiments leading to the demonstration of a Zeeman qubit is to first perform 1.762 μm spectroscopy as described in the previous chapter to locate a resonance from the optically pumped state to the $5D_{5/2}$ state for detection. Once such a resonance is located, RF spectroscopy must be performed to locate the resonance between the two Zeeman levels. RF radiation is synthesized by a Stanford Research Systems DS345 function generator at -20 dBm, amplified to +22 dBm and sent directly to the ground electrodes of the trap, accessed on the output end of the helical resonator. After optically pumping the ion to the bright qubit state, all lasers are shut off and a 50 μs pulse of RF radiation is applied to attempt to drive the ion into the opposite Zeeman level. This was found to heat the ion significantly, presumably because the frequency is very nearly twice the trap frequency. Since shelving efficiency depends strongly on ion temperature, performing state detection with a fixed duration, fixed frequency 1.762 μm pulse failed miserably. Instead, this was a perfect opportunity to employ the pulse sequencer described in section 2.4; shelving pulses were

replaced by frequency ramps over a fixed range at a rate chosen to adiabatically transfer ion population from the ground to the excited state. This is a much more robust shelving method, displaying significantly better insensitivity to ion temperature and magnetic fluctuations. Preliminary results of RF spectroscopy are shown in Fig. 6.1.

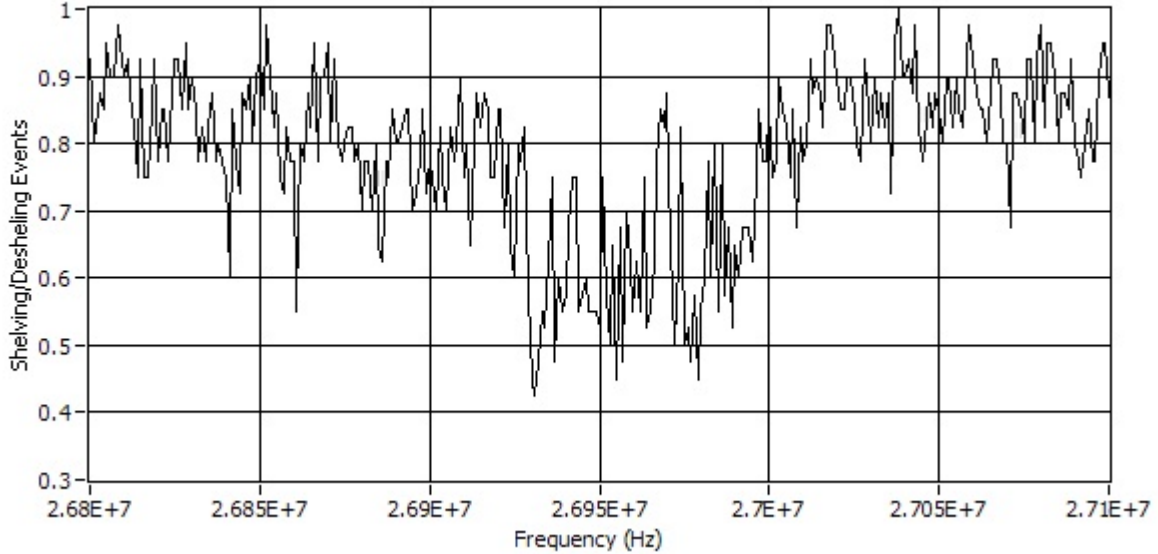


Figure 6.1: Preliminary results for driving RF Zeeman transitions between the $6S_{1/2}; M_J = \pm 1/2$ levels in $^{138}\text{Ba}^+$. The flat shelving level at 85% represents the maximum optical pumping/adiabatic passage shelving efficiency achieved. If the observed dip represented a π pulse, it would ostensibly reach approximately 15%. However, there is no reason to assume that the transition was not over- or under-driven, either of which would result in less than unit efficient population transfer.

6.2 From entangled ions and photons to entangled ions

The real utility of generating entangled ion-photon pairs is to transmit information about the quantum state of the ion over long distances to other ions. Several schemes have been proposed to accomplish this task [15, 99, 30]. The first such scheme involves weakly exciting the ion from the ground $|\downarrow\rangle$ state to a metastable excited state $|e\rangle$ with probability $\epsilon \ll 1$. The excited state has equal probability to decay to $|\downarrow\rangle$ or $|\uparrow\rangle$, and the detectors are

sensitive only to the latter. So after excitation of both ions, the state is $(|\downarrow\rangle_1 + \sqrt{\epsilon}|e\rangle_1) \otimes (|\downarrow\rangle_2 + \sqrt{\epsilon}|e\rangle_2)$. Conditioned on detection of a $|e\rangle \rightarrow |\uparrow\rangle$ photon, the ions will be projected into the state $\frac{1}{\sqrt{2}} (|\downarrow\rangle_1 |\uparrow\rangle_2 + e^{ik\Delta x} |\uparrow\rangle_1 |\downarrow\rangle_2)$ after a 50-50 beam splitter. This scheme suffers from the probability of multiple excitations and the fact that the relative phase caused by any optical path length difference Δx will ruin the entanglement fidelity. The second scheme requires the detection of coincident pairs of photons, so suffers from lower entanglement generation rate, but is much more robust. Experimentally the second scheme has been achieved with Ytterbium ions [72], but the emitted photons in that case are at a wavelength of 369 nm. This is UV and hence limits the distance over which the photons propagate in single-mode optical fiber to a few meters at most. As mentioned before, Ba^+ emits at 493 nm, so the emitted photons experience significantly less attenuation, enabling both a higher repetition rate for successful generation of entangled pairs of ions as well as longer distance between ions.

If a pair of $^{138}\text{Ba}^+$ ions is optically pumped to the spin up $M_J = +1/2$ Zeeman level of the $6S_{1/2}$ state, which will hereafter be denoted as $|\uparrow\rangle$, and excited with a linearly polarized pulse from a Ti:Sapphire laser to the spin up state in the $6P_{1/2}$ state, there are no mixings of levels on the excitation. Likewise on decay, each ion has two possible decay channels, each of which is equally likely, so the state of the two ions after several P state lifetimes (tens of ns) is

$$\begin{aligned}
|\Psi\rangle &= \frac{1}{2} (|\uparrow_1\rangle |\pi_1\rangle + |\downarrow_1\rangle |\sigma_1\rangle) \otimes (|\uparrow_2\rangle |\pi_2\rangle + |\downarrow_2\rangle |\sigma_2\rangle) \\
&= \frac{1}{4} [(|\uparrow_1\uparrow_2\rangle + |\downarrow_1\downarrow_2\rangle) \otimes (|V_1V_2\rangle + |H_1H_2\rangle) \\
&\quad + (|\uparrow_1\uparrow_2\rangle - |\downarrow_1\downarrow_2\rangle) \otimes (|V_1V_2\rangle - |H_1H_2\rangle) \\
&\quad + (|\uparrow_1\downarrow_2\rangle + |\downarrow_1\uparrow_2\rangle) \otimes (|V_1H_2\rangle + |H_1V_2\rangle)
\end{aligned}$$

$$+ (|\uparrow_1\downarrow_2\rangle - |\downarrow_1\uparrow_2\rangle) \otimes (|V_1H_2\rangle - |H_1V_2\rangle)] \quad (6.1)$$

where it has been identified that if the ion is observed perpendicular to the quantization axis that the π and σ decay modes are orthogonal and correspond to vertically and horizontally polarized photons, respectively. This isn't interesting yet, since the two ion-photon pairs are in a product state. If the two emitted photons are matched temporally and spatially on a 50-50 non-polarizing beam splitter as described in section 4.1 for the case of a single photon, the interference between the two amplitudes for both photons being transmitted or both being reflected can project the ions into an entangled state by removing which-way information from each individual photon as described in Chapter 4. Because of the antisymmetrization of the overall wavefunction [52], the two photons will emerge from different output ports of the beam splitter only if they are in the state $\frac{1}{\sqrt{2}} (|V_1H_2\rangle - |H_1V_2\rangle)$, immediately heralding the ion-ion state $\frac{1}{\sqrt{2}} (|\uparrow_1\downarrow_2\rangle - |\downarrow_1\uparrow_2\rangle)$. With polarizing beam splitters located in each of the output channels and four PMT's, it is possible to detect the photon state $\frac{1}{\sqrt{2}} (|V_1H_2\rangle + |H_1V_2\rangle)$ and generate the symmetric state $\frac{1}{\sqrt{2}} (|\uparrow_1\downarrow_2\rangle + |\downarrow_1\uparrow_2\rangle)$. Detecting two photons in the same output port corresponds to the $\frac{1}{\sqrt{2}} (|V_1V_2\rangle \pm |H_1H_2\rangle)$ states and does not generate a unique ion-ion entangled state [71].

This is a probabilistic process because only a very small percentage of the decays actually results in an entangled pair. There is effort to enclose each ion in an optical cavity to preferentially emit into a single spatial mode thereby making the process nearly deterministic [105, 7]. The probability for successful ion-photon entanglement generation is $P_{ion-ph} = P_{exc}BI_{\Delta\Omega} \left(\frac{\Delta\Omega}{4\pi} \right) T\eta$, where P_{exc} is the probability of excitation, B the branching ratio to the desired qubit states, $I_{\Delta\Omega}$ the intensity of the radiation into the solid angle of collection $\Delta\Omega$, T the loss due to transmission through optical fiber or from other optical elements such as interference filters and η the single-photon detection efficiency. Since two such single photon events are necessary for the generation of entangled ion pairs and only one of four Bell states

is detected from the post-selection process described above, the probability for success in that case is $P_{ion-ion} = \frac{1}{4}P_{ion-ph}^2$. The use of mode-locked pulses for excitation enables $P_{exc} \approx 1$ and using long wavelength transitions ensure that T and η are as high as possible. Additional sensitivity may be gained by using avalanche photodiodes (APD's) for detection rather than PMT's which would have a quantum efficiency closer to 80% rather than 10-20%. The greatest gains in efficiency come from improving the solid angle $\Delta\Omega$ from which photons are collected, which even with the best refractive optics available is typically only a few percent of the sphere [6] because of the distance between the ions and vacuum viewports. Several schemes using in-vacuum parabolic [69] and spherical mirrors with downstream aspherical correctors [97] have been investigated to boost fluorescence collection significantly. If ion state detection, the speed bottle-neck of the entire pulse sequence required, is conditioned on detection of a photon, the experiment can be run at a high repetition rate, perhaps a few kHz. Even still, an entanglement generation probability of a few times 10^{-8} is the current state of the art [72]. Construction of a partial Bell state analyzer (i. e. one that only generated the antisymmetric Bell state) has begun in our lab, using Toptica FiberDocksTM with identical triplet lenses as the outputs of two single-mode optical fibers, each directed onto a 50-50 beam splitter at as near normal incidence as possible. A half wave plate on a rotation mount in one arm of the interferometer can be rotated to change the measurement basis. The entire apparatus is enclosed in a light-tight box to keep error due to background counts at a minimum. Optical elements are mounted on remote-controllable Pico-motorTM mounts.

6.3 Applications

There are several applications of heralded entangled states of ions remotely separated by as great a distance as the ≤ 30 dB/km attenuation of 493 nm photons in optical fiber allows.

Since the Zeeman or hyperfine states involved have nearly infinite decay times, the entangled state can be pre-prepared for delayed measurement.

Entangled pairs of particles have long been used to test the famous Bell's inequality [8]. The generic *Gedankenexperiment*, recast in the more experimentally friendly CHSH form, proceeds as follows. At two different locations A and B , so labelled to reflect the identity of the experimenters Alice and Bob, two different measurements $A(a)$ or $A(a')$ and $B(b)$ or $B(b')$ can be performed. The combination of correlations C

$$S \equiv C[A(a), B(b)] + C[A(a), B(b')] + C[A(a'), B(b)] - C[A(a'), B(b')] \quad (6.2)$$

can be measured. In the case of classical systems, where the values of each measurement are uncorrelated and can take the values ± 1 , either $B(b) \pm B(b')$ will be zero and the other equal to two. So the average of many such experiments performed on the system will lead to $S \leq 2$, which is the Bell inequality. For a quantum mechanical system, if the measurements are the values of some non-commuting pair of operators such as two different components of a particle's spin along a different set of coordinate axes at each location A and B , the expectation value

$$\begin{aligned} S &= \left\langle \overbrace{-\hat{\sigma}_z}^{\text{particle 1}} \cdot \underbrace{\frac{1}{\sqrt{2}}(\hat{\sigma}_z + \hat{\sigma}_x)}_{\text{particle 2}} \right\rangle + \left\langle \hat{\sigma}_z \cdot \frac{1}{\sqrt{2}}(\hat{\sigma}_z - \hat{\sigma}_x) \right\rangle + \left\langle -\hat{\sigma}_z \cdot \frac{1}{\sqrt{2}}(\hat{\sigma}_x + \hat{\sigma}_x) \right\rangle - \left\langle \hat{\sigma}_x \cdot \frac{1}{\sqrt{2}}(\hat{\sigma}_z - \hat{\sigma}_x) \right\rangle \\ &= 2\sqrt{2} \end{aligned} \quad (6.3)$$

when the two particles are produced in a Bell state. This is clearly greater than two, violating Bell's inequality [18, 19].

An interesting application of remotely generated entangled ion pairs not related to quantum information processing is a Bell's inequality measurement that simultaneously closes

the detection and locality loopholes prognosticated by local hidden variable theories [99]. The former maintains that unless the detection efficiency is high enough (greater than 70%), the possibility remains that the experiment is biased by the subset of measurements that *do* violate the inequality while the greater set of all experiments measured and not measured *do not* violate Bell’s inequality. This has actually been closed by trapped ion experiments [89]. The second loophole, known as the “locality” or “lightcone loophole,” hypothesizes that subluminal signals can propagate amongst the different parts of the apparatus unless the choice of basis for measurement is outside of the reverse lightcone of the measurements on the opposite particle of the Bell pair. This has been closed with entangled photon pairs [103]. The state detection efficiency in trapped ions can easily be near unity, so the first

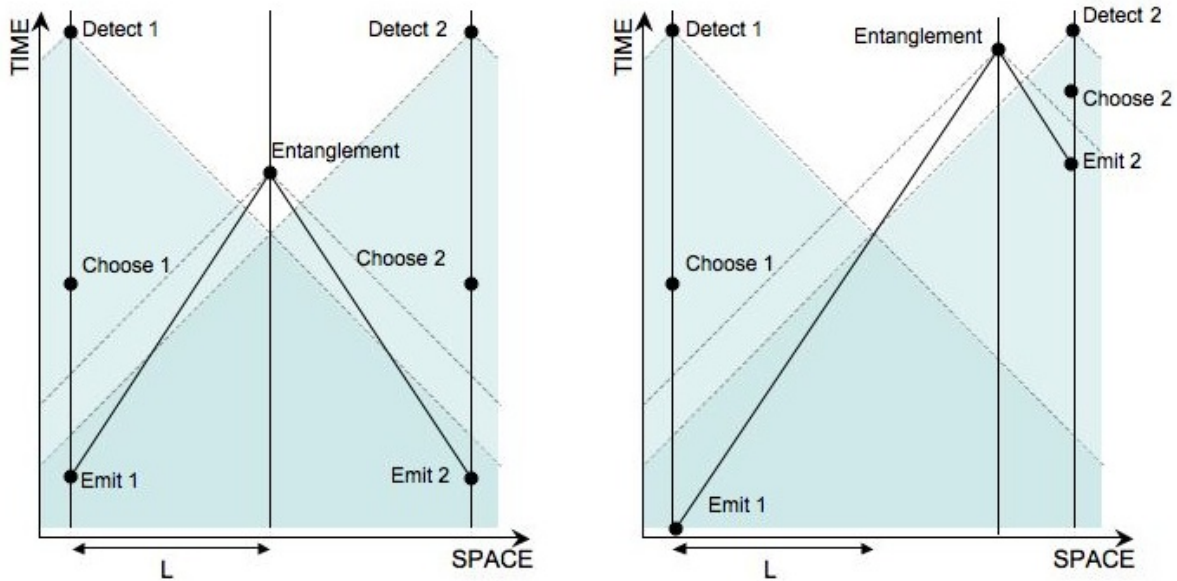


Figure 6.2: Adapted from [99], these show the space-time diagram of the progression of a Bell’s Inequality test that would simultaneously close the detection and locality loopholes. Left, the partial Bell-state analyzer is midway between the two ion traps, while to the right is a more likely experimental situation. “Emit” 1 and 2 refer to the ion excitation and decay, where the emitted photon propagates along the world-line at less than c . The entanglement of the ions is created where indicated, and “Choose” 1 and 2 refer to the choice of basis at each location.

loophole is easily closed. The latter can be closed if the experiment is set up as depicted in the space-time diagram shown in Fig. 6.2, with the ions located in separate traps separated by a distance of say one mile. The light travel time between the two locations would be $5.3 \mu\text{s}$. The velocity of the photons carrying the quantum information from each ion to the partial Bell state analyzer for the entanglement procedure would be slightly less than c because of the optical fiber, so the choice of basis for each measurement could fall outside of the reverse light cone of the opposite ion's measurement. Although the excitations (a few hundred femtoseconds) and decays (perhaps 50 ns) are not the bottle-necks, the individual qubit rotations and detection steps would have to take no more than a few microseconds, a difficult but in principle attainable feat.

While there is considerable effort in the trapped ion community to make ion traps smaller and smaller, incorporating increasing numbers of atoms in microfabricated trap structures capable of shuttling ions along tracks and even turning corners [102, 51], an alternative approach to a large-scale quantum computer is to employ what has been known as a cluster state [32]. In this model, a large-scale entangled array of ions is entangled via multiple photon-mediated entangling operations as described and the resulting cluster state can be used to perform quantum computations via appropriately chosen single-qubit projective measurements. It has been shown to be computationally equivalent to any conventional quantum circuit model computation so long as the entangled state incorporates two dimensions [87]. This is achieved with several 1D chains generated as already described, connected by a Hadamard/controlled phase flip operation on two ions in the middle of the entangled chains. The overhead in terms of the time required to generate the entangled state scales polynomially with the number of ions required. It is also possible to imagine using this probabilistic entanglement scheme to create local pairs of entangled ions which can then be used to implement deterministic gates between different sectors of a large-scale ion trap array. Quantum repeater schemes where entanglement is passed between intermediate nodes

separated by short distance can be used to turn the distance scaling from exponentially to linearly decaying [14, 31]

Bibliography

- [1] Leslie Allen and J. H. Eberly. *Optical Resonance and Two-Level Atoms*. Dover Publications N. Y., Inc., 1987.
- [2] Markus Ansmann et al. Violation of Bell's inequality in Josephson phase qubits. *Nature*, 461:504–6, 2009.
- [3] O. H. Arroe. Hyperfine structure and isotope shift in barium. *Phys. Rev.*, 79:836, 1950.
- [4] A. Aspect, P. Grainger, and G. Roger. Experimental realization of the Eintein-Podolsky-Rosen *gedankenexperiment*: A new violation of Bell's inequalities. *Phys. Rev. Lett.*, 49:91–4, 1982.
- [5] E. Back. Zur Kenntnis des Zeemaneffekts. *Annalen der Physik*, 375(5):333–372, 1923.
- [6] W. S. Bakr, J. I. Gillen, A. Peng, S. Fölling, and M. Greiner. A quantum gas microscope for detecting single atoms in a Hubbard-regime optical lattice. *Nature*, 462:74–77, 2009.
- [7] H. G. Barros, A. Stute, T. E. Northup, C. Russo, P. O. Schmidt, and R. Blatt. Deterministic single-photon source from a single ion. *New Jour. of Phys.*, 11:103004, 2009.
- [8] J. S. Bell. On the problem of hidden variables in quantum mechanics. *Reviews of Modern Physics*, 38:447, 1966.
- [9] K. Beloy, A. Derevianko, V. A. Dzuba, G. T. Howell, B. B. Blinov, and E. N. Fortson. Nuclear magnetic octupole moment and hyperfine structure of the $5D_{3/2,5/2}$ states of the Ba^+ ion. *Phys. Rev. A*, 77:052503, 2008.
- [10] D. Berkeland, J. D. Miller, J. Bergquist, W. M. Itano, and D. J. Wineland. Minimization of micromotion in a linear Paul trap. *Jour. of App. Phys.*, 83:5025–33, 1998.
- [11] D. J. Berkeland and M. Boshier. Destabilization of dark states and optical spectroscopy in Zeeman-degenerate atomic systems. *Phys. Rev. A*, 65:33413, 2002.

- [12] Eric Black. Notes on the Pound-Drever-Hall technique. Technical Report LIGO-T980045-00-D, Laser Interferometry Gravitational Wave Observatory, California Institute of Technology, 1998.
- [13] R. Blatt and D. J. Wineland. Entangled states of trapped atomic ions. *Nature*, 453:1008–1014, 2008.
- [14] H. J. Briegel, W. Duer, J. I. Cirac, and P. Zoller. Quantum repeaters: The role of imperfect local operations in quantum communication. *Phys. Rev. Lett.*, 81:5932–5, 1998.
- [15] C. Cabrillo, J. I. Cirac, P. García-Fernandez, and P. Zoller. Creation of entangled state of distant atoms by interference. *Phys. Rev. A*, 59:1025–33, 1999.
- [16] W. C. Campbell et al. Ultrafast gates for single atomic qubits. *Phys. Rev. Lett.*, 105:090502, 2010.
- [17] J. I. Cirac and P. Zoller. Quantum computations with cold trapped ions. *Phys. Rev. Lett.*, 74:4091–4, 1995.
- [18] J. F. Clauser and M. A. Horne. Experimental consequences of objective local theories. *Physical Review D*, 10:526–35, 1974.
- [19] J. F. Clauser, M. A. Horne, A. Shimony, and R. A. Holt. Proposed experiment to test local hidden-variable theories. *Physical Review Letters*, 23:880–4, 1969.
- [20] Coherent Laser Group, Santa Clara, CA. *The Coherent Mira model 900-B laser*, 1993.
- [21] T. B. Coplen et al. Commission on atomic weights and isotopic abundances report for the International Union of Pure and Applied Chemistry. In *Isotopic Compositions of the Elements*, volume 70, page 217. IUPAC, 1998.
- [22] J. J. Curry. Barium g factors. *Jour. Phys. Chem. Ref. Data*, 33:725, 2004.
- [23] Yehonatan Dallal. Toward high fidelity single ion qubit gates. Master’s thesis, Weizmann Institute of Science, Rehovot, Israel, 2009.
- [24] H. Dehmelt and P. A. Ekstrom. Proposed $10^{14}\Delta\nu < \nu$ laser fluorescence spectroscopy on Tl^+ mono-ion oscillator. *Bull. Am. Phys. Soc.*, 18:1521, 1973.
- [25] M. R. Dietrich and B. B. Blinov. Use of a microcontroller for fast feedback control of a fiber laser. [*arXiv:0905.2484*], 2009.
- [26] M. R. Dietrich, N. Kurz, T. Noel, Gang Shu, and B. B. Blinov. Hyperfine and optical barium qubits. *Phys. Rev. A*, 81:052328, 2010.
- [27] Matthew R. Dietrich. *Barium ions for quantum computation*. PhD thesis, University of Washington, 2009.

- [28] David DiVincenzo. Quantum computation. *Science*, 270(5234):255–61, 1995.
- [29] L.-M. Duan. Scaling ion trap quantum computation through fast quantum gates. *Phys. Rev. Lett.*, 93:100502–1, 2004.
- [30] L.-M. Duan and J. Kimble. Efficient engineering of multi-atom entanglement through single-photon detections. *Phys. Rev. Lett.*, 90:253601, 2003.
- [31] L.-M. Duan, M. D. Lukin, J. I. Cirac, and P. Zoller. Long distance quantum communication with atomic ensembles and linear optics. *Nature*, 414:413–8, 2001.
- [32] L.-M. Duan and R. Raussendorf. Efficient quantum computation with probabilistic quantum gates. *Phys. Rev. Lett.*, 95:080503, 2005.
- [33] V. A. Dzuba and V. V. Flambaum. Atomic optical clocks and a search for the variation of the fine structure constant. *Phys. Rev. A*, 61:034502, 2000.
- [34] V. A. Dzuba, V. V. Flambaum, and J. S. M. Ginges. Calculations of parity nonconserving s-d transitions in Cs, Fr, Ba⁺ and Ra⁺. *Phys. Rev. A*, 63:062101, 2001.
- [35] V. A. Dzuba and J. S. M. Ginges. Calculations of energy levels and lifetimes of low-lying states of barium and radium. *Phys. Rev. A*, 73:032503, 2006.
- [36] A. R. Edmunds. *Angular Momentum in Quantum Mechanics*. Princeton University Press, 1960.
- [37] A. Einstein, B. Podolsky, and N. Rosen. Can a quantum-mechanical description of reality be considered complete? *Physical Review*, 47:777, 1935.
- [38] Richard P. Feynman. Simulating physics with computers. *Int. Jour. of Theor. Phys.*, 21:467–88, 1982.
- [39] Christopher J. Foot. *Atomic Physics*. Oxford University Press, 2005.
- [40] T. M. Fortier et al. Precision atomic spectroscopy for improved limits on variation of the fine structure constant and local position invariance. *Phys. Rev. Lett.*, 98:070801, 2007.
- [41] E. N. Fortson. Possibility of measuring parity non-conservation with a single trapped atomic ion. *Phys. Rev. A*, 70:2383–2386, 1993.
- [42] S. J. Freedman and J. F. Clauser. Experimental test of local hidden variable theories. *Phys. Rev. Lett.*, 28:938–41, 1972.
- [43] A. Gallagher. Oscillator strengths of CaII, SrII and BaII. *Phys. Rev.*, 157:24, 1967.

- [44] J. J. García-Ripoll, P. Zoller, and J. I. Cirac. Speed optimized two-qubit gate with laser coherent control techniques for ion trap quantum computation. *Phys. Rev. Lett.*, 91:157901, 2003.
- [45] V. Gerginov. *Observation of a nuclear magnetic octupole moment of Cesium-133 through high resolution laser spectroscopy*. PhD thesis, Notre Dame, 2003.
- [46] D. A. Glazov, V. M. Shabaev, I. I. Tupitsyn, A. V. Volotka, V. A. Yerokhin, G. Plunien, and G. Soff. Relativistic and QED corrections to the g factor of Li-like ions. *Phys. Rev. A*, 70:062104, 2004.
- [47] Apollo Go. Observation of Bell inequality violation in B mesons. *Jour. of Mod. Optics*, 51:991–8, 2004.
- [48] G. Gopakumar, H. Merlitz, R.K. Chaudhuri, B. P. Das, U. S. Mahapatra, and D. Mukherjee. Electric dipole and quadrupole transition amplitudes for Ba^+ using the relativistic coupled-cluster method. *Phys. Rev. A*, 66:032505–1–6, 2002.
- [49] C. Guet and W. R. Johnson. Relativistic many-body calculations of transition rates for Ca^+ , Sr^+ , and Ba^+ . *Phys. Rev. A*, 44:1531–5, 1991.
- [50] D. Hayes et al. Entanglement of atomic qubits using and optical frequency comb. *Phys. Rev. Lett.*, 104:140501, 2010.
- [51] W. K. Hensinger, S. Olmschenk, D. Stick, D. Hucul, M. Yeo, M. Acton, L. Deslauriers, C. Monroe, and J. Rabchuk. T-junction ion trap array for two-dimensional ion shuttling, storage and manipulation. *Appl. Phys. Lett.*, 88:034101, 2006.
- [52] C. K. Hong, Z. Y. Ou, and L. Mandel. Measurement of subpicosecond time intervals between two photons by interference. *Phys. Rev. Lett.*, 59:2044–6, 1987.
- [53] G. Janik, W. Nagourney, and H. Dehmelt. Doppler-free optical spectroscopy on the Ba^+ mono-ion oscillator. *Jour. of the Opt. Soc. of Am. B*, 2:1251–7, 1985.
- [54] A. Kastberg, P. Villemoes, A. Arnesen, F. Heijkenskjöld, A. Langereis, P. Jungner, and S. Linnæus. Measurement of absolute transition probabilities in BaII through optical nutation. *Jour. Opt. Soc. Am. B*, 10:1330, 1993.
- [55] O. Yu Khetselius. Relativistic calculation of the hyperfine structure parameters for heavy elements and laser detection of the heavy isotopes. *Phys. Scr.*, T135:014023–6, 2009.
- [56] K. H. Knöll, G. Marx, K. Hübner, F. Schweikert, S. Stahl, C. Weber, and G. Werth. Experimental g_J factor in the metastable $5D_{3/2}$ state of Ba^+ . *Phys. Rev. A*, 54:1199–1205, 1996.

- [57] H. Kogelnik and T. Li. Laser beams and resonators. *Proceedings of the IEEE*, 54:1312–29, 1966.
- [58] T. Körber. *Measurement of light shift ratios with a single trapped $^{138}\text{Ba}^+$ ion, and prospects for a parity violation experiment*. PhD thesis, University of Washington, 2003.
- [59] N. Kurz, M. R. Dietrich, G. Shu, T. Noel, and B. B. Blinov. Measurement of Landé g -factor of $5\text{D}_{5/2}$ state of BaII with a single trapped ion. *Phys. Rev. A*, 82:030501(R), 2010.
- [60] N. Kurz, M. R. Dietrich, Gang Shu, R. Bowler, J. Salacka, V. Mirgon, and B. B. Blinov. Measurement of the branching ratio in the $6\text{P}_{3/2}$ decay of BaII with a single trapped ion. *Phys. Rev. A*, 77:060501(R), 2008.
- [61] T. Legero, T. Wilk, A. Kuhn, and G. Rempe. Time-resolved two-photon quantum interference. *Appl. Phys. B*, 77:797, 2003.
- [62] D. Leibfried, R. Blatt, C. Monroe, and D. J. Wineland. Quantum dynamics of a single trapped ion. *Rev. of Mod. Phys.*, 75:281–324, 2003.
- [63] D. Leibfried, B. DeMarco, V. Meyer, D. Lucas, M. Barrett, J. Britton, W. M. Itano, B. Jelenkovicacute, C. Langer, T. Rosenband, and D. J. Wineland. Experimental demonstration of a robust, high-delity geometric two ion-qubit phase gate. *Nature*, 422:412–6, 2001.
- [64] M. Lindberg and Stig Stenholm. The master equation for laser cooling of trapped particles. *Jour. of Phys. B*, 17:3375–89, 1984.
- [65] W. W. Macalpine and R. O. Schildknecht. Coaxial resonators with helical inner conductor. *Proceedings of the IRE*, 47:2009–2105, 1959.
- [66] A. A. Madej and J. D. Bernard. Single-ion optical frequency standards and measurement of their absolute frequency. In *Frequency Measurement and Control*. Springer Berlin, Heidelberg, 2001.
- [67] A. A. Madej and J. D. Sankey. Quantum jumps and the single trapped barium ion: Determination of collisional quenching rates for the $5\text{d}^2\text{D}_{5/2}$ level. *Phys. Rev. A*, 41:2621–30, 1990.
- [68] M. J. Madsen, D. L. Moehring, P. Maunz, R. N. Kohn, L.-M. Duan, and C. Monroe. Ultrafast coherent excitation of a trapped ion qubit for fast gates and photon frequency qubits. *Phys. Rev. Lett.*, 97:040505, 2006.
- [69] R. Maiwald, D. Leibfried, J. Britton, J. C. Bergquist, G. Leuchs, and D. J. Wineland. Stylus ion trap for enhanced access and sensing. *Nature Physics*, 5:551, 2009.

- [70] Harold J. Metcalf and Peter van der Straten. *Laser Cooling and Trapping*. Springer-Verlag, Inc., New York, 1999.
- [71] D. L. Moehring, M. J. Madsen, K. C. Younge, R. N. Kohn Jr., P. Maunz, L.-M. Duan, C. Monroe, and B. B. Blinov. Quantum networking with photons and trapped atoms. *Jour. Opt. Soc. Am. B*, 24:300–15, 2007.
- [72] D. L. Moehring, P. Maunz, S. Olmschenk, K. C. Younge, D. N. Matsukevich, L.-M. Duan, and C. Monroe. Entanglement of single atom quantum bits at a distance. *Nature*, 449:68, 2007.
- [73] B. E. Moore. Über die Zerlegung der Spektrallinien von Barium, Yttrium, Zirkon und Osmium in magnetischen Felde. *Annalen der Physik*, 330(2):309–345, 1908.
- [74] C. E. Moore. Atomic energy levels v. 3. In *Nat. Bur. Std. Circ. No. 467*. US Gov't. Printing Office, Washington, D. C., 1958.
- [75] P. F. Moulton. Spectroscopic and laser characteristics of $\text{Ti:Al}_2\text{O}_3$. *Jour. Opt. Soc. of Am. B*, 3:125, 1986.
- [76] W. Nagourney, J. Sandberg, and H. Dehmelt. Shelved optical electron amplifier: Observation of quantum jumps. *Phys. Rev. Lett.*, 56:2797–2799, 1986.
- [77] W. Neuhauser, M. Hohenstatt, P. E. Toschek, and H. Dehmelt. Localized visible Ba^+ mono-ion oscillator. *Phys. Rev. A*, 22, 1980.
- [78] T. Noel. Adiabatic passage. *In preparation*, 2010.
- [79] S. Olmschenk, D. Hayes, D. N. Matsukevich, P. Maunz, D. L. Moehring, and C. Monroe. Quantum logic between distant trapped ions. *Int. Jour. Quant. Inf.*, 8:337, 2010.
- [80] S. Olmschenk, D. N. Matsukevich, P. Maunz, D. Hayes, L.-M. Duan, and C. Monroe. Quantum teleportation between distant matter qubits. *Science*, 323:486, 2009.
- [81] Z. Y. Ou and L. Mandel. Violation of bell's inequalities and classical probability in a two-photon correlation experiment. *Phys. Rev. Lett.*, 81:50–3, 1988.
- [82] Wolfgang Paul. Electromagnetic traps for charged and neutral particles. *Rev. of Mod. Phys.*, 62:531–40, 1990.
- [83] F. M. Penning. The energy balance for an infinitely small electron current in a uniform electric field. *Physica*, 5:286–97, 1938.
- [84] E. H. Pinnington, R. W. Berends, and M. Lumsden. Studies of laser-induced fluorescence in fast beams of Sr^+ and Ba^+ ions. *Jour. Phys. B*, 28:2095, 1995.

- [85] O. Poulsen and P. S. Ramanujam. Time-differential level-crossing g -value measurements of the $6p^2P$ fine-structure levels in $^{138}\text{BaII}$ using an optical-induced orientation or alignment of a fast ionic beam. *Phys. Rev. A*, pages 1463–67, 1976.
- [86] J. D. Prestage, R. L. Tjoelker, and L. Maleki. Atomic clocks and variations of the fine structure constant. *Phys. Rev. Lett.*, 74:3511–3514, 1995.
- [87] R. Raussendorf and H. J. Briegel. A one-way quantum computer. *Phys. Rev. Lett.*, 86:5188–91, 2001.
- [88] J. Reader et al. Wavelengths and transition probabilities for atoms and atomic ions. In *Natl. Bur. Stand. Ref. Data Ser., Circ. No. 68*, volume 10. Gov't Printing Office, Washington, D. C., 1980.
- [89] M. A. Rowe, D. Kielpinski, V. Meyer, C. A. Sackett, W. M. Itano, C. Monroe, and D. J. Wineland. Experimental violation of a Bell's inequality with efficient detection. *Nature*, 409:791, 2001.
- [90] B. Sahoo, R. Chaudhuri, B. Das, and D. Mukherjee. Relativistic coupled-cluster theory of atomic parity nonconservation: Application to $^{137}\text{Ba}^+$. *Phys. Rev. Lett.*, 96:163003, 2006.
- [91] B. K. Sahoo et al. Magnetic dipole hyperfine interactions in $^{137}\text{Ba}^+$ and the accuracies of the neutral weak interaction matrix elements. *Phys. Rev. A*, 68:040501(R), 2003.
- [92] J. J. Sakurai. *Modern Quantum Mechanics*. Addison Wesley, New York, 1994.
- [93] J. Sherman, W. Trimble, S. Metz, W. Nagourney, and E. N. Fortson. Progress on indium and barium single-ion optical frequency standards. In *2005 Digest of the LEOS Summer Topical meetings*, IEEE Cat. No. 05TH8797, New York, 2005. IEEE.
- [94] Jeff A. Sherman. *Single barium ion spectroscopy: light shifts, hyperfine structure, and progress toward an optical frequency standard and atomic parity violation*. PhD thesis, University of Washington, 2006.
- [95] Bruce W. Shore. *The Theory of Coherent Atomic Excitation*, volume 2, Multilevel atoms and incoherence. John Wiley and Sons, Inc., 1990.
- [96] Bruce W. Shore. *The Theory of Coherent Atomic Excitation*, volume 1, Simple atoms and fields. John Wiley and Sons, Inc., 1990.
- [97] G. Shu, N. Kurz, M. R. Dietrich, and B. B. Blinov. Efficient fluorescence collection from trapped ions with an integrated spherical mirror. *Phys. Rev. A*, 81:042321, 2010.
- [98] Gang Shu. *Novel ion traps for enhanced fluorescence collection & single photon sources based on barium ions*. PhD thesis, University of Washington, 2010.

- [99] Christopher Simon and William T. Irvine. Robust long-distance entanglement and a loophole-free bell test with ions and photons. *Phys. Rev. Lett.*, 91:110405, 2003.
- [100] A. V. Steele, L R. Churchill, P. F. Griffin, and M. S. Chapman. Photoionization and photoelectric loading of barium ion traps. *Phys. Rev. A*, 75:053404, 2007.
- [101] Stig Stenholm. The semiclassical theory of laser cooling. *Rev. of Mod. Phys.*, 58:699–739, 1986.
- [102] D. Stick, W. Hensinger, S. Olmschenk, M. Madsen, K. Schwab, and C. Monroe. Ion trap in a semiconductor chip. *Nature Phys.*, 2:36–9, 2006.
- [103] G. Weihs, T. Jennewain, C. Simon, H. Weinfurter, and A. Zeilinger. Violation of Bell’s inequality under strict Einstein locality conditions. *Phys. Rev. Lett.*, 75:5039–43, 1998.
- [104] K. Wendt, S. A. Ahmad, F. Buchinger, A. C. Mueller, R. Neugart, and E. W. Otten. Relativistic J-dependence of the isotope shift in the 6s-6p doublet of BaII. *Zeitschrift für Physik*, 318:125–9, 1984.
- [105] T. Wilk, S. C. Webster, A. Kuhn, and G. Rempe. Single-atom, single-photon quantum interface. *Science*, 317:488, 2007.
- [106] N. Yu, W. Nagourney, and H. Dehmelt. Radiative lifetime measurement of the Ba⁺ metastable D_{3/2} state. *Phys. Rev. Lett.*, 78:4898–4901, 1997.

VITA

Nathan Kurz was born to Albert and Sandra Kurz on 20 July 1982 in Manassas, VA, where he lived until attending college at the Pennsylvania State University starting in Aug. 2000. He received his Bachelor of Science in Physics in 2004 after which he accepted a Fulbright Fellowship for study at the Technische Universität München where he worked with the E11 Lehrstuhl on time-resolved spectroscopy of melting ice under pressure. Lasers looked like fun at that point, and he joined the newly forged trapped ion quantum computation group under Dr. Boris Blinov at the University of Washington in Sept. 2005. After graduation he will continue on there under Drs. Blayne Heckel and Norval Fortson and measure zero to perhaps one more decimal place on the permanent electron electric dipole moment on ^{199}Hg .